The Thesis Committee for Prachi Mehta
Certifies that this is the approved version of the following thesis:

Application of Superparamagnetic Nanoparticle-based Heating for Non-Abrasive Removal of Wax Deposits from Subsea Oil Pipelines

APPROVED BY
SUPERVISING COMMITTEE:

Supervisor: _____
Hugh Daigle

Co-Supervisor: _____
Chun Huh

Application of Superparamagnetic Nanoparticle-based Heating for Non-Abrasive Removal of Wax Deposits from Subsea Oil Pipelines

by

Prachi Mehta, B.E.

Thesis

Presented to the Faculty of the Graduate School of

The University of Texas at Austin

in Partial Fulfillment

of the Requirements

for the Degree of

Master of Science in Engineering

The University of Texas at Austin

August 2015

Dedication

I would like to dedicate this thesis to my parents – Sumer Singh Mehta and Suman Mehta, who have always supported me without any question or hesitation. Their support and unbound love is the reason I keep going on. I owe them, my ‘American Dream’.

Acknowledgements

This thesis would not be possible if not for certain wonderful people – professors, friends and acquaintances; whom I had the fortune to meet and know over the past two years.

First, I would like to thank my professors – Dr. Bryant, for being an eccentric, brilliant professor who sparked my imagination, helped me grow and believe in myself, and above all, gave me the freedom of choosing my way; Dr. Huh, for being a constant source of enthusiasm, positivity and support. He has always thought the best for and of me, much more than I could have; and Dr. Daigle, for being very supportive, patient and accommodating. Special thanks to Dr. Bostick, from the electrical department for his generous help in explaining the theory of magnetic field propagation and circular coil in a steel pipeline.

Next, I would like to thank my friends – Glen Baum, for being the life support of all my experimental work. If I was allowed to include a co-author, he rightfully deserved the title. He has been a motivating friend, well-wisher and again, the lifeline for my experiments; Eva Vinegar, for being my first friend in America and one of the most wonderful; and Kishen Rafiz, for always being there and motivating me. They have been a constant emotional support.

Finally, I would like to thank some acquaintances – Dwight Romanovicz, for helping me take images of the tiniest nanoparticles; Dr. Mohsen Ahmadian, for letting me use the VSM equipment at the BEG; and Dr.Qing Wang, for providing me with lab-synthesized nanoparticles.

A heart-felt thank you to one and all!

Abstract

Application of Superparamagnetic Nanoparticle-based Heating for Non-Abrasive Removal of Wax Deposits from Subsea Oil Pipelines

Prachi Mehta, M.S.E.

The University of Texas at Austin, 2015

Supervisor: Hugh Daigle

Co-Supervisor: Chun Huh

Flow assurance is a critical problem in the oil and gas industry, as an increasing number of wells are drilled in deep water and ultra-deep water environments. High pressures and temperatures as low as 5°C in these environments hinder flow of hydrocarbon-based fluids by formation of methane hydrate and wax deposits on the inner surface of pipelines. Commonly used methods for removal of deposits from pipelines are chemical injection and foam or gel pigs, which face several limitations. In our work, an application to use superparamagnetic nanoparticle-based heating for flow assurance, in the form of a magnetic nanopaint is presented. Superparamagnetic nanoparticle-based heating has been extensively researched in the biomedical industry for cancer treatment by hyperthermia. Superparamagnetic nanoparticles in dispersions generate heat by application of an oscillating magnetic field as explained by Neel's relaxation theory. In

our application, superparamagnetic Fe_3O_4 nanoparticles are embedded in a thin layer of cured epoxy termed 'nanopaint'. This nanopaint coating on the internal surface of subsea pipelines could generate heat and thus remove formation of methane hydrates and wax.

In our work, the role of key parameters affecting heating performance of superparamagnetic nanoparticles such as particle size, and magnetic field is quantified. Rigorous characterization of physical and magnetic properties of nanoparticles and nanopaint is performed. This is correlated to and used to optimize the heating performance. Heating performance of several samples of Fe_3O_4 nanoparticles varying in size distribution is evaluated in static experiments. Two samples having similar physical and magnetic properties are compared in terms of the correlation between their size distribution and their heating performance. Performance of nanopaint to heat static fluids, flowing fluids and wax deposit is evaluated. Heating performance of superparamagnetic nanoparticles in dispersions and in nanopaint is found to be similar and so it is concluded that Neel's relaxation theory is applicable to nanopaint. Heating performance of nanopaint in flow experiment is found to be better than in static experiments by a factor greater than 5. A correlation of heating performance of nanopaint at magnetic fields of 100 to 1000 A/m is developed. Finally, implementation issues of nanopaint are addressed. The effect of low ambient temperatures on nanopaint heating performance is evaluated. The theoretical feasibility of generating a magnetic field inside a pipeline is studied. A COMSOL model is used to verify the feasibility of magnetic field propagation inside a steel pipeline and is subsequently used to evaluate nanopaint heating of wax deposits in pipeline. Material and power requirements are analyzed and optimized using the COMSOL model.

Table of Contents

List of Tables

List of Figures

Chapter 1: Introduction

As an increasing number of wells are drilled in deep offshore fields and oil and gas are produced in cold subsea environment, flow assurance becomes a critical problem for their unhindered transport. This thesis proposes a novel method of applying magnetic nanoparticles for heat generation in the form of a nanoparticle-embedded coating on the inner surface of a pipeline and the subsequent removal of wax deposits from oil pipelines.

The work presented in this thesis is divided into six chapters. In the first, introductory chapter, a brief overview of the motivation of this work is presented, i.e., flow assurance in subsea pipelines. Then, the objectives of this research work are discussed. In the second chapter, the background for the magnetic nanoparticle regimes and heating modes are presented; the heating performance parameter, 'Specific Absorption Rate (SAR)' is described; and the parameters affecting SAR are discussed. The third chapter presents the materials used for the experiments, characterization methods for determination of physical and magnetic properties of magnetic nanoparticles and nanopaint; and subsequently, prediction of SAR of nanoparticles based on size distribution analysis. The fourth chapter describes the experimental setup, methodology and results of static, flow and wax heating experiments; quantifies of the effect of thermal properties and low ambient temperatures on performance of nanopaint; and describes the limitations of translating SAR results to different systems. The fifth chapter describes the proposed method of removing wax that was deposited in a nanopaint-coated subsea pipeline; and the theoretical feasibility of the generating magnetic field inside steel pipelines. Then COMSOL, a simulation software that computes magnetic field and temperature distributions, is used to model, simulate and optimize wax removal in subsea steel pipelines by nanopaint and estimate the power requirements for this application. The

final chapter outlines the general conclusions from this thesis and future work necessary to commercialize the idea of magnetic nanopaint for flow assurance.

1.1 MOTIVATION: FLOW ASSURANCE IN SUBSEA PIPELINES

Flow assurance is the ability to transport hydrocarbon-based fluids economically and safely from the reservoir to surface processing facilities, over the life of the field. During the exploration and production of crude oil and gas from deep water and ultra-deep water wells, subsea production facilities are employed. Due to the difficulty of construction and high costs, these facilities need be designed with higher degree of precision, accounting for all possible risks during the life of the well. A key objective is the safe and economic transportation of oil and gas from the production facilities to processing/ distribution sites, i.e., flow assurance. At these conditions, the pipeline fluids are subjected to cold subsea temperatures of ~ 5 °C. The high temperature gradient decreases pipeline temperature along the length of the pipeline. When the temperature falls below the cloud point, heavier hydrocarbons like wax or asphaltenes start precipitating out and get deposited on the inner walls of the pipeline. Over time, these deposits increase in thickness and hinder flow of fluids, posing safety concerns.

Various methods are employed for remediation and prevention of flow assurance problems, primarily relying on the principles of temperature increase, pressure reduction or mechanical hindrance (Denniel et al. 2004). The most common correction method is the use of pigs for mechanical removal of deposits. These are highly compressible foams that are inserted periodically into the pipeline for abrasive, mechanical removal of (Minami et al. 1999). However, pig operation has several limitations. It requires shutdown of operation leading to lost revenue due to disruption in production. Further, pigs tend to get stuck in pipeline suspending production for extended periods of time.

We propose to use superparamagnetic nanoparticle-based heating (Benz 2012) for non-abrasive removal of deposits from pipelines. It is the practice of using superparamagnetic nanoparticles (SPM-NP) and an external magnetic field for a highly localized and focused delivery of heat. As will be described in detail later, when these particles are subjected to the magnetic field oscillation of certain frequency range, intense heat can be generated by the internal spinning of magnetic poles in the single-domain superparamagnetic nanoparticles. Its primary application to date is to destroy cancerous tissue in human beings (Pankhurst et al. 2003). In that application, nanoparticles with a special surface coating are injected into human blood stream, which attach themselves at the target cells. Magnetic field oscillation is then applied externally to the body to heat up the particles and subsequently the target cells locally. Applications involving SPM-NPs have several merits : a) control over surface area of heating; b) localized heating; c) control of heating rates by varying concentration of nanoparticles and magnetic field; d) moderate requirement of infrastructure or chemicals; and hence, use of these for prevention and remediation of problems associated with cooling-induced deposition of solids is an attractive and promising application.

In our proposed application, we coat the inner surfaces of pipelines with "nanopaint" which is a paint with superparamagnetic nanoparticles dispersed in it. This nanopaint (Davidson et al. 2012) generates heat upon application of an alternating magnetic field. By generating an intense, localized heating by the nanopaint, the wax/asphaltene deposits on the painted surface can melt and peel itself away from the pipe wall and flow in the bulk pipeline fluid. Magnetic energy may be delivered by means of a hydraulically balanced, buoyant, portable device that moves along the length of the pipeline. Such a device can be inserted into the pipe periodically so as to remove formation of a thin layer of deposit from the pipeline. Thus, we propose a new method for

chemical-free, non-abrasive removal of pipeline deposits using superparamagnetic-nanoparticle based paint.

1.2 RESEARCH OBJECTIVES

Earlier work in this field has been the biomedical applications of heating of superparamagnetic nanoparticles in liquid (Hergt et al. 2004; Rovers et al. 2009) and embedded in a solid by freeze-drying (Hsu & Su 2008). To the best of our knowledge, this is the first time that these particles have been used for heat generation while being embedded in a solid medium. The novel application of nanoparticle-based paint for flow assurance is first described in Davidson et al. (2012). However, the characterization of nanopaint; and limits and parameters that affect nanopaint-based heating has not been discussed. Heating by SPM-NPs is mainly dependent on particle size distribution, and magnetic field strength and frequency, among other parameters (Lévy et al. 2008). It is important to understand these limits and parameters to optimize heating performance of superparamagnetic nanoparticles.

The focus of the current work is to perform rigorous characterization of the nanopaint; and the identification and quantification of the governing parameters to optimize nanopaint-based heating in static experiments. Further, issues regarding its implementation in a real scenario, namely wax removal from a subsea steel pipeline system, will be addressed. For effective implementation of experimental results to field, the performance of nanopaint at low temperatures and the feasibility of nanopaint to melt wax deposits will be evaluated. A model of nanopaint heating of wax by magnetic field will be modeled using computational modeling software, COMSOL. Optimization of nanopaint application in terms of power requirement and cost will be briefly discussed.

[1]Chapter 2: Theoretical Background

2.1 HYPERTHERMIA OVERVIEW

Hyperthermia is the process of destroying cancerous tissues by elevated temperatures of the order of 42 °C – 46 °C (Ondeck et al. 2009). Traditionally, hyperthermia resulted in damage to surrounding healthy tissue due to non-selective and uncontrolled radiation. However, technology advances have made possible targeted and local hyperthermia, also called magnetic fluid hyperthermia (Jordan et al. 1999). This is effected by injecting selectively-attachable magnetic nanoparticles into the body and subjecting them to an alternating magnetic field, which produces localized heat treatment. Medical studies have also indicated that nanoparticles are more efficient at heating than micron-sized particles. The heating produced is dependent on the size of the nanoparticles, and magnetic field strength and frequency among other factors.

The concept of magnetic fluid hyperthermia was first proposed by Gilchrist et al. in 1957, to destroy cancer in lymph nodes of dogs. Technological innovation in the past two decades has resulted in refinement of this technology, specifically in superparamagnetic iron oxide (Fe_3O_4) nanoparticles. Extensive literature exists on iron oxide for nanoparticle-based heating, due to its compatibility with biological tissues (Wang et al. 2010; Pankhurst et al. 2003). Studies on heating losses of superparamagnetic nanoparticle were done by Neel in 1957. Rosensweig (2002) developed a model for quantification of heating losses and its dependence on various parameters. Thus, this technology has been developed and applied for novel use in biomedicine. We seek to apply this exciting technology to deliver localized heat for oil and gas applications, particularly for flow assurance in subsea pipelines.

[1] Mehta, P., Huh, C., & Bryant, S. L.,2014. Evaluation of superparamagnetic nanoparticle-based heating for flow assurance in subsea flowlines. International Petroleum Technology Conference. IPTC-18090-MS
All work was performed by Prachi Mehta and supervised by Steven Bryant and Chun Huh.

2.2 Relevant Magnetic Principles

In order to understand the principle of magnetic fluid hyperthermia, we need to know a few basic principles on the generation of an alternating magnetic field. This is achieved experimentally by passing current through a multi-turn coil or a solenoid. The flow of an alternating (AC) current generates an alternating magnetic field at the center of the coil, which is strongest at the center and decreases in strength with distance away from the coil. The electromagnetic (EM) wave produced by a coil is a transverse electric wave, which means that there is no electric field in the direction of wave propagation, and the magnetic field propagates in the direction of the EM wave. Magnetic field of a long coil (solenoid) is given by Ampere's law:

$$H = \frac{NI}{L}, \tag{1}$$

where H is the magnetic field (A/m), N is the number of turns of the coil (solenoid), I is the current flowing through the solenoid (A), and L is the length of the solenoid (m). This equation holds true only for a long solenoid whose radius is very small compared to its length, which is not true for our system but a proper accounting will be made later. Hence, the magnetic field formula used in our calculation was derived from Biot-Savart law, shown in Appendix C. Here, magnetic field is calculated for each turn and the calculated cumulative value reflects the actual magnetic field. The magnetic field of each turn for the three-turn coil is calculated by

$$H_z = \frac{Ia^2}{2(a^2+z^2)^{3/2}}, \tag{2}$$

The magnetic field formula of the three-turn coil (see equation (2)) was modified to account for the spiral ribbon shape of the five-turn coil and is calculated by

$$H_z = \frac{I}{2h}\left[\frac{z+\frac{h}{2}}{\sqrt{a^2+\left(z+\frac{h}{2}\right)^2}} - \frac{z-\frac{h}{2}}{\sqrt{a^2+\left(z-\frac{h}{2}\right)^2}}\right], \quad (3)$$

where H_z is magnetic field at the center axis of the coil (A/m), I is the current (A), a is the radius of the coil (m), h is the height of each ribbon (m), and z is the height of the coil or distance from origin (m).

Next, we look at the material of interest – magnetic nanoparticles. The revolving electrons in the nanoparticles' atoms generate an electric field and hence have an associated magnetic field. Hence all particles have magnetic moments due to the force exerted by these magnetic fields. In a nanoparticle, there are distinct regions called magnetic domains. All magnetic moments in a domain have the same direction; however the direction changes across a domain. The magnetic moment direction varies depending on the variations in structure, physical or magnetic properties of nanoparticles called anisotropy. (Benz 2012)

Due to the variation in magnetic moment, there are different types of magnets, namely paramagnets, diamagnets and ferromagnets. In paramagnets, magnetic moments align in the direction of the applied field but magnetism is lost once the field is removed. In diamagnets, magnetic moments align opposite to the magnetic field, then disappear once it is removed. Ferromagnets contain multiple domains in which the spins of free electrons within the material align, thus creating a permanent magnetic moment within each domain. The spin alignment direction of each domain within the material is random, so they tend to cancel each other and the net magnetic moment of ferromagnets is

typically small. However, in the presence of a magnetic field, the magnetic moment of all of the domains align, which generates a larger magnetization than for other types of magnetic materials, as well as increases the magnetic field amplitude.

The type of magnetic material most important for this work has a form of paramagnetism known as superparamagnetism (Benz 2012). Superparamagnetism is found in ferromagnetic materials in the size range 3 – 50 nm in diameter. They have much higher magnetic susceptibilities than typical paramagnets. Superparamagnets have zero coercivity and remanence (Kneller & Luborsky 1963). Coercivity is the magnetization required to reduce a magnetized material back to non-magnetized condition after reaching saturation. Hence, zero coercivity means that the internal magnetic moment of the material will randomize with no reverse magnetization necessary when the magnetic field is removed. Zero remanence means that removal of the external magnetic field will randomize the internal magnetic moment of the superparamagnet which reduces the magnetization of the material to zero. Because of these two principles, the magnetization of superparamagnetic materials does not display hysteresis. The phenomena of superparamagnetism in nanoparticles is described in detail below.

2.3 Magnetic Nanoparticle Regimes and Heating Modes

Magnetic nanoparticles have properties very different from colloidal magnetic particles, owing to their high surface to volume ratio and the quantum phenomena occurring at the nanoscale. Our range of interest lies between a few nm to ~150 nm, specifically with respect to iron oxide. Magnetic nanoparticles in this range show enhanced heating due to different loss mechanisms. The loss mechanisms vary with particle size and structure. Magnetic domain variation with particle size results in

different nanoparticle regimes (Thanh 2012). The characteristics and heat loss mechanism associated with the different regimes is schematically shown in Figure 1 and will be explained in detail below.

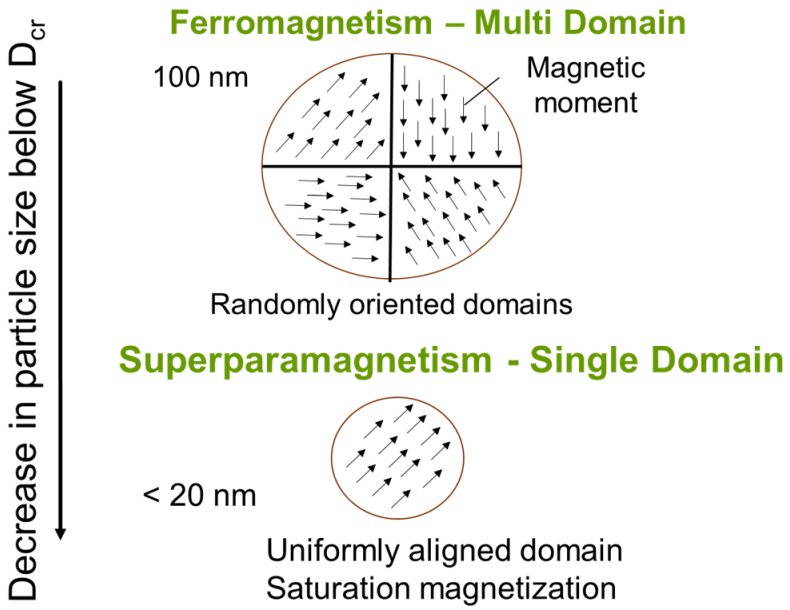

Figure 1: Transition from multi-domain to single-domain nanoparticle

2.3.1 Multi-Domain Regime

Multi-domain nanoparticles are made of several distinct domains whose magnetic moment vary across domains. The result is that magnetic moments tend to cancel each other and the net magnetic moment can be negligible (as in a paramagnet) or have a net positive value (as in a ferromagnet). The particles have certain stable orientation due to surface, crystal and volume anisotropy (Goya et al. 2003). Thus, the moments tend to align in these stable orientations that represent minimum energy levels. Hence, a minimum energy barrier needs to be crossed to move these moments from the minimum

energy level. This energy is supplied by an external magnetic field which tends to rotate the moment in the direction of the applied field. When a sufficiently large field is applied, all the moments align in the direction of the applied field, i.e., achieve saturation magnetization.

In the case of multi-domains, magnetization leads to moment rotation across domain walls, i.e., an applied external field leads to displacement of domain walls. The magnetization lags behind the magnetic field, i.e., the magnetization does not reduce to zero in the absence of an applied field (Kita et al. 2008). This results in heat loss by hysteresis. The greater the coercivity, greater the magnetic energy is converted to heat. Multi-domain nanoparticles have smaller coercivity values compared to single domain particles due to interactions between the domains (Kneller & Luborsky 1963).

2.3.2 Single Domain Regime

As particle size decreases, the particle reaches a critical diameter where it can support only a single-domain magnetic structure. Now, the particle has only one magnetic moment, with all the moments in the domain aligned in the same direction. The coercivity increases with particle diameter and reaches a maximum before transition into multi- domain region. Hence, this regime represents the maximum heat loss achievable by hysteresis. The behavior of particles in this regime is described by Stoner-Wohlfarth model. The particle relaxation time is much larger than measurement time (frequency) and hence it exhibits hysteresis. This means that the magnetization lags behind the applied magnetic field, leading to a displacement of the magnetization curve during de-magnetization. The area enclosed by the magnetization curves during the magnetization and de-magnetization cycle is called the hysteresis area. This heat loss by hysteresis gradually decreases with decreasing coercivity and becomes zero in the SPM regime. The

transition region between single and multi-domain is called pseudo-single domain. Hysteresis can decrease by increasing concentration due to dipole interactions. Heating by hysteresis can be predicted by

Specific Loss Power (SLP) = hysteresis area x frequency of magnetic field (4)

Heat loss in this regime can be predicted by knowing the coercivity and magnetization of nanoparticle. Coercivity values limit the area of the hysteresis loop which is directly proportional to heating. Coercivity dependence on particle size is given by Kneller & Luborsky (1963). However, there is no clear theory on prediction of coercivity based on physical parameters of nanoparticles, and hence heat loss is difficult to predict.

2.3.3. Superparamagnetic Regime

Superparamagnetic nanoparticles are single-domain nanoparticles whose coercivity is zero. This means that the magnetization follows changes in the applied magnetic field. The particles exhibit uniaxial anisotropy and hence have stable preferred orientation, which corresponds to the state of minimum energy (Thanh 2012). This energy is supplied by the alternating magnetic field which excites the particle and results in heat generation (Coffey & Kalmykov 2012). There are two primary mechanisms of heating: Neel relaxation and Brown relaxation (Kötitz et al. 1999). The frequency of magnetic field and particle size determines which mechanism dominates.

Brown relaxation is the physical rotation of particles which causes heat loss due to viscous forces. In this case, the magnetic moment is locked to the crystal axis and so the whole particle rotates in the medium. This generally occurs in particles smaller than 13 nm and at frequencies less than 300 kHz. The heat loss may be attributed to the fact that the frequencies are so small that the magnetic moment almost entirely stays at the

ground state, due to thermal fluctuations and so the particle itself rotates. The limiting factor for Brown relaxation is viscous media that hinder particle movement.

Neel relaxation is the reorientation or rotation of the particle moment resulting in heat loss (Bakoglidis et al. 2012; Kneller & Luborsky 1963). When an alternating magnetic field of a certain frequency is applied, the magnetic moment of a superparamagnetic nanoparticle rotates several times within a time interval, generating heat. This happens when the Neel relaxation time is much smaller than the characteristic measurement time. The Neel relaxation time describes the time taken by the particles to reach thermal equilibrium before relaxing. The time required to magnetize a nanoparticle to saturation is the characteristic measurement time, τ_m. If $\tau_m >> \tau_N$, then the magnetic moment will rotate several times (excite and relax) within the Neel relaxation time and the particle magnetization during the measurement period will average to zero. Contrarily, if $\tau_N >> \tau_m$ then the particle does not have time to excite and relax, thus its magnetic moment appears blocked. Neel relaxation usually occurs in particles of diameter between 5-30 nm and at frequencies between 100 kHz and 1 GHz (Bakoglidis et al. 2012). Neel relaxation produces more heat for a given magnetic field compared to other processes. Hence, we are interested in exploiting this phenomenon for our application.

2.4. QUANTIFICATION OF HEATING: SPECIFIC ABSORPTION RATE (SAR)

The heating performance by Neel relaxation is described in terms of specific absorption rate (SAR), that relates the heat energy produced with the conditions of magnetic field and particle properties (Rovers et al. 2009; Rosensweig 2002). Theoretically, SAR (W/g) is given by

$$SAR = \frac{2(\pi m H f \tau_N)^2}{\tau_N K_B T V \rho (1+(2\pi f)^2 \tau_N{}^2)}, \quad (5)$$

$$\tau_N = \tau_o e^{\frac{KV}{K_B T}}, \quad (6)$$

where SAR = specific absorption rate (W/g), m = $\mu_o M_d V$ is the magnetic moment (Jm/A), M_d is the domain magnetization of nanoparticle (A/m), μ_o is the permeability of free space (N/A^2), H is the magnetic field amplitude (A/m), f is the frequency (Hz), T is the temperature (K), V is particle volume (m^3), ρ is density of nanoparticle (g/m^3), K_B is Boltzmann constant (J/K), K is volumetric magnetic anisotropy of nanoparticle (J/m^3), τ_o is a constant and τ_N is the Neel relaxation time (s). SAR shows quadratic dependence on magnetic field strength and is inversely proportional to temperature. Superparamagnetic nanoparticles undergoing Neel relaxation are known to follow the above dependence.

Empirically, SAR for batch experiments can be calculated from the measurement of temperature increase for a SPM-NP sample subjected to a prescribed magnetic field oscillation by

$$SAR = \frac{C_{P,system}\Delta T}{\left(\frac{W_{NP}}{W_{sample}}\Delta t\right)}, \quad (7)$$

where $C_{P,system}$ is the specific heat capacity ($Jg^{-1}K^{-1}$) of the system (either nanoparticle dispersion or nanopaint-water system), ΔT is the temperature rise in the system during an increment of time Δt, W_{NP} is the weight of nanoparticles in the sample either in dispersion or in nanopaint, W_{sample} is the total weight of the sample (nanoparticle dispersion or nanopaint-water system). According to equation (5), SAR is independent of nanoparticle concentration (W_{NP}/W_{sample}), thermal properties of the medium or system

containing nanoparticles, and time of measurement. Hence, SAR should essentially be the same for the same nanoparticles at different concentrations, except when magnetic interaction between individual nanoparticles occurs. In the literature, SAR values as high as 400 W/g have been reported (Hergt et al. 2004). The physical limit of hyperthermia by superparamagnetic nanoparticle in terms of structural and magnetic properties is described by Neel's relaxation theory (Hergt et al. 1998). Heating performance of magnetic nanoparticles can be controlled by variation of particle size, applied field frequency and amplitude (Hergt et al. 2008; Glöckl et al. 2006). It is important to understand these limits and governing parameters to optimize heating performance of superparamagnetic nanoparticles.

The application of nanopaint exploits the fact that superparamagnetic nanoparticles can generate heat by Neel relaxation even while fixed in a solid medium through Neel relaxation. The paint is simply a method of fixing a thin layer of nanoparticles to a surface. Here we use the approach of Davidson et al. (2012) in which magnetite nanoparticles are embedded in epoxy to create nanopaint. The nanopaint is then applied to the surface of the object to be heated, and after drying the nanopaint is capable of generating and dissipating heat to its surroundings. The focus of the current paper is the identification and quantification of the governing parameters for the optimization of nanopaint-based heating in batch and flow experiments. This necessitates the description of SAR in a flow system, and is calculated by

$$SAR_{flow} = \frac{\dot{m} c_{p,system} \Delta T}{w_{NP}}, \quad (8)$$

where ṁ is the mass flow rate (g/s) of the fluid flowing through the pipe, $C_{P,system}$ is the specific heat capacity ($Jg^{-1}K^{-1}$) of the flowing fluid plus the nanopaint on the pipe wall, ΔT is the temperature rise of the fluid between outlet and inlet, and W_{NP} is total mass of nanoparticles in the nanopaint.

2.5 THEORETICAL CONSIDERATION OF PARAMETERS THAT AFFECT HEATING PERFORMANCE

The importance of nanoparticle size, magnetic field and temperature on heating efficiency optimization is demonstrated employing the theoretical SAR equation (5) and (6). The values of the parameters (Rovers et al. 2009) used for this evaluation are shown in Table 1.

Symbol	Value
M_d (kA/m)	447
τ_o (s)	10^{-9}
K_B (J/m^3)	1.38 E-23
K (J/m^3)	8000
T (K)	298

Table 1: Values of parameters used for prediction of SAR

2.5.1 Particle size

Heating performance can be primarily controlled by varying particle size, as reported by studies on size dependence on heating (Chatterjee et al. 2003; Gonzales-Weimuller et al. 2009). It has been found that restricting particle diameter to a small range can significantly improve heating (Hergt et al. 2008; Bakoglidis et al. 2012). This

dependence is given by the SAR correlation (equation (5)) developed by Rosensweig (2002). In order to better understand the dependence below, we show the effect of particle diameter on SAR for two frequencies of interest.

The effect of particle diameter (D_P) on SAR at 600 A/m is evaluated using equation (5). Prediction of SAR as a function of nanoparticle diameter at two frequencies of interest, 450 kHz and 630 kHz, is shown in Figure 2. SAR is shown to increase sharply as particle diameter is varied across an optimum narrow size range: we see that there is a five-fold increase in SAR when particle diameter is varied from 15 nm to 17 nm. This shows that heating is a strong function of particle diameter, given the same magnetic field. Nanoparticle samples are often poly-dispersed in size. Subsequently, a sample that has higher concentration of particles in the optimum size range will have higher SAR and hence better heating.

Next, we look at the effect of frequency. For 450 kHz, the optimum size range based on full width at half maximum (FWHM) is between 16 - 20 nm and for 630 kHz, it is between 16-19 nm. There is a small shift in the optimum size range as the frequency changes. An important point to note here is that optimum size range is not the same for all samples. It varies with the shape and magnetic properties of the particles among other factors. This needs to be understood while comparing different samples.

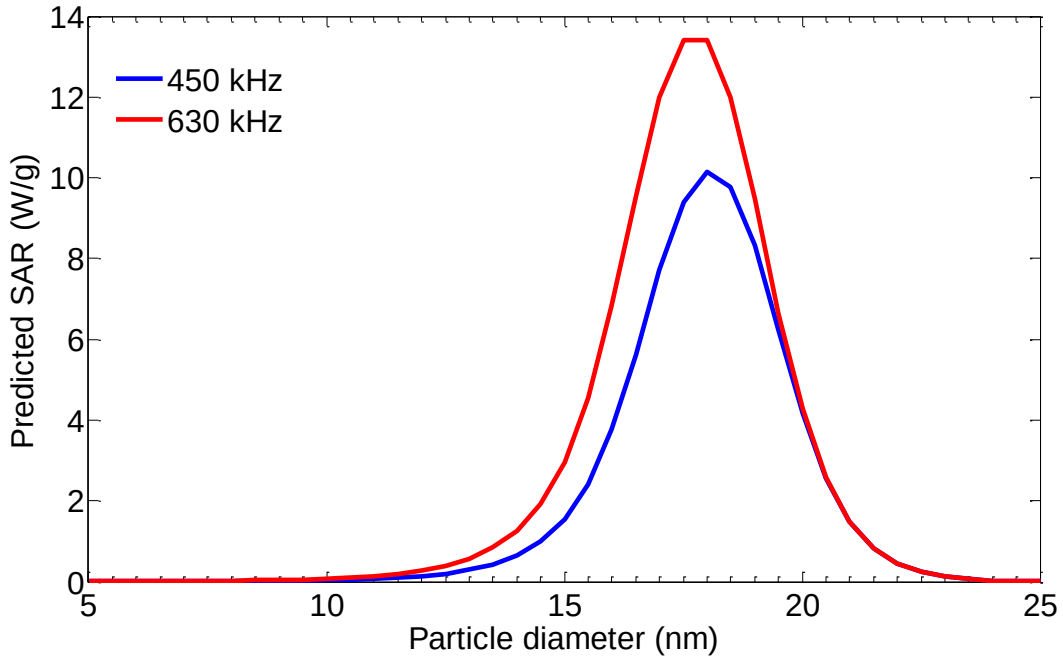

Figure 2: SAR dependence on nanoparticle diameter and frequency at magnetic field H=600 A/m and magnetic anisotropy K=8000 J/m^3

2.5.2 Magnetic field strength/amplitude

SAR (W/g) has shown to have a linear relation with the square of magnetic field (H^2) (Glöckl et al. 2006). The effect of the magnetic field (H) on SAR is evaluated using equation (5). Prediction of SAR at 450 kHz as a function of magnetic field strength is shown in Figure 3. It shows that SAR increases with magnetic field for a given particle diameter.

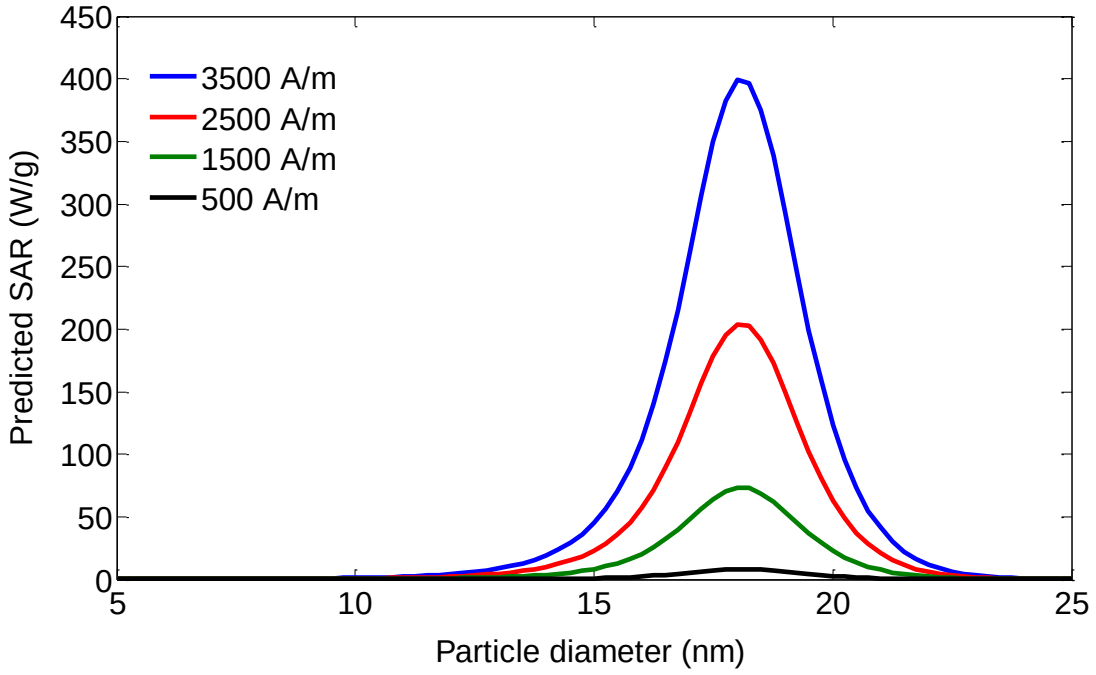

Figure 3: SAR dependence on nanoparticle diameter and magnetic field at frequency f=450 kHz, and magnetic anisotropy K=8000 J/m^3

2.5.3. Temperature

Prediction of SAR as a function of temperature is shown in Figure 4. It is seen that SAR decreases at higher temperatures (Hergt et al. 1998). However, at lower temperatures, SAR is higher, indicating better heating efficiency, which is good for the nanopaint-based heating for the cold subsea environment. Understanding of the temperature dependence on SAR is especially important as our proposed application would have variation of temperature across a wide temperature range from 5°C to 50°C. Hence the temperature effect needs to be analyzed experimentally. Since localized heat accumulation due to poor thermal conductivity can result in significant decrease in SAR with time, the effect

of thermal conductivities of the paint and the fluids flowing in it on nanopaint heating will also be analyzed.

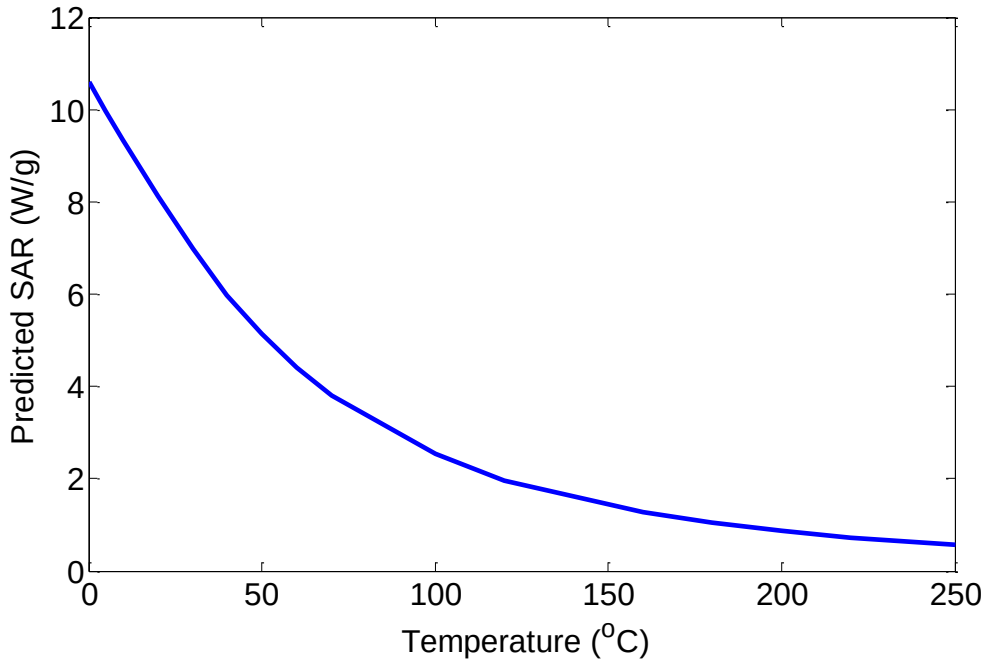

Figure 4: SAR dependence on ambient temperature from 100 °C to 250 °C at a magnetic field frequency of 450 kHz and magnetic field of 600 A/m

[2]Chapter 3: Characterization of Materials

3.1 MATERIALS

All investigations presented in this paper are based on iron oxide (Fe_3O_4) nanoparticles, mainly with EMG 1400 and EMG 605 procured from Ferrotec, Germany. Secondary investigations were also performed on in-house synthesized sample PAA-8K and Ocean Nanotech samples ONN 25 and ONN 30. EMG 1400 with hydrophobic surface treatment was provided as in powder form and EMG 605 with a hydrophilic surface treatment was provided as an aqueous dispersion at a concentration of 15.85 % by weight of Fe_3O_4. PAA-8K was coated with polyacrylic acid and dispersed in water at a concentration of 0.5 % by weight and ONN 25 and ONN 30 were dispersed in chloroform at a concentration of 10 wt.%. In our experiments, EMG 1400 was diluted by toluene/hexane and EMG 605 was diluted by DI water.

Nanopaint was prepared by dispersing sonicated samples of EMG 605 or EMG 1400 solution in the paint. The paint used was Macropoxy 646 A and B from Sherwin Williams in the ratio 1:1 by weight. The nanopaint was coated on the internal surfaces of polycarbonate cylinders (diameter = 2 cm, height = 7 cm), which were surrogate 'pipes', manually using a paint brush. The coating was left to cure and dry for 24 – 48 hours. The dried coating was light brown to dark brown in color depending on the concentration of iron oxide, as shown in Figure 5.

[2] Mehta, P., Huh, C., & Bryant, S. L.,2014. Evaluation of superparamagnetic nanoparticle-based heating for flow assurance in subsea flowlines. International Petroleum Technology Conference. IPTC-18090-MS
All work was performed by Prachi Mehta and supervised by Steven Bryant and Chun Huh.

Figure 5: Nanopaint coated on internal surface of polycarbonate sylinders shows variation in color due to varying concentrations of iron oxide in paint

The concentration of nanoparticles in nanopaint is calculated by measuring the weight of the sample before and after drying. The basis for this calculation is that the weight loss of paint is primarily due to evaporation of volatile components like toluene. The concentration is calculated as weight % of Fe_3O_4 using equation (9).

$$w_P = \frac{w_{BD} \times W}{w_{AD}} \tag{9}$$

where w_P is the weight fraction of Fe_3O_4 nanoparticles in dried nanopaint, w_{BD} is the weight of the wet paint on the substrate, W is the weight fraction of nanoparticles in wet paint and w_{AD} is the weight of the dried paint. The specific heat capacity of the paint is given by equation (10).

$$c_{p,Paint} = c_{p,Iron\ Oxide} \times w_P + c_{p,Epoxy} \times (1\text{-}w_P) \quad (10)$$

where $c_{p,Paint}$ is the specific heat capacity of the dried nanopaint (J/g.K), $c_{p,Iron\ Oxide}$ and $c_{p,Epoxy}$ is the specific heat capacity of iron oxide and epoxy respectively (J/g.K) and w_P is the weight fraction of nanoparticles in the dried nanopaint. The properties of materials used in these experiments are summarized in Table 2.

Fluid	ρ (kg/m^3)	C_p(J/g.K)	k (W/m.K)
Water	999	4.18	0.58
Toluene	866	1.13	0.14
Iron Oxide (Fe_3O4)	4800	0.67	N/A
Epoxy	1200	0.92	N/A

Table 2: Properties of materials used for heating experiments

3.2 CHARACTERIZATION OF NANOPARTICLES AND NANOPAINT

3.2.1 Size Determination

Particle size was determined using an FEI Tecnai transmission electron microscope (TEM). EMG 605 and PAA-8K were dispersed in water for the measurement, while EMG 1400 and ONN 25 were dispersed in toluene. 10 – 20 μL of the sample were pipetted onto coated grids based on their affinity. EMG 605 was put on formvar-coated molybdenum grids and EMG 1400 was put on carbon-coated molybdenum grids. Several images were taken at different magnifications and locations on the grid. The images are shown in Figure 6 with the scale of 50 nm shown.

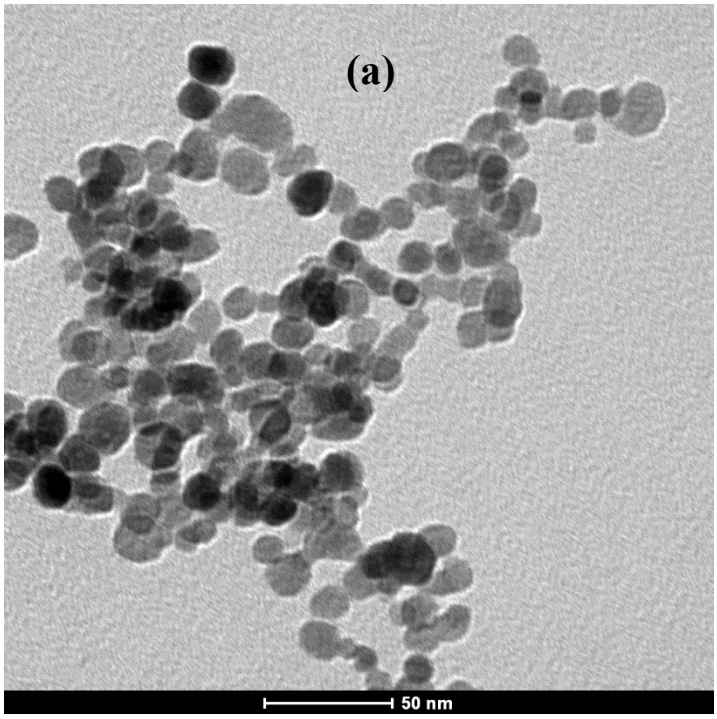
(a)
50 nm

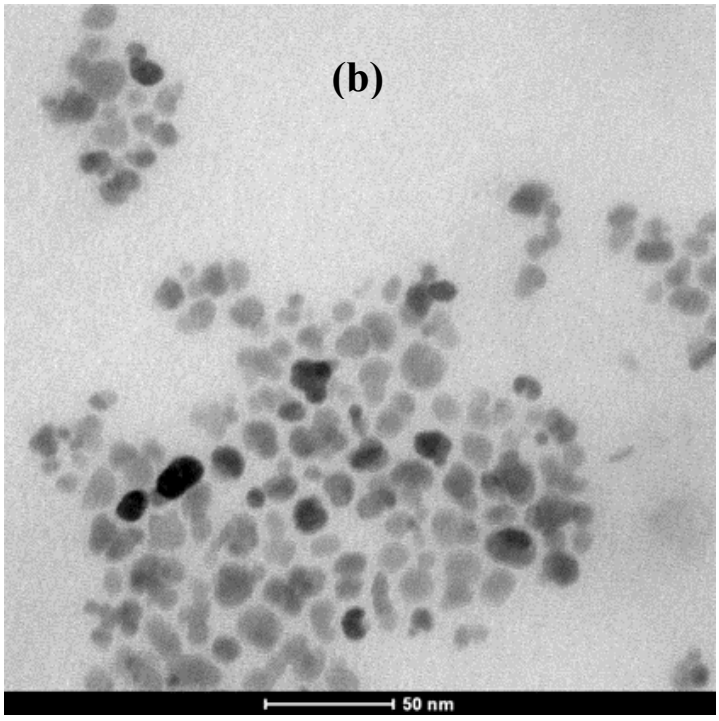
(b)
50 nm

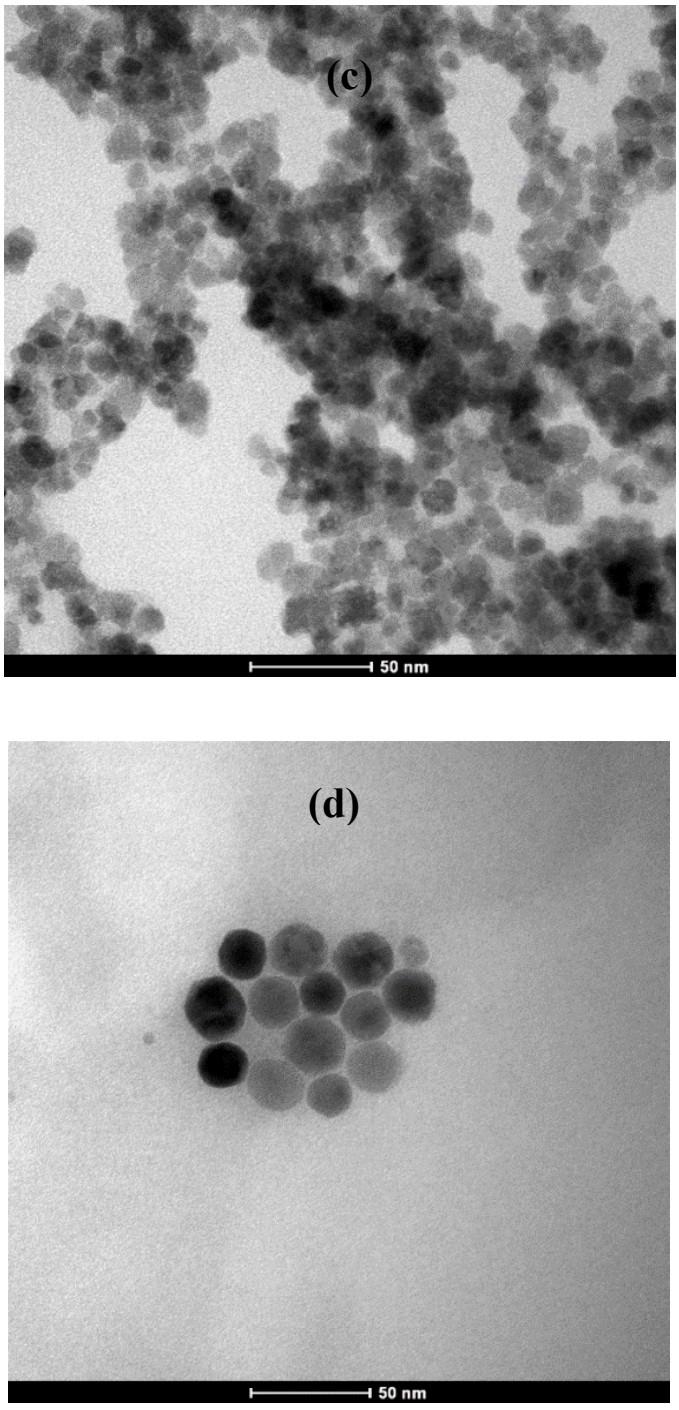

Figure 6: Transmission Electron Microscope (TEM) images of iron oxide (Fe_3O_4) nanoparticles samples: (a) EMG 605, (b) EMG 1400, (c) PAA-8K, and (d) ONN 25.

The images can be used to measure the size of individual particles. Samples which are synthesized by the same method nevertheless have comparable magnetic and physical properties and hence their heating performance can be compared, such as EMG 605 and EMG 1400. These samples were thus further analyzed to obtain particle size distributions. The summary of characterization of these samples is shown in Table 3.

Property	Symbol/Unit	EMG 1400	EMG 605
Surface coating	-	Hydrophobic	Hydrophilic
Mean particle diameter (TEM)	D_p (nm)	10.6 +/- 2.4	11.3+/-3.1
Volume %	%	70	3.9
Saturation magnetization of nanoparticle	M_s (10^3 A/m)	450.5	451.5

Table 3: Summary of characterization of nanoparticle samples EMG 1400 and EMG 605

The images were processed using open source software, ImageJ. A sample set of over 100 particles were measured for EMG 605 and EMG 1400, to give the size distribution and mean size based on number intensity as shown in Figure 7. The figure shows that the two samples are very similar in their mean size distribution. Since SAR can vary substantially over a small size range as described earlier, we calculate the composite SAR for the two samples as described below.

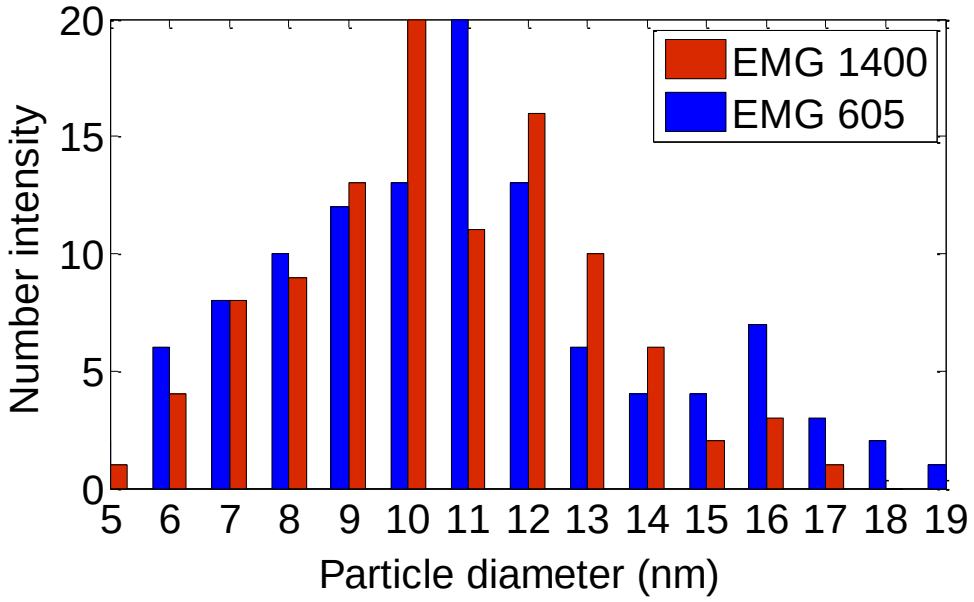

Figure 7: Particle size distribution of EMG 605 and EMG 1400 samples based on analysis of TEM images

Prediction of SAR Based on Particle Size Distribution

The particle size distribution obtained from TEM analysis was used to predict the heating performance of EMG 605 and EMG 1400 in terms of SAR. Equation (5) was used to calculate SAR of a particle of size 'D' nm subjected to a magnetic field of 'H' A/m and frequency of 'f' Hz. Using this equation, SAR for different particle sizes was calculated. Using the number intensity of particle size shown in Figure 7, the SAR contribution by each particle size was found and was averaged for the total number of particles to give the predicted effective SAR value of the sample. Thus, SAR values were predicted for EMG 605 and EMG 1400 samples. It was predicted that SAR of EMG 605 is better than EMG 1400 by a factor greater than 5 for a given field and frequency. This is

attributed to EMG 605 having more number of particles of higher SAR compared to EMG 1400. This hypothesis was tested using experiments, as discussed in Chapter 4.

3.2.2 Magnetic Properties: Vibrating Sample Magnetometer

Magnetization and magnetic susceptibility were determined in a vibrating sample magnetometer (VSM). A vibrating sample magnetometer is a device that physically vibrates the sample inside a uniform magnetic field. A pick up coil measures the induced voltage which is a measure of the sample's magnetic moment or magnetization. Magnetization is the density of induced magnetic moments in a magnetic material. Here, the magnetization of the sample was recorded as a function of the applied magnetic field from 0 to 796 kA/m. This is called a Langevin curve. A Langevin curve showing no hysteresis is a characteristic of SPM-NPs. The initial slope of the curve is used to calculate magnetic susceptibility.

We measured the magnetic properties of the nanoparticles in a fluid, in a solid medium i.e., the paint and in a colloidal suspension of sand in water. First, several samples of EMG 605 at concentrations of 0 – 3.9 % by volume in DI water and solid powder of EMG 1400 were analyzed. Next, the effect of sand on susceptibility of iron oxide nanoparticles EMG 605 was analyzed. The EMG 605 nanofluid was mixed with F95 silica sand at concentrations of 0 to 3.9 % by volume and analyzed. Analysis of nanopaint required prior preparation and drying of EMG 605 paint at concentrations of 0 – 3.9 % by volume. A representative sample of the dried paint was used for analysis.

The Langevin curves of all samples showed no hysteresis. This curve shows magnetization induced in the magnetic sample for an entire alternating cycle of 796 kA/m or 10,000 Oe. The results were normalized for the concentration and the normalized results for EMG 605 nanoparticles and nanopaint is shown in Figure 8. Magnetization is

lower for nanoparticles in paint when compared to those in fluid. We believe that non-uniform distribution of nanoparticles in nanopaint resulted in this deviation.

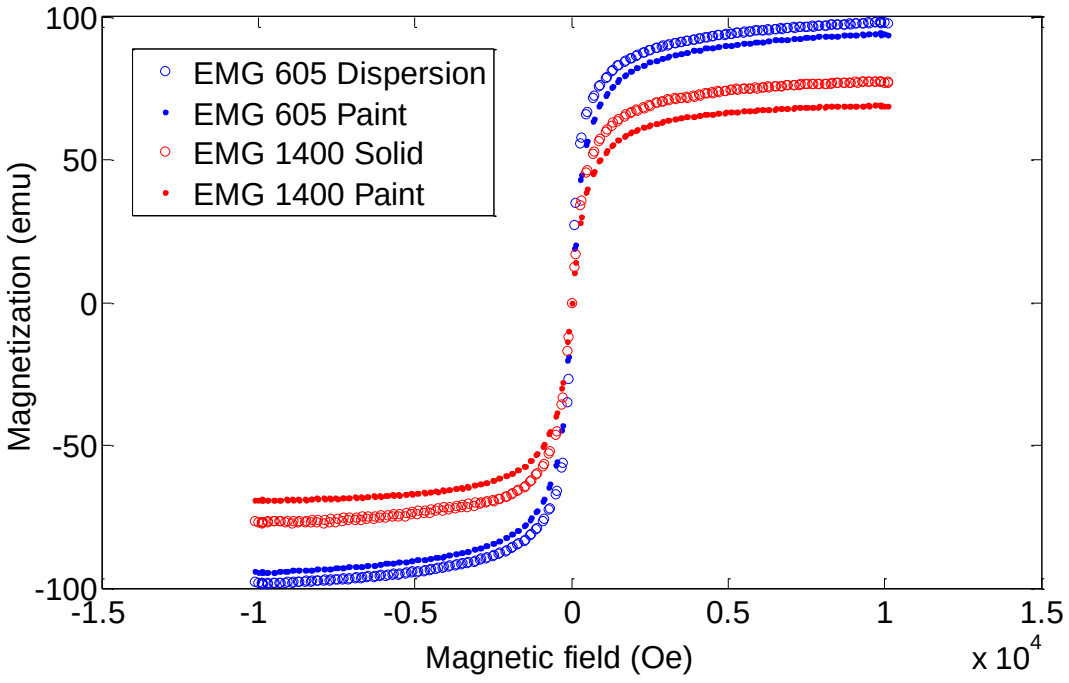

Figure 8: Langevin curves for EMG 605 dispersion and paint; and EMG 1400 solid and paint

The susceptibility values of EMG 605 nanofluid in water, in sand and in paint were recorded and are summarized in Figure 9. This shows the variation of susceptibility as a function of nanoparticle concentration in different media. It is seen that the susceptibility follows a linear relation with concentration. Also, EMG 605 shows a similar behavior in fluid as well as in a slurry of EMG 605 nanofluid in sand. The susceptibility drops much lower in paint, which is believed to be due to interference by the epoxy paint.

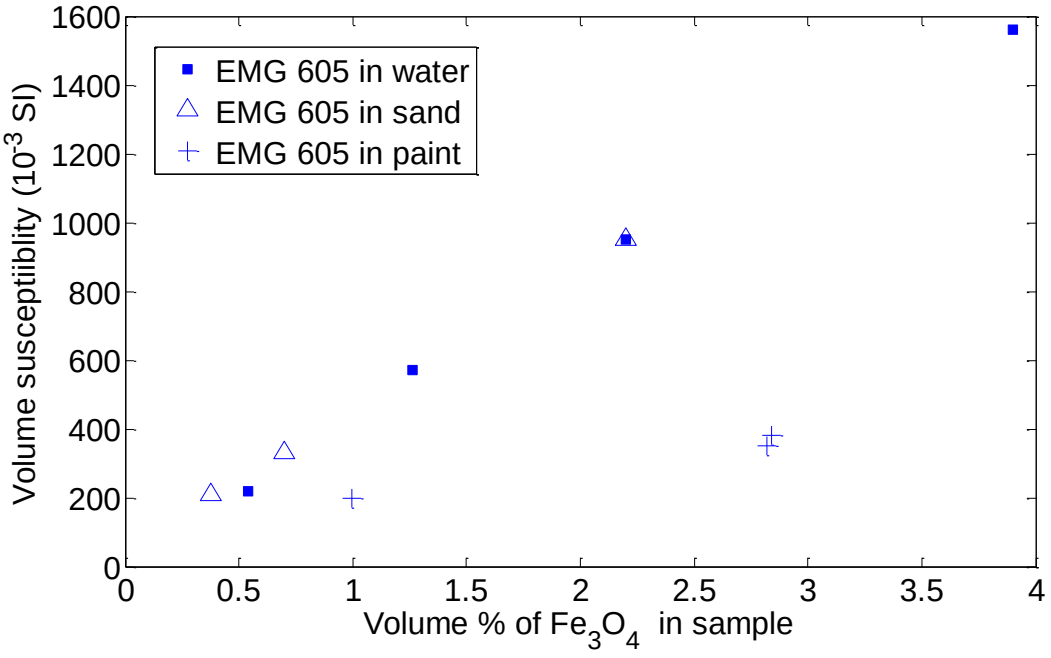

Figure 9: Susceptibility of EMG 605 nanofluid in water, sand and in paint at various concentrations from 0 to 3.9 % by volume.

3.2.3 Physical Properties of Nanopaint

The dried nanopaint was examined physically, for the distribution of nanoparticles in the medium and the variation in nanopaint thickness. Nanoparticles embedded in nanopaint were imaged using a scanning electron microscope (SEM), as shown in Figure 10. This shows the nanoparticles coated with paint, clustered together in distinct groups. Hence, it is believed that there are a few localized heat spots in the paint that release majority of the heat.

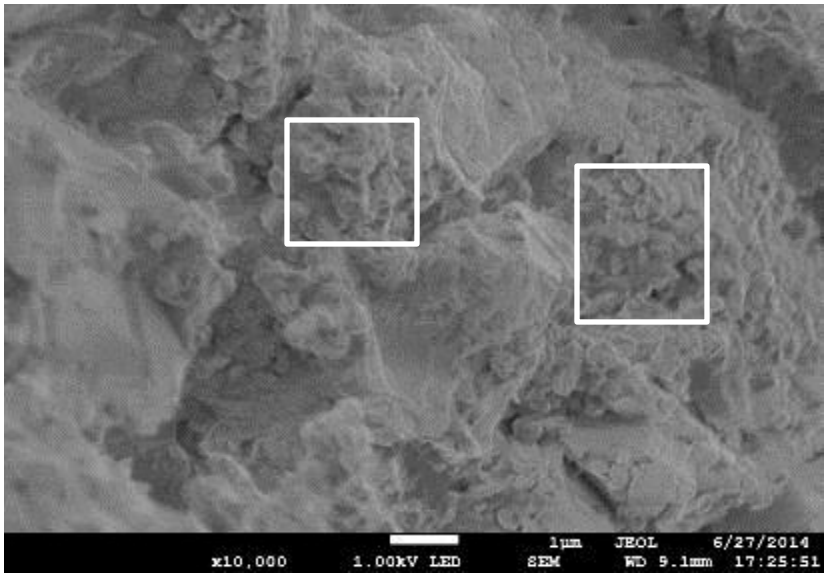

Figure 10: Scanning Electron Microscope (SEM) image of nanopaint showing iron oxide particle clusters in a matrix of paint (scale:1 micron)

A thin cross-section of nanopaint was analyzed under a Keyence digital optical microscope and is shown in Figure 11. It shows the thickness varying between 90 – 300 μm.

Figure 11: Digital microscope image of cross-section of nanopaint film shows thickness variation from 90 to 300 μm.

Limitation of existing formulation

The paint formulation is simple and easily reproducible. The primary limitations are non-uniform distribution of nanoparticles in the nanopaint and non-uniform thickness of paint. These result in concentration of nanoparticles in selective spots, resulting in varied heating across the film. This results in different temperatures across the surface of a nanopaint film subject to an alternating magnetic field. However, when the net contribution of a nanopaint film to a system such as water is considered, the heating due to the entire film is measured, thus eliminating the effect of varied localized heating by concentrated particles. So, these limitations are not deemed to be significant for our application, where the net contribution of all nanoparticles is measured on a macroscopic scale. However, a uniform coating is vital for applications where surface heating is required to be uniform. Hence, we looked at methods to produce uniform nanopaint films.

Nanopaint Fabrication Method: Spin Coater

A well-established technical method is employed to develop a more uniform coating of paint. A spin coater, shown in Figure 12, is a device that spins a liquid sample on a flat substrate at a certain speed, which enables vaporization of the volatile components leading to a solid coating. For our application, it was spun at 1500 rpm for 30 seconds to form a solid film. Different media and substrates were used for the trials to form a uniform, solid layer of robust coating. The thickness of the coating can be controlled by variation of speed of rotation and time; lower speeds result in thicker coatings. The robustness of such a film depends on the material of the coating and chemical compatibility between the coating and the substrate.

We did trials using different mediums - epoxies Macropoxy 646 A and B, EPON 815 C resin and Versamid 125; and polystyrene- polyisoprene-polystyrene co-polymer.

Flat sheets made of polyether, polyvinyl chloride, polycarbonate and polypropylene were also used. The sheets were cut into small rectangles of 2.5 cm x 7.5 cm and different media containing nanoparticle sample EMG 605 were placed on them. The sheets were rotated at a speed of 1000 – 1500 rpm for 30 s to 60 s.

Figure 12: Spin coater used to develop uniform nanopaint on substrate

The nanoparticles were found to be incompatible with the EPON resin and would lead to clusters. In the case of the co-polymer, a uniform coating was obtained but it could be easily destroyed by scratching. A robust coating was obtained using the macropoxy and EMG 605 combination. It was observed that the nanopaint coating made using this method is uniform and is about 10 – 14 μm in thickness. This coating would be useful where uniform surface heating is desired. However, it is not possible to coat the interior of a hollow cylinder using this device. Hence for our experiments, the manually applied coating is used for the sake of simplicity and effectiveness.

[3]Chapter 4: Heating Experiments: Static and Flow

4.1 Experiment Setup and Methodology

All experiments were conducted in a magnetic induction heater, which serves as the magnetic field oscillation generator. The device consists of a power unit, detachable multi-turn coils and coolers. The power unit of the heater supplied an alternating current to a coil, which generated an oscillating magnetic field around the coil. The schematic of the magnetic field generation setup is shown in Figure 13.

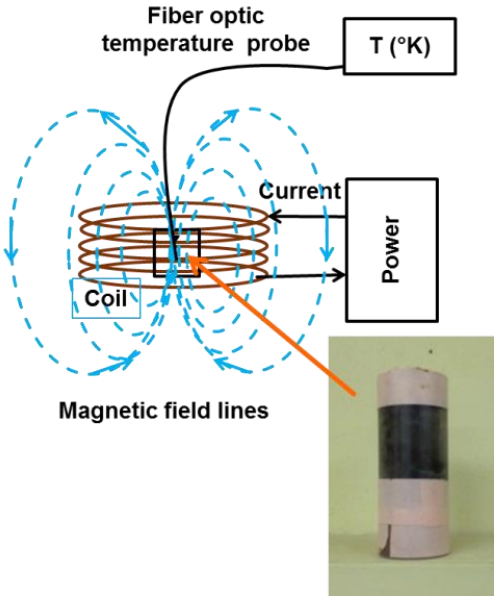

Figure 13: Schematic of experimental setup shows a nanopaint sample placed in a magnetic field generated by a current-carrying multi-turn coil; fiber-optic temperature probe is used for measuring heating of sample by nanoparticles dispersed in fluid or in nanopaint.

[3] Mehta, P., Huh, C., & Bryant, S. L.,2014. Evaluation of superparamagnetic nanoparticle-based heating for flow assurance in subsea flowlines. International Petroleum Technology Conference. IPTC-18090-MS
All work was performed by Prachi Mehta and supervised by Steven Bryant and Chun Huh.

The magnetic field is strongest at the center of the coil and decreases in intensity as we move towards the outer part. Hence, it is important to place samples at the same position, for comparison of results with the same intensity of magnetic field. The magnetic field induces Neel relaxation in the nanoparticles and generates heat in the sample, which is measured by a temperature probe.

The magnetic field generator used for our experiments was model SI-100-KWHF from Superior Induction, as shown in Figure 14. Different coils were attached to the heater to achieve different oscillation frequencies. A three-turn coil (radius = 5 cm, height = 3 cm) was used to produce a 450 kHz field, and five-turn spiral ribbon-shaped coil (radius=1.6 cm, height = 30 cm) was used to produce a 630 kHz field.

Figure 14: Magnetic induction heater equipment from Superior Induction

The magnetic field strength was varied by controlling current input to the coil from 5 to 25 A. Temperature measurement is done using a fiber-optic temperature probe, NOMAD from Neoptix, Canada.

4.2 STATIC EXPERIMENTS

Static experiments of nanofluid and nanopaint were performed at 450 kHz in the three-turn coil (vertical configuration) by varying magnetic field between 200 to 600 A/m. The magnetic field was calculated using equation (2).

4.2.1 Nanofluid

Identical hollow tubes (diameter = 2 cm, height = 7 cm; closed on one end) made of PVC or polycarbonate were used to hold the static nanofluid. The experiments were performed for concentrations ranging from 0.5 to 6 % by weight of Fe_3O_4 in dispersion. EMG 605 and PAA-8K were diluted with DI water; and EMG 1400, ONN 25 and ONN 30 were diluted with toluene. All samples were sonicated in a bath sonicator for 10 – 30 minutes to break down any agglomerates and maintain homogeneity.

4.2.2 Nanopaint

Two types of nanopaint were prepared by dispersing EMG 1400 and EMG 605 in epoxy respectively. The dispersions were mixed well to ensure uniform distribution of nanoparticles in paint. Identical hollow tubes (diameter = 2 cm, height = 7 cm; closed on one end) made of PVC were coated with nanopaint using a paint brush and left to cure for 24 - 48 hours at room temperature. These were termed EMG 1400 paint and EMG 605 paint, respectively. The experiments were performed for concentrations ranging from 0.5 to 15 wt. % of Fe_3O_4 in the paint. The concentration of nanoparticles in nanopaint was calculated using equation (9) and specific heat capacity of the paint was calculated using equation (10).

The tubes were insulated with urethane foam and placed at the center and middle of the coil, where magnetic field intensity is maximum. All experiments were performed with a constant mass of sample, completely contained inside the coil and at the same location, and for the same measurement time of 300 s. This ensures that comparison of results is made for similar experimental conditions. The magnetic field was turned on and the temperature was measured at the center of the tube and plotted as a function of time. The slope of the plot $\Delta T/\Delta t$ in the linear region was calculated as shown in Figure 15 and substituted in equation (7) along with specific heat capacity and weight fraction of nanoparticles to give SAR.

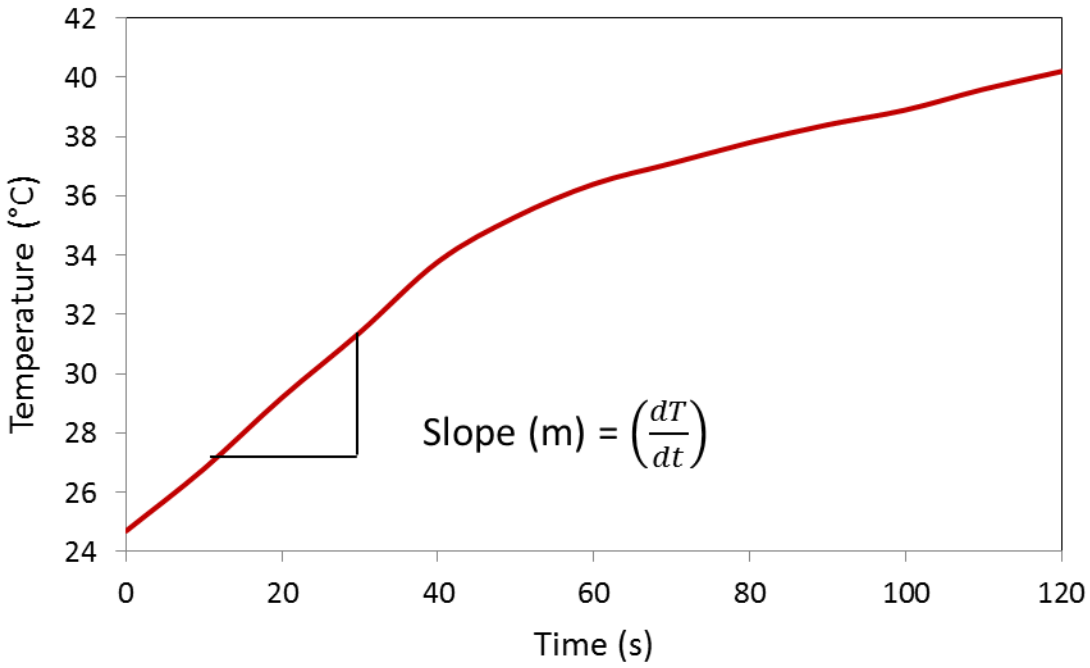

Figure 15: Example of heating rate measurement from experimental data

SAR was plotted as a function of magnetic field H and square of magnetic field H^2. Neel's relaxation theory states that SAR of superparamagnetic nanoparticles is proportional to the square of magnetic field and the adherence of the nanoparticle samples to this rule was evaluated by plotting SAR vs. square of magnetic field. The plot of SAR vs. magnetic field gives a correlation of the performance of a given nanoparticle under various magnetic fields.

4.2.3 Results: Heating Static Nanofluid

The temperature increase at 120 s for EMG 1400 and EMG 605 for various concentrations of iron oxide is given in Table 4 and Table 5 respectively.

Current	**Magnetic field**	**Temperature increase in 120 s**		
I(A)	**H (A/m)**	**(K)**		
		0.7 wt. %	**2.6 wt.%**	**5.4 wt.%**
10.4	245.4	2.4	7.4	15.5
15.2	358.7	4.2	11.8	23.2
20.4	481.4	5.5	16.4	29.3
25.5	601.8	6	20.7	32.5

Table 4: Summary of EMG 1400 dispersion heating result at concentrations of 0.7 %, 2.6 % and 5.4 % by weight of iron oxide at 450 kHz

Current I(A)	Magnetic field H (A/m)	Temperature increase in 120 s (K)		
		0.7 wt. %	**2.6 wt.%**	**5.6 wt.%**
5.1	120.4	0.7	2.4	5.3
10.1	238	2.1	7	14.9
15.2	358	3.5	14.8	32.8
20	472	5.4	20.1	42.2

Table 5: Summary of EMG 605 dispersion heating results at concentrations of 0.7 %, 2.6 % and 5.6 % by weight of iron oxide at 450 kHz

The data shows that the heating rate increases with the concentration of nanoparticles. It was observed that the temperature was linear with time initially i.e., constant heating rate, after which it decreased gradually. Hence, the initial linear temperature gradient was calculated as shown in Figure 15, and normalized for the concentration and specific heat capacity of the material. This gives the energy liberated per unit weight of the nanoparticle in Watt/gram, namely Specific Absorption Rate (SAR). The results for the various nanofluid samples are summarized in Figure 16.

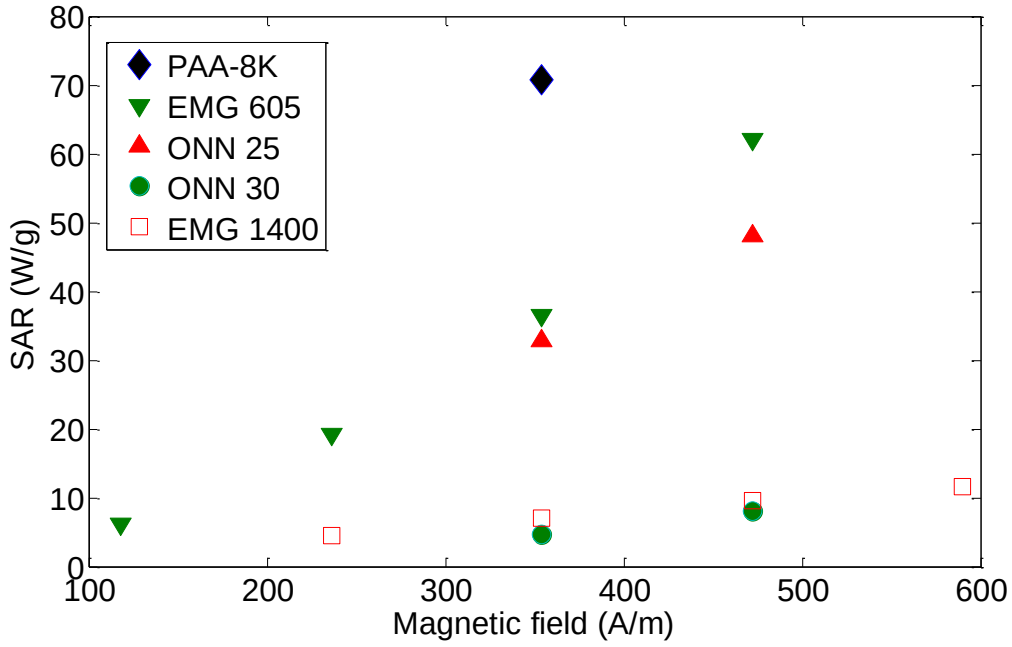

Figure 16: SAR vs Magnetic Field: Heating performance of nanofluid samples- PAA-8K, EMG 605, EMG 1400, ONN 25, and ONN 30

Varied performance of different samples of iron oxide shows that for a given weight of nanoparticle sample and magnetic field, there are other factors that affect heating, one of them being nanoparticle size. As shown in section 2.5 and section 3.2.1, SAR can be predicted given we know the size distribution and other intrinsic properties of the nanoparticle sample. Since, it is difficult to ascertain some of those properties such as magnetic anisotropy, comparison can be fairly made only for particles synthesized by the same method, having similar shape and structure, and hence whose properties are comparable. EMG 605 and EMG 1400 satisfy this criteria and hence are used for further investigations and comparison. Even though PAA-8K showed the best heating performance, its performance was difficult to compare due to its non-uniform shape and

unavailability of sufficient quantity of sample being in-house synthesized. Further, the concentration of the PAA-8K sample is not accurately known, with uncertainty on its SAR calculation. For comparison, SAR of EMG 605 and EMG 1400 are plotted as a function of square of magnetic field amplitude, as H^2, in Figure 17.

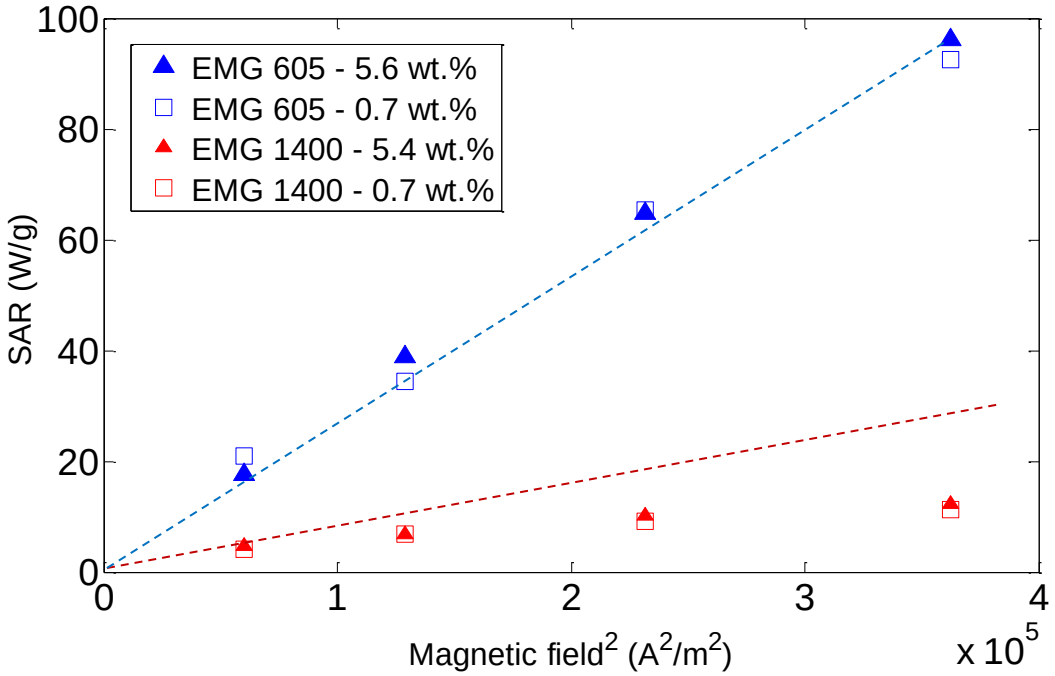

Figure 17: SAR of EMG 605 and EMG 1400 at various concentrations as a function of square of magnetic field amplitude; with dotted lines showing an ideal quadratic trend

It is seen that SAR for EMG 605 and EMG 1400 is independent of concentration from 0.1 – 6 % by weight. SAR of EMG 605 shows a good fit with square of magnetic field amplitude as predicted by equation (5), whereas EMG 1400 does not show the same correlation. For EMG 605 dispersion, SAR is proportional to 3E-4 H^2 and for EMG 1400 dispersion, SAR shows low fit with 3E-5 H^2. The dotted lines show the trend of a quadratic relation. It is believed that some aggregation of EMG 1400 particles may have

occurred, making them no longer superparamagnetic. Similar observations have been made by Davidson et al. (2012). With the aim of comparing heating performance of EMG 605 and EMG 1400, SAR values at different concentrations were averaged at each value of magnetic field and are shown in Table 6.

Magnetic field H (A/m)	**$SAR_{EMG\ 605}$ (W/g)**	**$SAR_{EMG\ 1400}$ (W/g)**	**$SAR_{EMG\ 605}$/ $SAR_{EMG\ 1400}$**
236	19.3	4.5	4.3
354	36.6	7.1	5.1
472	62.1	9.6	6.4
590	94.7	11.6	8.1

Table 6: Comparison of experimental SAR of nanoparticle dispersions EMG 605 and EMG 1400 at 450 kHz

Table 6 shows that EMG 605 has better heating performance than EMG 1400 by a factor of 4 to 8. This is in line with the prediction that SAR for EMG 605 should be better based on particle size distribution. However, based on particle size distribution it was predicted that the factor of $SAR_{EMG\ 605}$/ $SAR_{EMG\ 1400} \sim 5$ (see section 3.2.1). It is believed that agglomeration of nanoparticles, which resulted in EMG 1400 sample's deviation from a quadratic relation, might have also caused this deviation. But the reasons for the departure from equation (5) are not clear at present. Accurate quantitative comparison will require experiments with Fe_3O_4 nanoparticle samples of a known size distribution, and accurate measurement of the spatial distribution of magnetic field strength to which the sample is exposed, among other parameters.

4.2.4 Results: Heating Static Fluid in Nanopainted Vials

The ability of nanopaint on the inner wall of a container to raise the temperature of static water is recorded and shown in Table 7 and Table 8.

Current	Magnetic field	Temperature increase in 180 s		
I(A)	H (A/m)	ΔT (K)		
		2.48 wt.%	**7 wt.%**	**12.9 wt.%**
10.4	245.4	0.5	0.8	1.1
20	472.0	0.6	1.4	2
15.3	361.0	0.4	1.1	1.7
25.2	594.7	0.7	1.5	2.7

Table 7: Summary of EMG 1400 nanopaint heating results at concentration of 7 % and 12.9 % by weight of iron oxide in paint at 450 kHz

Current	Magnetic field	Temperature increase in 180 s		
I(A)	H (A/m)	ΔT (K)		
		6.4 wt.%	**13.9 wt.%**	**14.69 wt.%**
10.4	245.4	2.5	2.7	4.2
20	472.0	9.2	9.1	14.2
15.3	361.0	5.6	6.5	8.5
25.2	594.7	12.9	14.3	19.4

Table 8: Summary of EMG 605 nanopaint heating results at concentration of 6.4 % and 13.9 % by weight of iron oxide in paint at 450 kHz

These tables show the temperature increase of a static water sample by EMG 605 and EMG 1400 nanopaint at different magnetic fields. This temperature increase was expressed in terms of SAR using equation (7). SAR of nanopaint is plotted as a quadratic function of magnetic field in Figure 18. It is seen that SAR for EMG 605 nanopaint and EMG 1400 nanopaint is independent of concentration up to 6 % by weight. However at higher concentrations up to 14 % by weight, there is a decrease in heating performance.

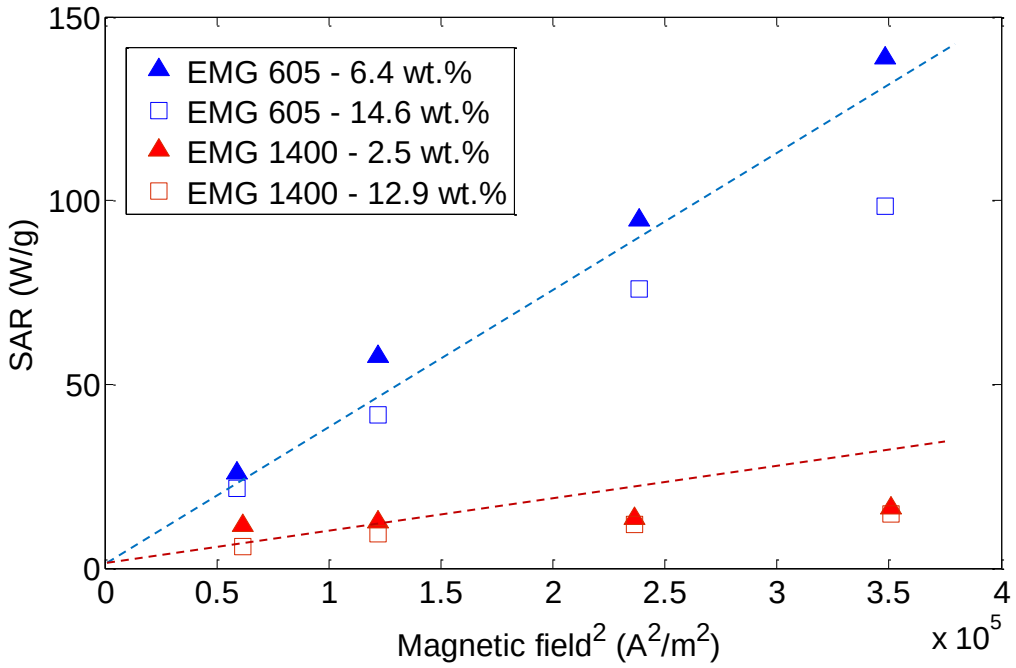

Figure 18: SAR of EMG 605 nanopaint and EMG 1400 nanopaint at various concentrations, as a quadratic function of magnetic field; with dotted lines showing an ideal quadratic trend

Thus, there is a threshold concentration above which increasing concentration does not result in a proportionate increase in heating. As in dispersions, SAR shows a

square dependence on magnetic field amplitude and performance of EMG 605 nanopaint is better than EMG 1400 nanopaint. Hence, SAR correlation given by equation (5) can also be applied to nanopaint.

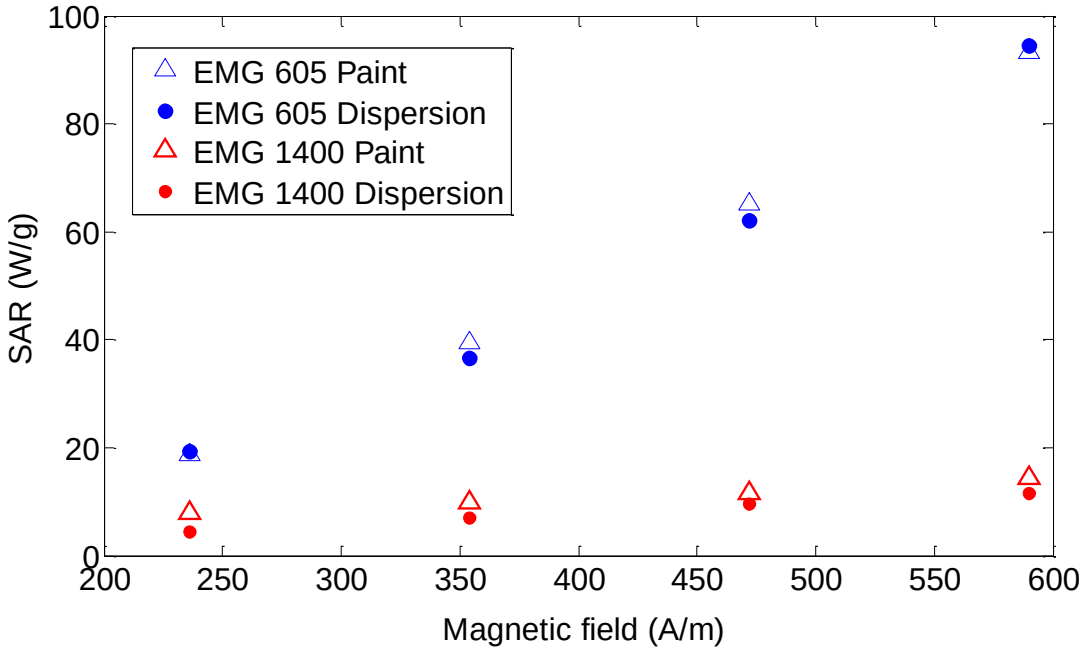

Figure 19: Summary of heating performance of EMG 605 paint and dispersion, and EMG 1400 paint and dispersion at magnetic field of 200 to 600 A/m and 450 kHz

The averaged SAR values of EMG 605 and EMG 1400 dispersion and nanopaint are plotted as a function of magnetic field amplitude in Figure 19. The dotted lines indicate the trend that a quadratic relation would follow. It is seen that SAR for nanopaint is similar to dispersions at a given magnetic field and frequency. There is a slight deviation but this may be due to experimental error. It is generally concluded that nanoparticles in liquid and in paint follow the same heating trend. Neel's relaxation

theory has been used to explain heating performance of SPM-NPs in dispersion. We show that nanoparticles embedded in solid (nanopaint) show the same heating performance as dispersion. Hence, it is concluded that Neel's relaxation theory is applicable to nanopaint. Further, we see that EMG 605 shows superior heating performance and hence is used for further experiments and calculations. For EMG 605, SAR is proportional to 1.3E-3 $H^{1.76}$ and this correlation can be used to predict SAR for different magnetic fields.

4.3 FLOW EXPERIMENTS

Flow experiments were performed at 630 kHz in a five-turn coil (horizontal configuration) by varying magnetic field between 300 to 1000 A/m. A long tube with inner diameter 1.6 cm and length 24 cm was coated with EMG 605 paint at a concentration of about 2.5 % by weight. The tube wall was bored at equal intervals to place three temperature ports, as shown in Figure 20. The experimental setup is shown in Figure 21. The tube was insulated with urethane foam which is magnetically non-responsive and placed inside the coil. It was connected to an HPLC pump in an open loop setting and flow rates were varied between 0.5 to 5 mL/s. The volume of the nanopainted pipe and the volumetric flow rates were used to calculate the residence time of the fluid inside the pipe. Temperature was measured at different points on the pipe, with the probe centered at the axis of pipe.

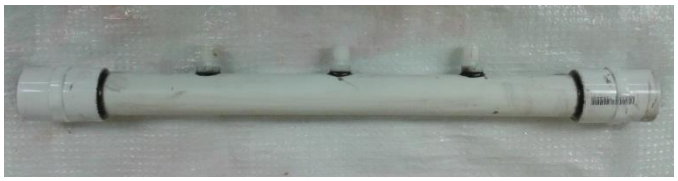

Figure 20: A long tube of inner diameter, ID = 1.6 cm and length, L = 24 cm with temperature ports; coated internally with EMG 605 nanopaint.

The magnetic field was calculated using equation (3). The temperature increase of the flowing water by nanopaint at different flow rates and magnetic fields is quantified in terms of SAR_{flow} by equation (8).

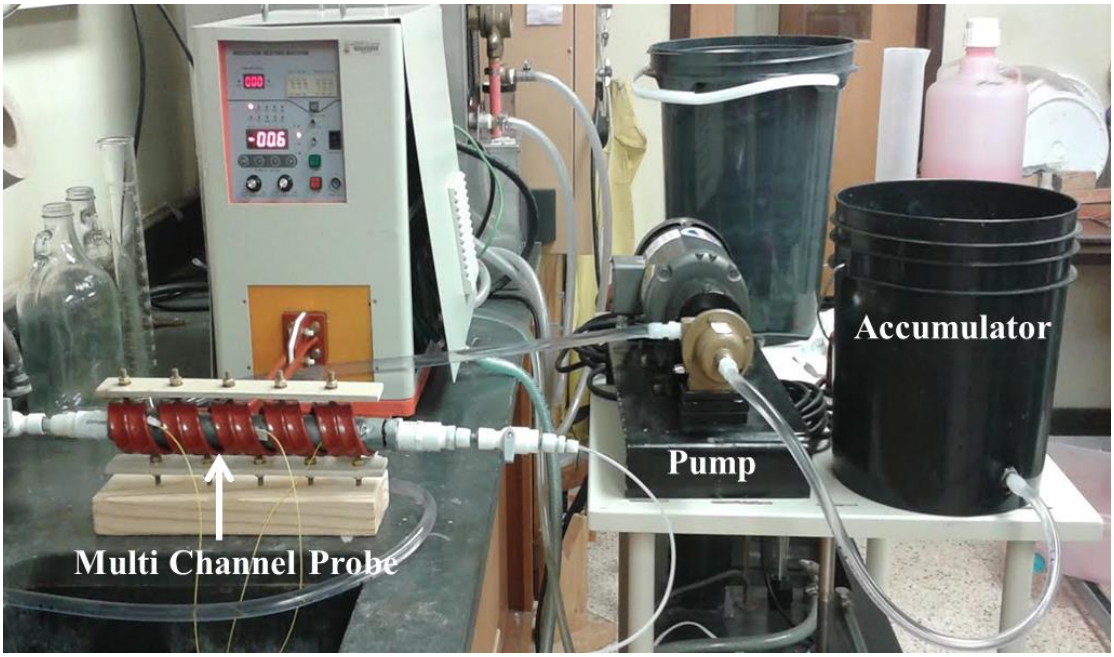

Figure 21: Flow experiment setup shows a long nanopainted tube in a 5 turn coil, connected to a HPLC pump in an open-loop

4.3.1 Results: Heating Flowing Fluid through Nanopainted Pipe

SAR_{flow} is plotted as a function of residence time at different magnetic fields in Figure 22. It is seen that SAR_{flow} is maximum corresponding to certain 'optimum' residence time at different magnetic fields. This indicates that some time is required for complete heat dissipation from the paint medium to water. At these peak points, SAR_{flow} is higher than SAR for static experiments by a factor of ~ 5 to 8, depending on magnetic

field. For instance, at 500 A/m, EMG 605 paint showed SAR of 70 W/g compared to 500 W/g for flow experiments.

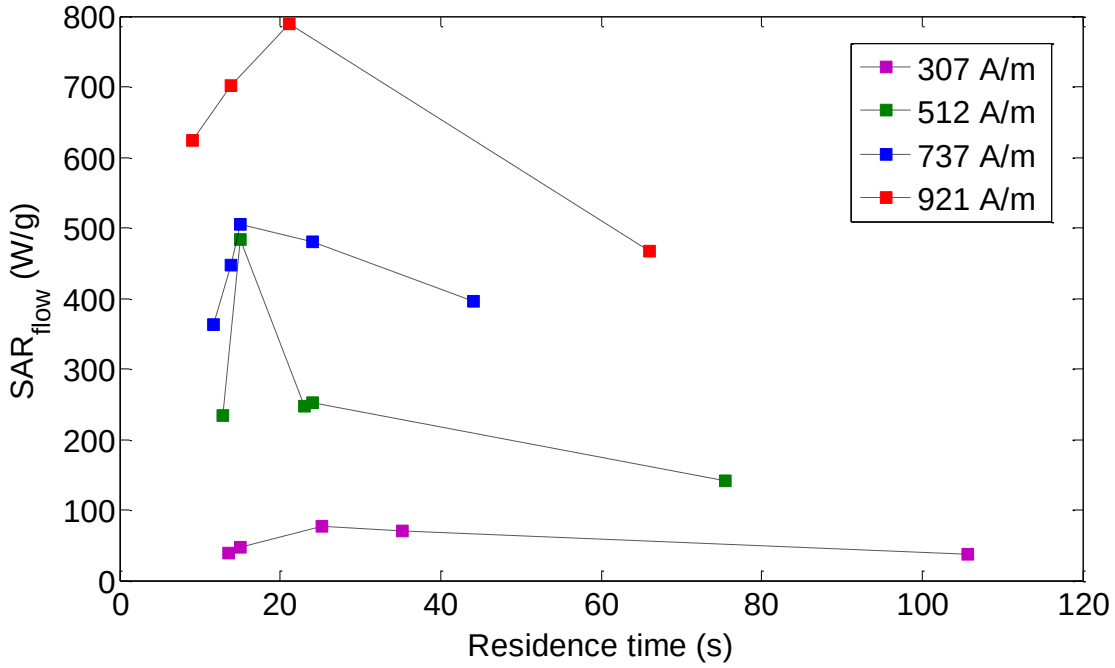

Figure 22: SAR of flow experiments as a function of residence time for different magnetic fields from 300 to 1000 A/m

It is hypothesized that in static experiments, the high temperature in and around the nanoparticle due to slow heat dissipation from surface of paint decreases SAR. Low thermal conductivity increases temperature locally at the surface of paint, which decreases heating performance of nanoparticles, as indicated by equation (5). In flow experiments, flow of fluids maintains conducive temperature at surface of paint for effective heat generation and conduction. Thus, it is seen that flow-induced mixing facilitates better heat transfer.

4.4 Wax Coupon Experiments

Since our application is wax removal from pipelines, we evaluated the feasibility and efficiency of nanopaint to melt wax deposited on its surface by a simple experiment. Experiments were performed at 630 kHz in a five-turn coil (horizontal configuration) by varying magnetic field between 300 to 1000 A/m. The wax was deposited on a layer of nanopaint, coated on a rectangular polycarbonate slab. The procedure of creating a wax coupon is shown in the Figure 23.

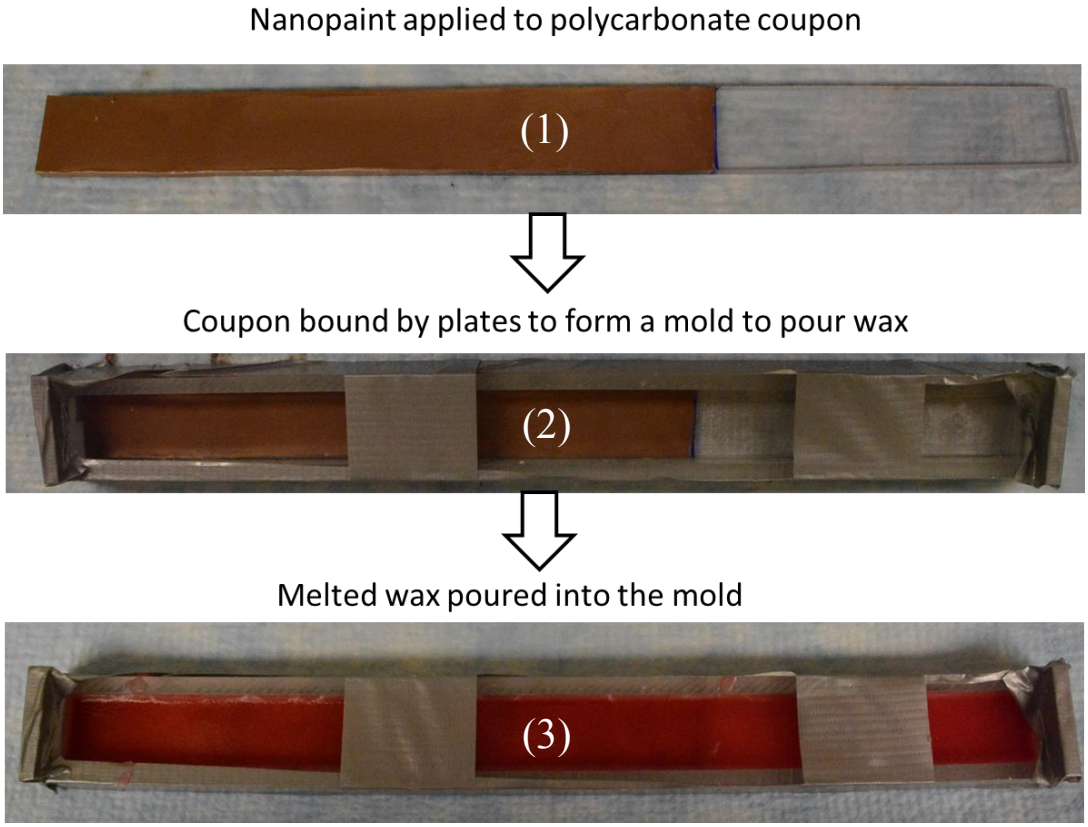

Figure 23: Schematic for creating a wax coupon on a nanopaint-coated polycarbonate slab: (1) Nanopaint (brown) is applied to a side of polycarbonate coupon (slab), (2) Coupon is bounded by similar polycarbonate slabs to form a cuboid mold and (3) Melted colored paraffin wax is poured into the mold and left to cool

A rectangular polycarbonate slab of dimensions 36 cm x 2.5 cm x 0.5 cm was used as a coupon for this experiment. Initially, nanopaint was applied to a side of the slab, 23 cm x 2.5 cm in dimension. After drying, the slab was bounded by similar polycarbonate slabs and plastered into place to form a hollow cuboid mold. The paraffin wax used has a melting point of 323 K was used as a representative of the pipeline wax deposit. Red-colored paraffin wax was melted and poured into the mold and left to cool for about 1-2 hours.

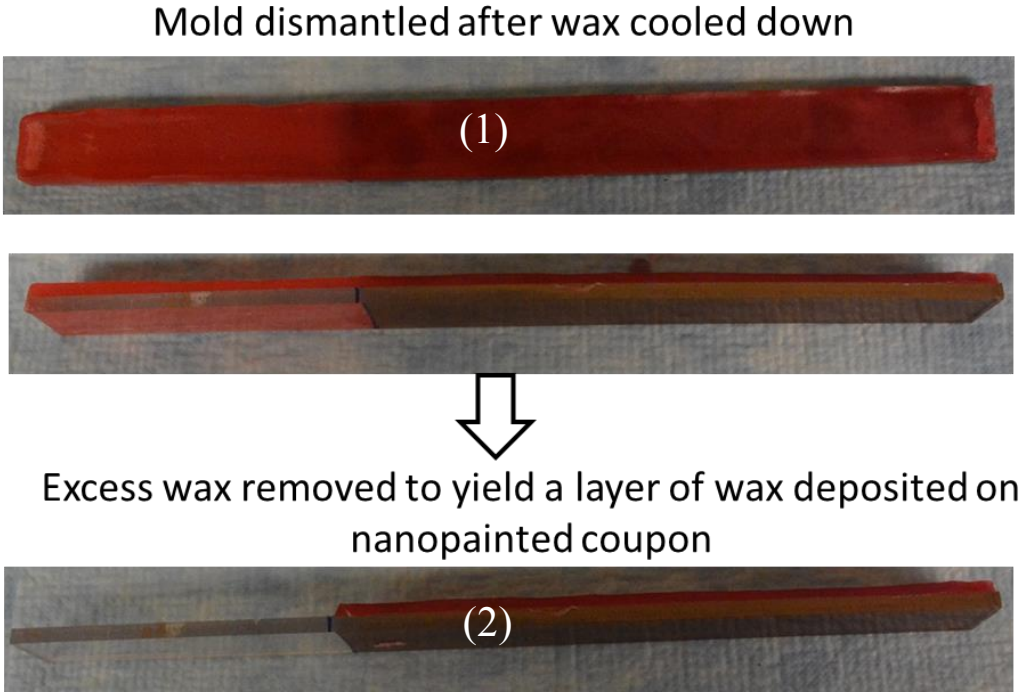

Figure 24: Formation of uniform layer of paraffin wax on nanopaint-coated slab: (1) Mold was dismantled after wax cooled, and (2) Excess wax was removed from the non-painted portion of polycarbonate coupon

After cooling, the cuboid mold was dismantled as shown in Figure 24. Only the wax in contact with nanopaint is required and so the remaining wax was carefully

removed. The weight of the wax on the coupon and thickness of wax layer was recorded. The nanopainted wax coupon so obtained was used for experiment. The above procedure was repeated to obtain several coupons, of different average thickness ranging from 5 to 15 mm.

The wax coupon was inserted into the 5-turn coil and held by a metal clamp-stand. The coupon was so positioned that the entire wax portion was inside the coil. Probes were inserted in three different locations, at the contact of nanopaint-wax surface to measure temperature. The setup is shown in Figure 25. The induction heater was turned on and the rate of temperature increase of the surface, for wax to reach its melting point was recorded. The procedure is repeated for different magnetic fields and different wax thickness.

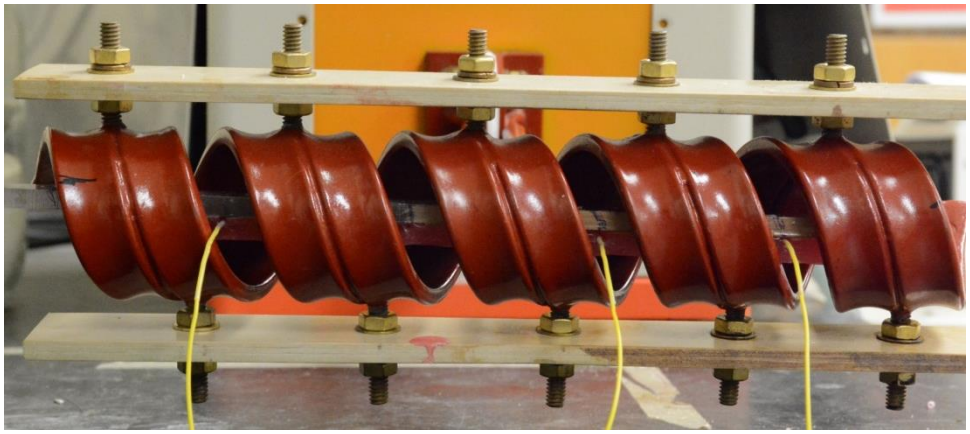

Figure 25: Wax coupon with temperature probes at the nanopaint-wax contact surface, placed inside a 5-turn coil

These experiments are different from the static and flow experiments, in the sense that they involve surface heating as opposed to bulk heating. SAR, defined previously,

quantifies heating behavior of nanoparticles in a bulk medium. In order to understand surface heating behavior of nanopaint, we do not have a quantification parameter. Hence, we compare the heating of two different materials by nanopaint to that of nanopaint-air surface heating, to see if there is a common trend. We use PDMS (Polydimethylsiloxane) as the second material, as it is a polymer that can be melted and molded, much as same as wax. The melting point of PDMS is 313 K. A procedure similar to the wax case was used to form a transparent PDMS coupon on a polycarbonate slab, as shown in Figure 26. Temperature probes were placed at the same intervals as the wax coupon cases. The induction heater was turned on and the rate of temperature increase of the PDMS-nanopaint surface was recorded. In addition, the temperature increase of the nanopaint surface alone without any deposit was recorded under conditions of complete insulation. This was used as a base case for comparison of the results.

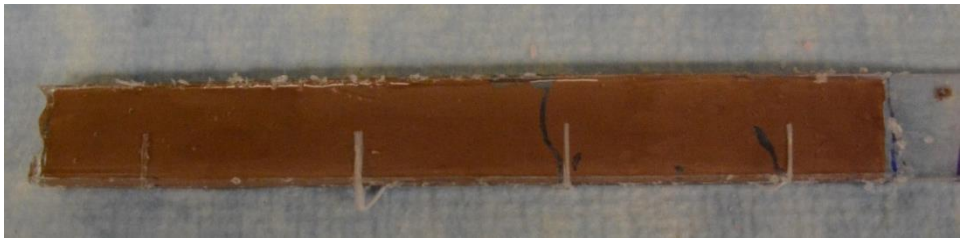

Figure 26: A layer of PDMS deposited on a nanopaint-coated polycarbonate slab shows relative position of surface temperature probes

4.4.1 Results: Heating Wax and PDMS by Nanopaint

For the wax coupon experiment, it was observed that at about 323 K (melting point of wax), wax melts and falls off the coupon, and the heating time was constant for different wax thickness (5 to 15 mm) at the same magnetic field. For instance, the time

taken to melt wax at 725 A/m was between 540 s to 660 s. It was concluded that the heat mainly melted a thin wax layer in proximity to nanopaint and hence wax layer thickness does not affect its removal. This encouraging result serves as a proof of concept for effectiveness of nanopaint-induced removal of wax deposit.

Next, based on the surface temperature probe readings, the heating rates of the nanopaint surface, nanopaint- wax surface and nanopaint-PDMS surface were recorded and shown as a function of magnetic field, as in Figure 27.

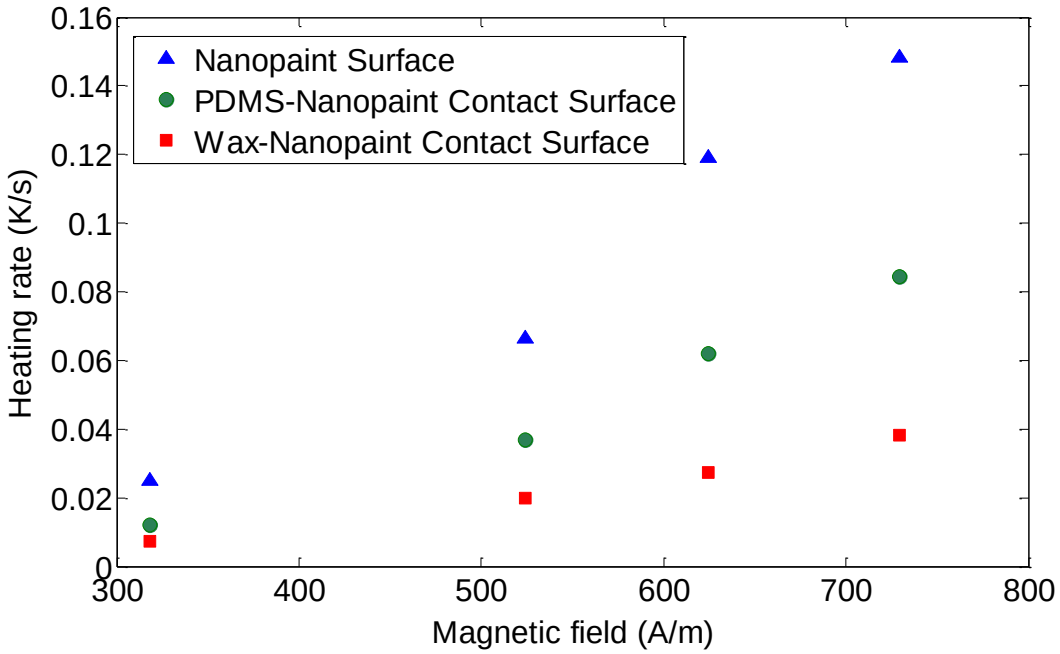

Figure 27: Heating rates of nanopaint surface, nanopaint- wax surface and nanopaint-PDMS surface at magnetic fields of 300 to 800 A/m and 630 kHz

It is seen that there is a constant factor of 1.75 – 2.1 between heating nanopaint to heating PDMS-nanopaint surface. Similarly, there is a constant factor of 3.5-4 between

heating nanopaint to heating wax-nanopaint surface. In earlier heating experiments, heating performance was directly influenced by the specific heat capacity of the material, as described by SAR definition. Hence, we believe that the surface heating experiments might show a similar dependence. A comparison between their specific heat capacities showed that wax/air ~ 3.5 and PDMS/air ~ 1.5, which are similar to the experimental factors. Hence, we believe that surface heating by nanopaint depends on the specific heat capacity of the material. However, it differs from bulk heating as in the heating occurs on the surface and hence is not affected by the volume of material. In order to quantify the effect of nanopaint for surface heating of wax, it will be more useful to consider nanopaint as a heat source and evaluate its effect on its surroundings. This concept will be utilized in the COMSOL model of nanopaint heating in pipelines in Chapter 5.

4.5 Factors Affecting Heating Performance of Nanopaint

As we have analyzed heating performance of nanopaint for static and flow systems and heating bulk and surface medium, we now consider factors that might affect heating performance of nanopaint such as thermal property and low ambient temperatures.

4.5.1 Thermal Property

The effect of thermal property (thermal conductivity, specific heat capacity) of nanopaint on its heating performance was evaluated using the 3-turn coil, static experiment setup. The thermal property of paint was varied by using metallic additives of high thermal conductivity and low specific heat capacity, such as silver and graphite. Two different paint samples were prepared from a standard nanopaint of 2.5 % by weight of iron oxide nanoparticles. The samples were added with 5 % by weight of silver nanoparticles from US Nano and 6 % by weight of graphite powder from Sigma Aldrich,

respectively. While it is important to quantify the effect of an additive on the thermal property of the standard nanopaint, we did not have the means to measure thermal conductivity of the paint. The effect of additive on another thermal property, specific heat capacity, can be quantified employing the mixing rule given by equation (11).

$$c_{DP} = c_D \times w_D + c_P \times (1 - w_D), \quad (11)$$

where c_{DP} is the specific heat capacity of nanopaint with a metallic additive(W/m.K), c_D is the specific heat capacity of the dopant (W/m.K), w_D is weight fraction of additive in paint and c_P is the specific heat capacity of the standard nanopaint (W/m.K). The specific heat capacity of silver-added paint and graphite-added paint was calculated to be 0.88 J/g.K and 0.89 J/g.K while that of standard nanopaint was 0.92 J/g.K. Additive-added nanopaint was applied to three identical vials each for sake of reproducibility as shown in Figure 28.

Figure 28: Glass vials painted internally with standard nanopaint, graphite-added nanopaint and silver-added nanopaint respectively

The two samples were compared with the standard nanopaint with no additives. These painted vials were filled with 2g of DI water and placed inside hollow glass cylinders for stability. These were placed at the center of the coil and temperature was

measured using fiber-optic temperature probe as shown in Figure 29. The ability of additive doped nanopaint on the inner wall of a container to raise the temperature of static water is expressed in terms of SAR using equation (7).

Figure 29: Setup to evaluate effect of thermal conductivity on nanopaint heating performance

SAR of silver-added nanopaint, standard nanopaint and graphite-added nanopaint is plotted as a function of magnetic field in Figure 30. It is seen that heating rates and SAR of silver-added nanopaint is similar to standard nanopaint whereas graphite-added nanopaint shows smaller SAR compared to the standard. It is believed that interaction between the larger graphite particle with iron oxide nanoparticles may have resulted in aggregation and thus suppressed heating performance. The concentration of the additive is small compared to the medium of the nanopaint and hence, the specific heat capacity is mainly driven by the nanopaint material which is epoxy in our case. Hence, it would be more effective to control specific heat capacity values by changing the medium of the nanopaint.

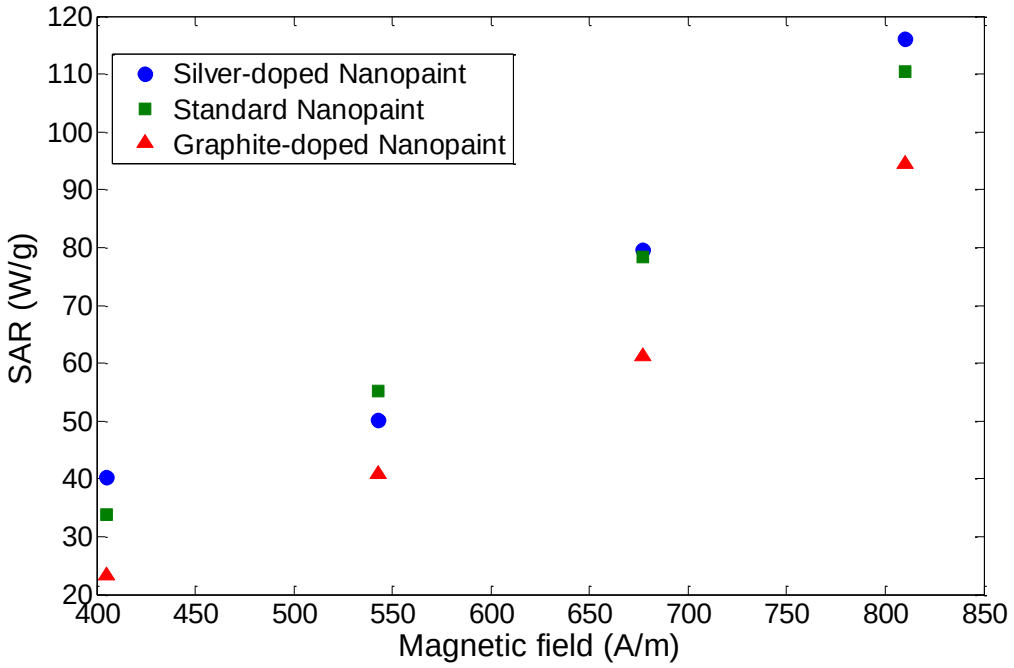

Figure 30: SAR of silver-added nanopaint, standard nanopaint and graphite-added nanopaint as a function of magnetic field at 450 kHz

An important point to note here is that a lower value of specific heat capacity does not necessarily produce more heat but produces higher heating rates. This is because the material requires lesser amount of heat to cause a unit rise in temperature. Variation of thermal property of nanopaint might be particularly useful if the time of heat delivery is an important parameter. In general, it can be concluded that for the scale of our experiment, small increases in specific heat capacity do not affect heating rate of nanopaint.

4.5.2 Low Ambient Temperatures

In the application of flow assurance in subsea pipelines, nanopaint may be subjected to low ambient temperatures. Hence we evaluate the effect of low ambient temperatures on heating performance of nanopaint using the setup shown in Figure 31.

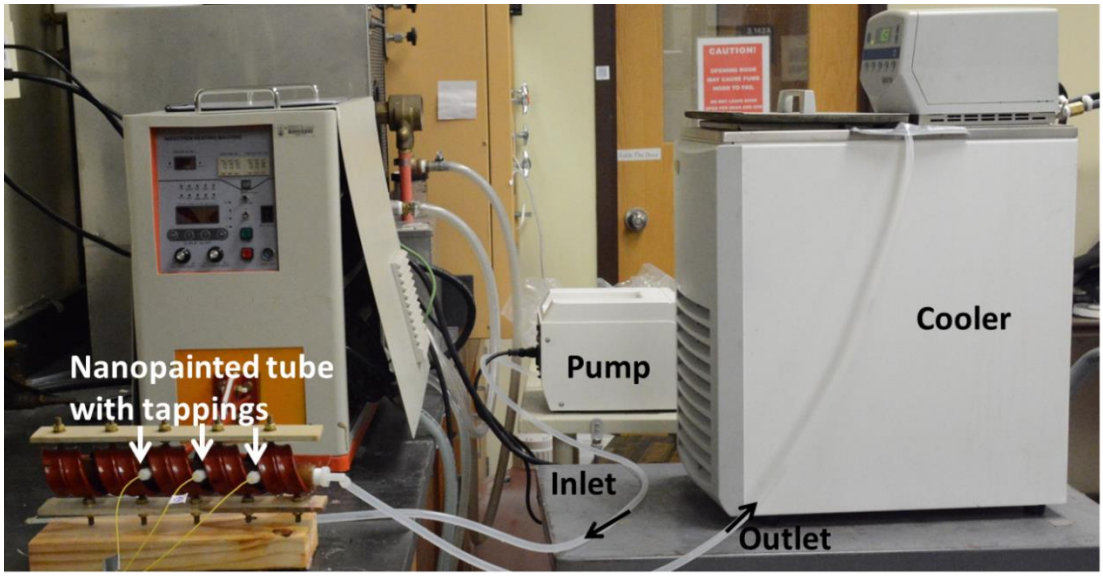

Figure 31: Setup to evaluate effect of low ambient temperature on heating performance of nanopaint

An tube made of ultem, a magnetically inert material, was coated with nanopaint which contains 2.6 % by weight of EMG 605and placed inside the 5-turn coil, as shown in Figure 31. The tube was sufficiently insulated with glass wool and was connected to a water cooler, via a piston pump. This arrangement was used to fill the tube with cold water at a particular temperature. The cooler could go to a minimum temperature of 10 °C. Once the tube was filled with cold water, the inlet and outlet ends of the tube were clamped to conduct a static test, as shown in Figure 32. The induction heater was

operated at a frequency of 630 kHz and current of 10 to 40 A. The current is varied and the temperature rate of the cold water is measured over a wide temperature range.

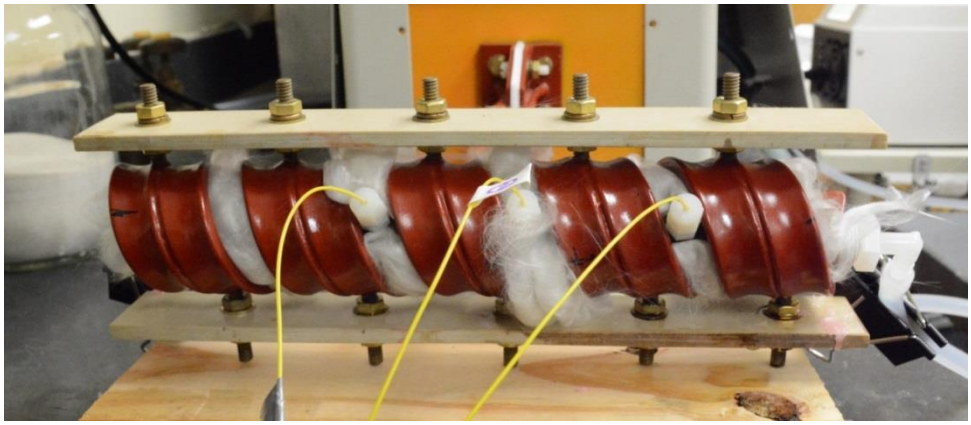

Figure 32: Insulated nanopainted tube containing cold water under static conditions

The temperature of the water is plotted as a function of time for different magnetic fields in Figure 33. It is seen that at a magnetic field strength of 830 A/m, the temperature follows a linear trend for a wide range of temperature from 15 °C to 45 °C. This shows that heat generation rate is constant over time. At 625 A/m and 522 A/m, we see a slight dip in the slope at higher temperatures. However, the lower temperatures between 10 °C to 25 °C do not significantly affect heating performance of nanopaint. Hence, it is concluded that the heating performance correlation shown in Figure 19 can be applied to systems at an ambient temperature of 10 °C to 45 °C. However, heating performance might decrease significantly at higher temperature and this factor needs to be considered, when the application is for a high-temperature setting.

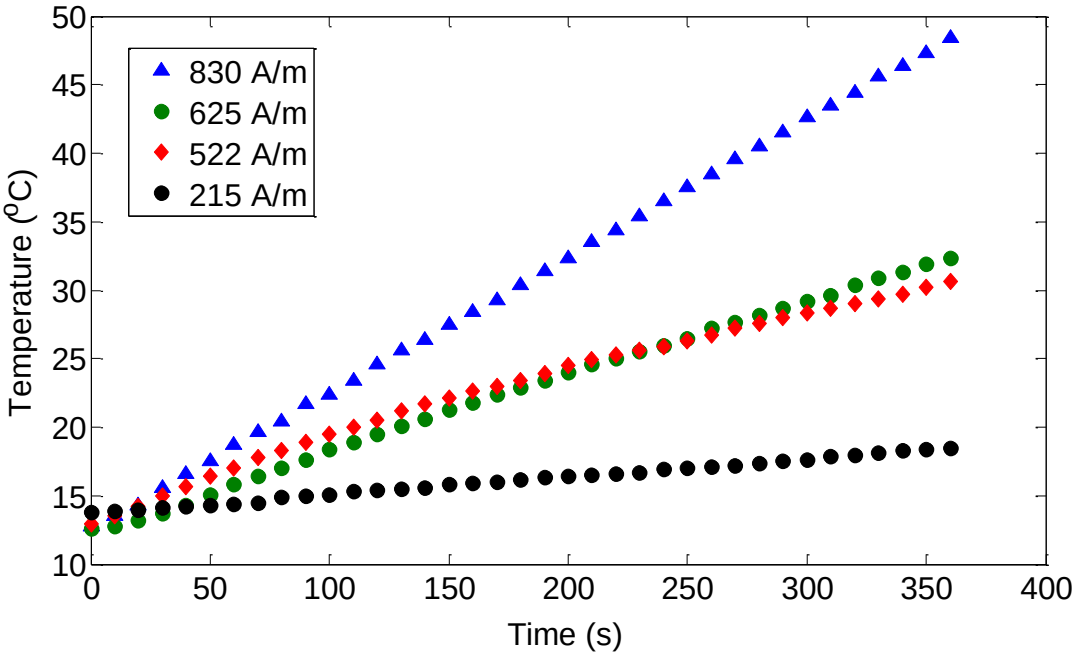

Figure 33: Heating rate of nanopaint – water system under low ambient temperature of 10°C at a magnetic field of 200 to 850 A/m and 630 kHz

4.6 Translation of SAR Experimental Results to Real Systems

We have seen SAR results of different nanoparticle samples, under various magnetic fields, frequencies and ambient temperature. Next, we discuss the limitation of SAR interpretation and its application to different systems.

4.6.1 Limitation of nanoparticle loading

It is seen that SAR is independent of concentration up to a maximum concentration of about 5 – 7 % by weight for nanoparticle dispersions and about 13 % by weight for nanopaint. Previous work in this field has focused on maintaining nanoparticle concentration as low as possible, for the sake of human treatment. For our nanopaint application, a high loading of the nanoparticles will be more effective. However, there

would be an upper limit to the concentration of nanoparticles in a system, not only because the heating efficiency tends to decrease at very high concentration but also due to the cost. This is because as nanoparticle loading increases, the amount of heat generated increases which however, cannot be readily transferred to the system. In our case, the nanopaint may not efficiently transfer the excess heat to the system and this would lead to an increase in the temperature of the nanopaint. This rise in temperature further decreases the heating performance of nanoparticle in the nanopaint or in a fluid, as per Neel's relaxation theory. A high thermal conductivity system would remedy this difficulty.

4.6.2 Limitation of SAR Definition

SAR by definition is the amount of energy liberated per unit weight of nanoparticle. As described in section 4.2.2, this can be measured by temperature increase of the system. However, temperature increases linearly with time initially, after which its heating rate decreases gradually as shown in Figure 15. SAR is thus usually calculated using the heating rate in the linear region; and hence it is not a true indication of the overall heating capability of the nanoparticle-containing system. Thus the SAR correlation generally holds true if the time of the process is of a shorter duration, about 300 – 400 s for fields of 100 to 1000 A/m. This is important to be considered for implementing the results to any system.

4.6.3 Application of SAR to Heating of Different Liquids

SAR is a constant value for a given nanoparticle sample and, consequently, for heating different systems under similar conditions. An experiment was conducted to test this hypotheses. A static experiment setup was used to evaluate and compare heating of decane and water by nanopaint in two different trials. Insulated glass vials coated with nanopaint of about 2.5 % by weight of iron oxide (EMG 605 sample) were used to heat

the same quantity of decane and water. Decane has a specific heat capacity of 3.2 J/g.K while water has a specific heat capacity of 4.18 J/g.K. The temperature was recorded at the center of the vial and used to calculate SAR using equation (7). A plot of SAR of the two systems as a function of magnetic field is shown in Figure 34.

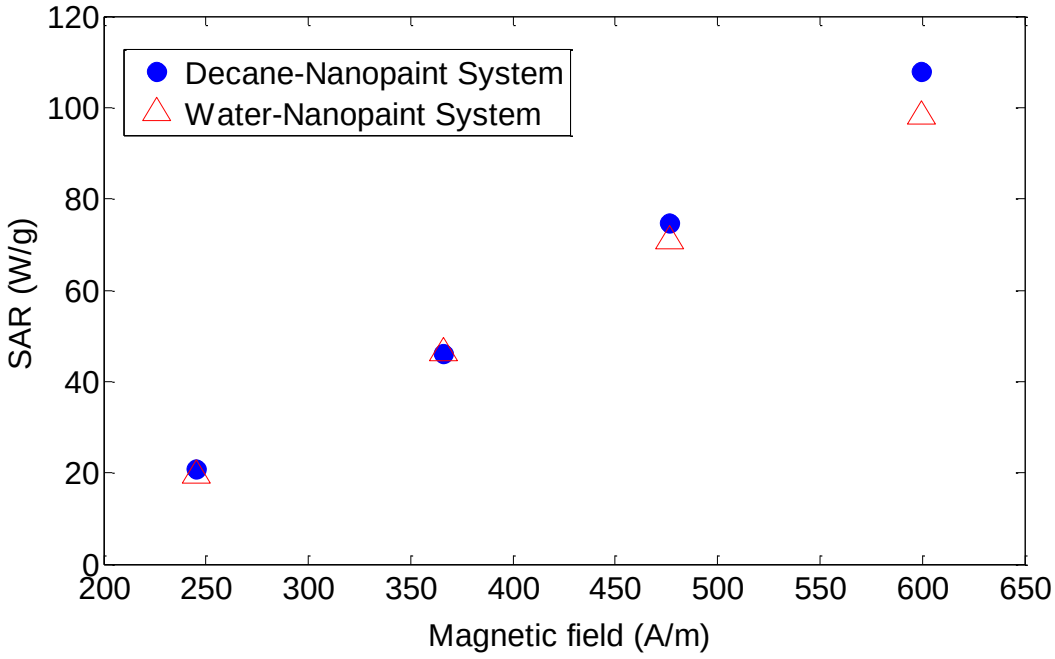

Figure 34: Comparison of SAR results for decane-nanopaint and water-nanopaint systems at magnetic fields of 200 to 700 A/m and 450 kHz

Figure 34 shows that for the same nanopaint and magnetic field, SAR is fairly constant for the decane and water systems. This shows that the heat generated by nanopaint is the same and does not depend on the contact medium. Thus, it can be concluded that the SAR correlation shown in Figure 19 can be applied to different liquids.

Chapter 5: Implementation of Nanopaint Heating to Subsea Pipelines

The technology described in the preceding sections can be applied for flow assurance in subsea pipelines. Wax deposition is a common problem in crude oil pipelines (Minami et al. 1999). The conditions and process of wax deposition have been widely studied (Kok & Saracoglu 2000; Huang et al. 2014). Crude oil being a mixture of hydrocarbons of different molecular weight and boiling point, some of the heavier components tend to precipitate out below certain critical temperatures in the form of wax. This effect is more pronounced in subsea pipelines. These are at depths of 3000 m (or more) below sea level and at temperatures of 2 °C to 10 °C. These conditions induce a temperature gradient between the pipeline and its surroundings and hasten the process of wax formation. The wax formed tends to deposit on the inner walls of the pipelines, forming a hard deposit with time that constricts the flow of fluids. For safety and operational reasons, it is important to remove the deposits frequently. Common methods of removal have been discussed in Chapter 1. In this chapter, we will discuss the removal of wax deposit from steel pipelines using nanopaint technology. First we discuss the methods of magnetic field delivery to nanopaint, followed by a discussion of the feasibility of magnetic field generation and propagation in pipelines. Then, we explain the concept of the proposed delivery system followed by modeling and optimization of the system, in terms of power and cost requirement.

5.1 Application: Removal of Wax Deposits From a Nanopainted Subsea Steel Pipeline

This application requires that nanopaint be coated on the interior walls of steel pipeline, primarily during pipeline engineering. The nanopaint-coated pipeline with wax deposit is schematically shown in Figure 35. This nanopaint is subjected to an alternating magnetic field by a magnetic field generator. Details about the magnetic energy delivery

system will be discussed further in this section. The generated magnetic field heats up the surface of the nanopaint via Neel relaxation, which in turn heats and melts the wax in contact with it. Thus, this provides a non-abrasive, chemical-free method for wax removal from pipelines.

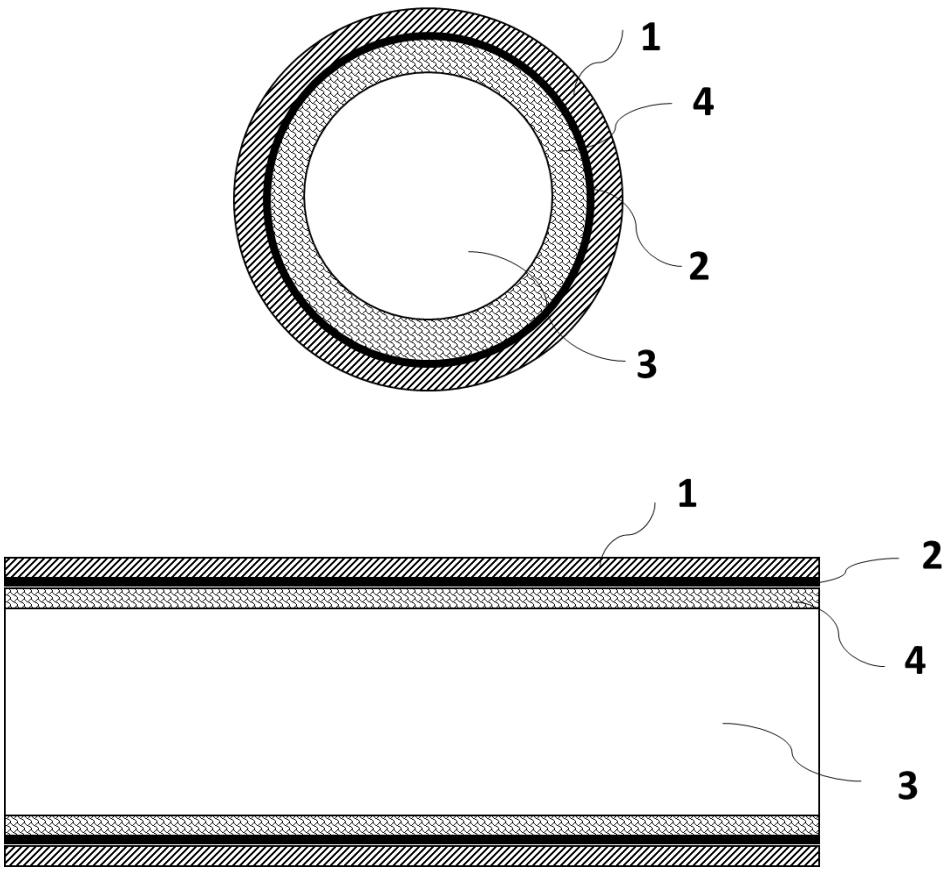

Figure 35: Front view (above) and side view (below) of a subsea steel pipeline (1) coated with nanopaint (2). It carries crude oil (3) which cools down and results in wax deposition (4) over time

Next, we briefly discuss details of the magnetic field generator device.

5.1.1 Design of Magnetic Field Generator

A literature survey was conducted to examine existing technologies to design and build a portable magnetic field generator, with a view to develop a similar generator that can be inserted and operated inside the steel pipelines. Several technologies will be briefly discussed here.

Bologna (2001) describes a portable device that can deliver an alternating magnetic field to human body. The device consists of a casing that houses a generator and a battery-powered electromagnet. The core contains a battery and has a coil wound on it coaxially. The generator consists of a CPU (central processing unit) that programs the oscillator to generate waves at a particular frequency. The generator is provided with a microprocessor capable of generating harmonics of a particular frequency. The generator can be turned on by a push button. These waves are fed to the coil, thus generating a magnetic field oscillation of a prescribed frequency.

Turner et al. (2010) describes the design of an electromagnetic applicator for hyperthermia treatment, capable of producing frequencies from 100 KHz to 1 MHz. The design consists of a transparent applicator with conformable face that supplies magnetic energy to the tissue. It has an antenna that connects to a generator/battery system and generates the magnetic wave. The device is made highly dielectric (using deionized water) to allow for effective transmission of field outside the device rather than inside itself.

Boddie et al. (1987) describes an apparatus for producing precisely controlled electromagnetic fields in the radio-frequency (RF) range. The device consists of a pair of inductor rings placed between capacitor plates. Spatial orientation of the rings and phase of the current flowing through the rings can manipulate the magnetic field. Helmholtz configuration, which consists of two electromagnetic placed co-axially, will concentrate

the field at the center of the rings while some other configurations like wedge will shift the field outside the rings. Hence design of the coil is important for maximizing magnetic field at a desired location. The capacitor plates act as generators. An RF generator provides power to the inductor rings via an amplifier and inductance coupler. The frequencies can be varied from the KHz to MHz range using different generator or amplifier specifications.

Surducan et al. (2012) describes the use of a magnetron to generate microwaves. A magnetron is a device that uses electric and magnetic fields to generate electromagnetic waves. A hot cathode generates electrons by means of thermionic emission in a cavity. A constant magnetic field prevents electrons from leaving the cavity and concentrates them on the inner surface of the cavity (anode). This acts as the inductor and leads to generation of electromagnetic field. The magnetron is placed on the waveguide and coupled co-axially to generate a field.

The technologies described above show the feasibility and design considerations for a portable magnetic field generator. The main design considerations are to be given to the coil, oscillation generator, magnetic and electric properties of material of construction and battery power. These can be modified with the objective of achieving desired frequencies and field strength at the location of interest. Next, we will look at the feasibility and effects of generating electromagnetic fields inside a steel pipeline.

5.1.2 Theory: Electromagnetic Fields in a Cylindrical Pipeline

We now consider the generation and propagation of electromagnetic field in a steel pipeline. The design and limitations of a metal waveguide have been previously studied (Harrington et al. 1995; Holloway et al. 2000). Here, we discuss the theory of electromagnetic wave propagation and attenuation in a pipeline. The pipeline is modeled

as a circular waveguide with perfectly conducting wall. The cylindrical coordinate system (ρ, ϕ, z) is used to describe positions within the waveguide. Figure 36 shows the coordinates of the pipeline, where ρ is the radial distance (m), ϕ is the azimuthal angle, and z is the distance along the axis (m).

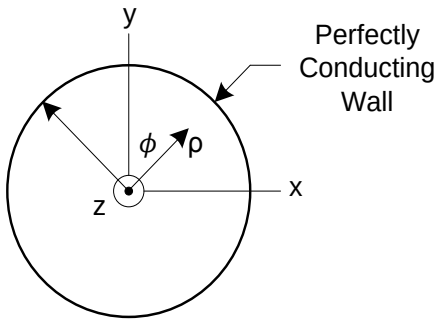

Figure 36: Coordinates of a circular waveguide

There are two types of electromagnetic modes that can propagate along the z axis of the circular waveguide:

- The Transverse Electric to z modes (abbreviated TE^z) and
- The Transverse Magnetic to z modes (abbreviated TM^z)

The TE^z modes can be excited by one or more magnetic dipoles (coils) whose moments (a vector pointing in a direction perpendicular to the planes of the windings with magnitude equal to current x area of circular winding x number of turns) are aligned with the z axis. The TM^zmodes can be excited by one or more electric dipoles (current carrying wires extending parallel to the z axis). The vector moment of an electric dipole has a magnitude equal to the current flowing in the wire, times the length of the wire and a direction that points in the direction of the wire extension.

Both modes can produce magnetic field components tangent to the waveguide wall (covered with nanopaint). The propagation characteristics of all electric (E) and magnetic field (H) components associated with these two modes are determined by the boundary conditions that a relevant component of the electric field (E_ϕ and E_z) tangent to the perfectly conducting waveguide wall equals zero. The theory for this section was obtained from Balanis (1989).

TE^z Modes

First, we consider the TE^z modes, which can be characterized with the spatial distribution of the electric field, E_ϕ . The boundary condition for $E_\phi(\rho, z)$ determination is to set $E_\phi(\rho = a, \phi, z) = 0$ for all $0 \leq \phi < 2\pi$, and all z along the length of the waveguide (pipe). The expression for electric field $E_\phi(\rho, \phi, z)$, available from solving the Maxwell's equations, is

$$E_\phi(\rho, \phi, z) = C_{mn}\left[\frac{dJ_m(k_\rho\rho)}{d(k_\rho\rho)}\right][C_2\cos(m\phi) + D_2\sin(m\phi)]e^{-jk_z z}, \qquad (12)$$

where C_{mn}, C_2 and D_2 are constants that depend on the specific characteristics of the electric dipole sources, and $J_m(k_\rho\rho)$ is the Bessel function of the first kind of order m. Also required is

$$k_\rho^2 + k_z^2 = k^2 = \omega^2\mu\epsilon - j\omega\mu\sigma. \qquad (13)$$

In this last equation, $\omega = 2\pi f$, where f is the frequency in Hertz, and μ, ϵ, and σ are, respectively, the magnetic permeability, electric permittivity and electrical conductivity of the medium (oil) filling the waveguide (pipe).

The requirement that $E_\phi(\rho = a, \phi, z) = 0$ is satisfied by

$$\left[\frac{dJ_m(k_\rho\rho)}{d(k_\rho\rho)}\right]_{\rho=a} = 0. \qquad (14)$$

For this to happen both k_ρ and a are real and positive. The function $\frac{dJ_m(k_\rho a)}{d(k_\rho a)}$ oscillates between positive and negative through the value zero an infinite number of times as $k_\rho a$ increases in value from zero. The integer n represents the number of these zero crossings, each n (zero crossing) representing a different type of TE^z mode. Notice that there are now two integers, m and n, associated with each type of TE^z mode. The abbreviation for each of these mode types is TE^z_{mn}. The value of $k_\rho a$ at the nth zero crossing of the function $\frac{dJ_m(k_\rho a)}{d(k_\rho a)}$ is given the symbol χ_{mn}. In other words, at the nth zero crossing,

$$k_\rho a = \chi_{mn}, \tag{15}$$

which gives

$$k_\rho = \frac{\chi_{mn}}{a}. \tag{16}$$

The attenuation of a TE^z_{mn} mode down the length of the waveguide in the z direction is determined by the terms $e^{-jk_z z}$ that appear in the expression for $E_\phi(\rho, \phi, z)$ (and the expressions for all of the other electric and magnetic field components associated with the mode). Thus, knowing the value of k_ρ for each m and n value one can compute the associated k_z value from the expression

$$k_z = \sqrt{k^2 - k_\rho^2} = \sqrt{\omega^2\mu\epsilon - j\omega\mu\sigma - \left(\frac{\chi_{mn}}{a}\right)^2}. \tag{17}$$

Although there are a couple of modes with less attenuation, the TE^z_{01} $(m = 0, n = 1)$ mode appears to be best for creating a maximum uniform magnetic field around the circumference of the waveguide wall. The $n = 1$ zero crossing for $\left[\frac{dJ_0(k_\rho a)}{d(k_\rho a)}\right]$ occurs for

$$\chi_{01} = 3.833, \text{which gives } k_\rho = \frac{3.833}{a}$$

This means that for the TE^z_{01} mode

$$k_z = \sqrt{\omega^2\mu\epsilon - j\omega\mu\sigma - \left(\frac{3.833}{a}\right)^2}. \tag{18}$$

The attenuation in the z direction is specifically expressed by the terms

$$\mathrm{Re}\left[e^{-jk_z z}\right] = e^{\mathrm{Im}[k_z]z}$$

where for the TE_{01}^{z} mode

$$\mathrm{Im}[k_z] = \mathrm{Im}\sqrt{\omega^2\mu\epsilon - j\omega\mu\sigma - \left(\frac{3.833}{a}\right)^2}. \quad (19)$$

As an example consider the following parameter values:

$f = 2 \times 10^6$ (2 MHz), $\omega = 2\pi f$, $\mu = \mu_0 = 4\pi \times 10^{-7}$, $\epsilon = \epsilon_0 = 10^{-9}/36\,\pi$,

$\sigma = 0.01\ S/m$, and $a = 9\ inches = 0.229$ m

For the TE_{01}^{z} mode these values give

$$\mathrm{Im}[k_z] = -16.99$$

Thus, the attenuation for this mode is described by the function $e^{-Im[k_z]\,z}$. (20)

Here, magnetic field is reduced by the factor 4.18x10^{-8} for every meter in the z direction. The frequency of a waveguide mode must be above the cutoff frequency in order to propagate without severe attenuation. The cut-off frequency ω_c, for a TE_{mn}^{z} mode may be computed from the expression

$$\omega_c = \frac{\chi_{mn}}{a\sqrt{\mu\epsilon}}. \quad (21)$$

Expressed in Hz, the cutoff frequency is

$$f_c = \frac{\chi_{mn}}{2\pi a\sqrt{\mu\epsilon}}. \quad (22)$$

For the TE_{01}^{z} mode the value of the cutoff frequency is 800.6 MHz. Any mode whose frequency is below cutoff is said to be evanescent and is severely attenuated.

TM^z Modes

A discussion of the TM^z modes parallels that of the TE^z Modes. For the TM^z modes the boundary conditions require that z-component of the electric field, $E_z(\rho = a, \phi, z) = 0$. The expression for $E_z(\rho, \phi, z)$ associated with TM^z modes is

$$E_z(\rho, \phi, z) = -jB_{mn}\frac{k_\rho^2}{\omega\mu\epsilon}J_m(k_\rho a)[C_2\cos(m\phi) + D_2\sin(m\phi)]e^{-jk_z z}. \quad (23)$$

The boundary requirement is satisfied by

$$J_m(k_\rho a) = 0. \quad (24)$$

The function $J_m(k_\rho a)$ oscillates both positive and negative through the value zero. As with the TE^z modes the integer n numbers the successive zero crossings. This means that there is both an m and an n associated with each TM^z mode, abbreviated TM_{mn}^z. The value of $k_\rho a$ for each crossing is expressed by

$$k_\rho a = \chi_{mn}, \quad (25)$$

which gives

$$k_\rho = \frac{\chi_{mn}}{a}. \quad (26)$$

The values of χ_{mn} for the TM_{mn}^z modes have also been tabulated for different values of m and n. To find the mode attenuation the procedure follows that described for the TE_{mn}^z modes. The expression for k_z is

$$k_z = \sqrt{k^2 - k_\rho^2} = \sqrt{\omega^2\mu\epsilon - j\omega\mu\sigma - \left(\frac{\chi_{mn}}{a}\right)^2}, \quad (27)$$

and the specific term that express the attenuation in the z direction are $\mathrm{Re}\left[e^{-jk_z z}\right] = e^{\mathrm{Im}[k_z]z}$.

It appears that the TM_{mn}^z mode best suited to produce a uniform magnetic field at the waveguide wall is TM_{01}^z $(m = 0, n = 1)$. For this mode,

$$\chi_{01} = 2.405 \text{ which gives } k_\rho = \frac{2.405}{a}.$$

With the same example parameters used with the TE_{01}^{z} mode, the exponential term describing the mode attenuation in the z direction is

$$e^{\mathrm{Im}[k_z]z} = e^{-10.52z}. \tag{28}$$

The field components are reduced by the factor $2.7\text{x}10^{-5}$ for each meter along the z axis. The Hertz cutoff frequency for the TM_{01}^{z} mode is 502.3 MHz. Modes with frequency less than this are evanescent and severely attenuated.

Next, we used the equations described above to evaluate the attenuation of magnetic waves inside a pipeline containing fluids of different electrical conductivity. Waveguide attenuation is more pronounced at higher electrical conductivities, which happens when fluids contain high water and salt content. Hence it is instructive to quantify this effect using equation (19) and equation (20). The attenuation factor was calculated at 500 MHz and different magnetic fields by varying the electrical conductivity in equation (19). Equation (20) was used to calculate the attenuation at different distances along the pipe (z). These equations were solved in MATLAB and the results are shown in Figure 37. It shows that for lower conductive fluids, electromagnetic waves can propagate without severe attenuation of magnetic field amplitude and at higher conductivities, the attenuation is steep. For instance, at an electrical conductivity of 0.01 mho m^{-1}, the wave attenuates within 1 m of propagation, whereas at 1E-5 mho m^{-1}, the wave propagates about 20 m with minimum attenuation.

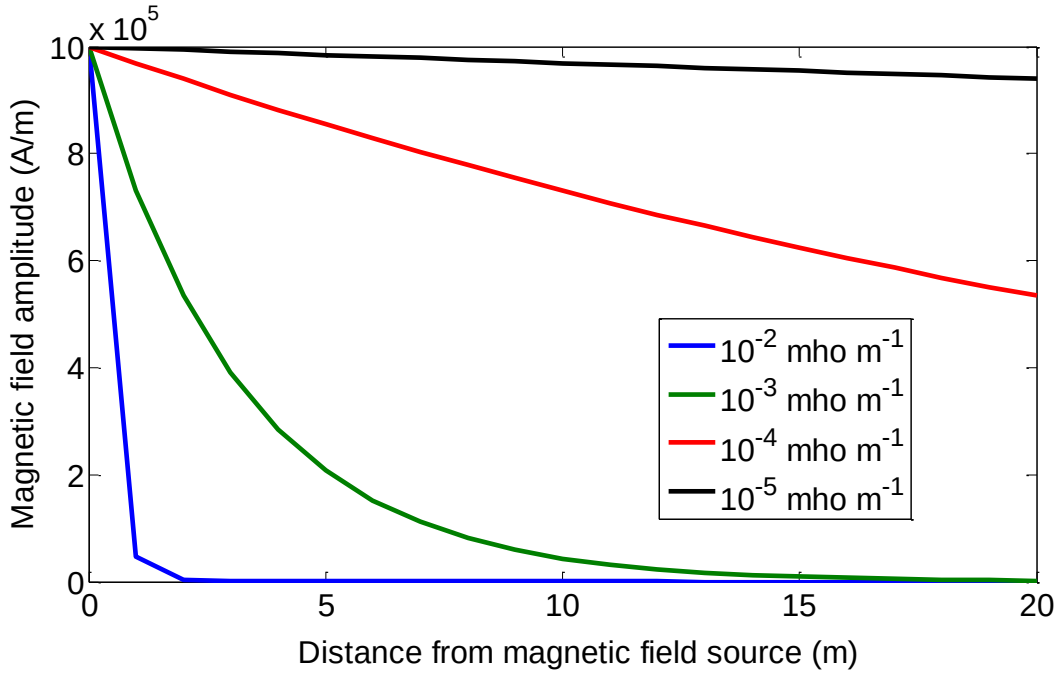

Figure 37: Electromagnetic wave attenuation in a steel pipeline containing fluids of different electrical conductivities at 1 GHz

However, cut-off frequencies as high as 500 MHz (used in this calculation) would be difficult to generate in terms of technology and cost. Further, pipelines extend for several kilometers and hence a single waveguide would not be able to service an entire system of pipelines. Waveguide can be considered to be a 'far field' source of excitation, since its location is fixed and fields propagate from this location to far distances. For our application, 'near field' sources of magnetic field would be critical to deliver sufficient energy. In the case of near fields, we consider the magnetic field close to the source of excitation. In the vicinity of the sources the 'near fields' would fall off less rapidly than shown for the modes. This might mean that a properly designed spatial sequence of sources could produce enough magnetic field at the pipe wall to cause the nanoparticle

paint to significantly heat the medium in the pipe. Consequently, a magnetic field source that moves along the pipe can generate a strong magnetic field along it, eliminating the concern of attenuation. Hence, next we study the effect of 'near field' source of magnetic field on nanopaint, namely a concentric multi-turn coil or solenoid inside a pipeline.

5.1.3. Theory: Magnetic Field between a Pipe Wall and Concentric Coil

Figure 38 shows the magnetic field lines produced by a multi-turn, cylindrical, current-carrying coil positioned inside a cylindrical pipe. The figure shows a cross sectional view of the concentric coil and the pipe. The purpose of showing the figure is to illustrate how the magnetic field could be made stronger outside the coil in the space between the pipe and the coil windings than it is inside the coil, so that the magnetic energy delivery to the nanopaint can be effective.

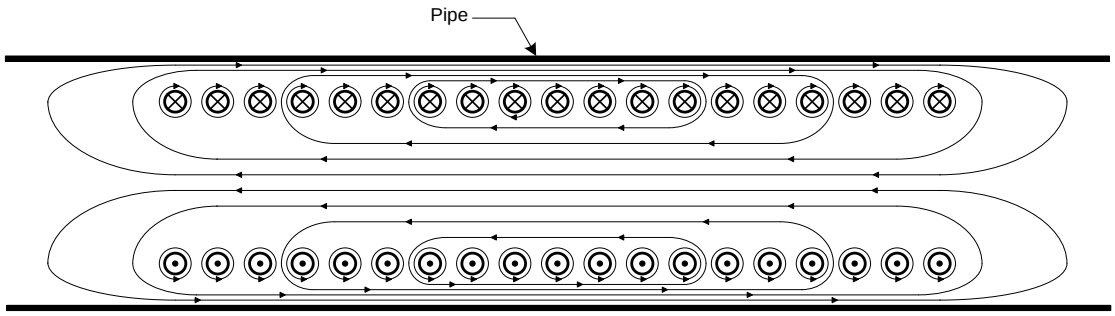

Figure 38: Magnetic field line distribution by a cylindrical concentric multi-turn coil inside a cylindrical steel pipeline

In the figure, the current in the coil windings shown at top is flowing out of the page and that in the lower windings is flowing into the page. It is assumed that each winding carries an equal amount of current. The magnetic field is represented by lines that encircle the coil windings. The direction of the magnetic field is indicated by

arrowheads attached to the field lines. Some of the lines encircle the wire of a single turn of the coil while others encircle groups consisting of any number of turns.

As shown in Figure 38, all of the field lines that pass from right to left through the inside of the coil must return passing through the outside of the coil wires. If the pipe is made of metal and the magnetic field is excited by alternating currents in the coil windings, then the penetration of the magnetic field into the pipe wall will be quite small due to the skin depth limitation (charge tends to concentrate on pipe wall) (Reutov & Loskutov 2007). This means that essentially all of the magnetic field flux inside the coil passes through the space between the coil windings and the pipe wall. The radial dimension of this space can be set by adjusting the radius of the coil relative to that of the pipe. Here, the radius of the coil is a significant fraction of that of the pipe, in order for the nanopaint on the pipe wall to experience the intense magnetic field. As described below, for our application we envision to use a coil encased in a free floating magnetic field generator, for which the relative radius of the coil to the pipe will be a design parameter.

It is true that there will be some ohmic heating due to the induced currents in the pipe. This will simply add to heat produced by the nanopaint layer. Nonetheless as much magnetic energy should be delivered to the nanopaint layer, so that the maximum heating efficiency by the nanoparticles in the layer could be achieved by Neel relaxation.

Based on the above preliminary design considerations, we propose a magnetic wave delivery system consisting of a hydraulically balanced, buoyant, portable, multi-turn coil generator that moves along the length of the pipeline. The schematic of the setup is shown in Figure 39.

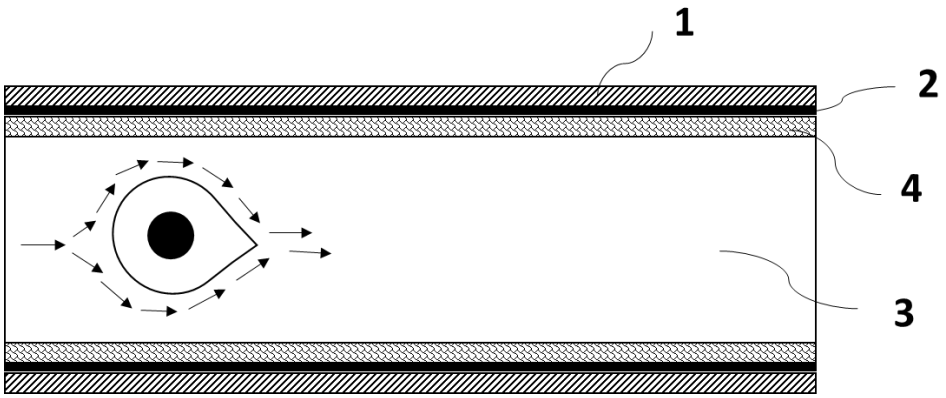

Figure 39: A hydraulically balanced, buoyant magnetic field generator device that streamlines the flow of oil inside the pipeline (1) which is coated with nanopaint (2). The pipeline carries crude oil (3) and wax deposits (4)

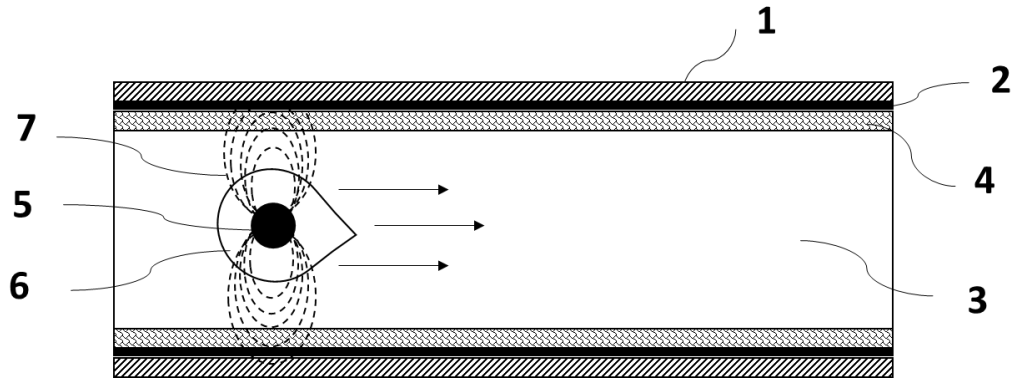

Figure 40: A hydraulically balanced, magnetic field generator device with generator (5) and external casing (6) generates an alternating magnetic field (7). The nanopaint subjected to an alternating magnetic field heats up, heating a thin layer of wax next to it

When turned on, the magnetic field generator generates an alternating magnetic field, as shown in Figure 40. This field heats up the nanopaint, which in turn heats a thin layer of wax. As the wax heats up to its melting point ~ 323 K, it detaches itself from the

pipeline surface and enters the fluid phase, most probably in small pieces, as shown in Figure 41.

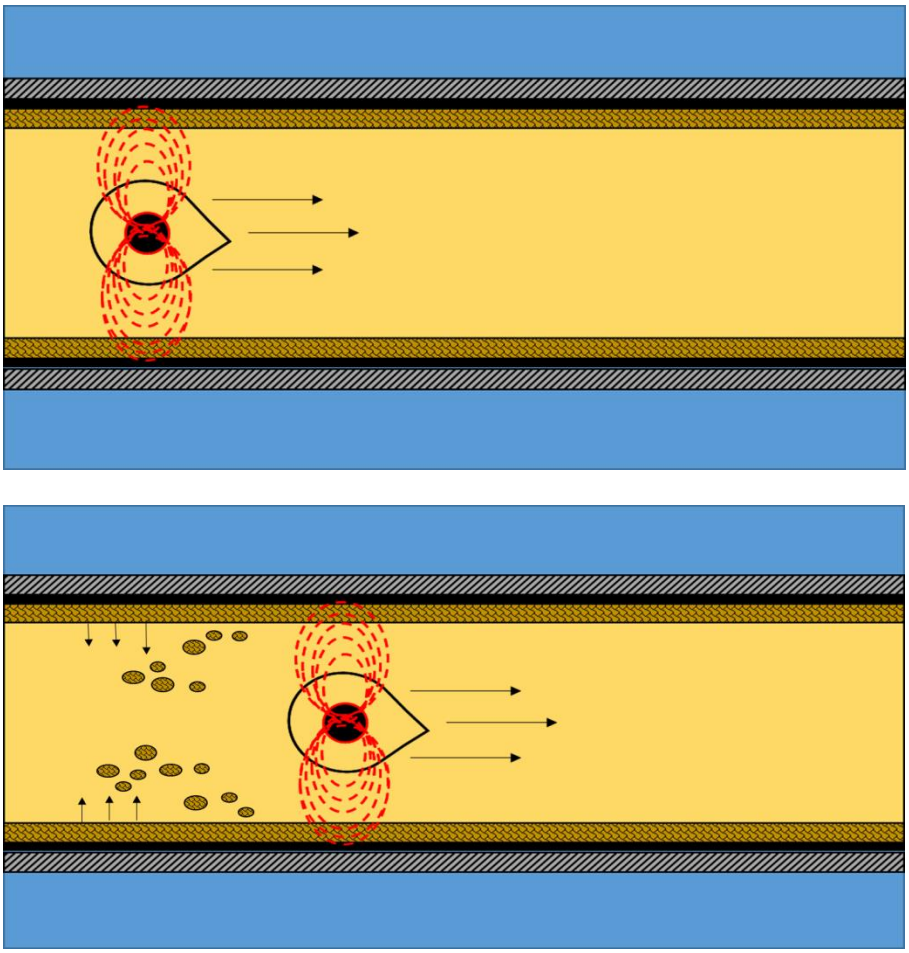

Figure 41: Alternating magnetic field heats the nanopaint which results in subsequent melting and removal of wax deposits over time

The heating rate of the wax will depend on the magnetic field and concentration of nanoparticles in the nanopaint. This will also determine the residence time and velocity of the magnetic field generator moving along the pipe axis inside the pipeline. These

topics will be discussed in the next section, by carrying out the simulations of magnetic field propagation and heat transfer within a model pipeline system.

5.2 Computational Modeling of Nanopaint-induced Heating of Wax Deposits in a Subsea Pipeline

This section will discuss the computational modeling work using COMSOL v.4.3a, a finite element modeling software package. It is used to model magnetic energy delivery to a nanopainted steel pipeline and analyze the subsequent change in temperature distribution across a subsea pipeline. We also create a model for the wax coupon heating setup described in Chapter 4 and validate it with experimental results.

The models help us understand the key implementation issues: a) the magnetic field distribution inside a nanopainted steel pipeline due to an alternating current-carrying multi-turn coil, b) heat flow and temperature distribution in a subsea pipeline due to nanopaint heating and c) energy and material requirement to remove wax deposit and maintain flow conditions in a subsea pipeline.

The procedure for generating a model in COMSOL, for both the magnetic field generation and heat transport, follows the steps below:

1) Input of model parameters and definitions
2) Build model geometry
3) Assign appropriate boundary and domain conditions
4) Mesh model geometry
5) Solve appropriate partial differential equations via finite elemental analysis
6) Analyze and process results

The key model inputs, equations, and boundary conditions will be described for the model, followed by optimization study and analysis of results.

5.2.1 Pipeline Model Description

We model the subsea pipeline as a pipe in pipe cylindrical system, separated by insulation as shown in Figure 42.

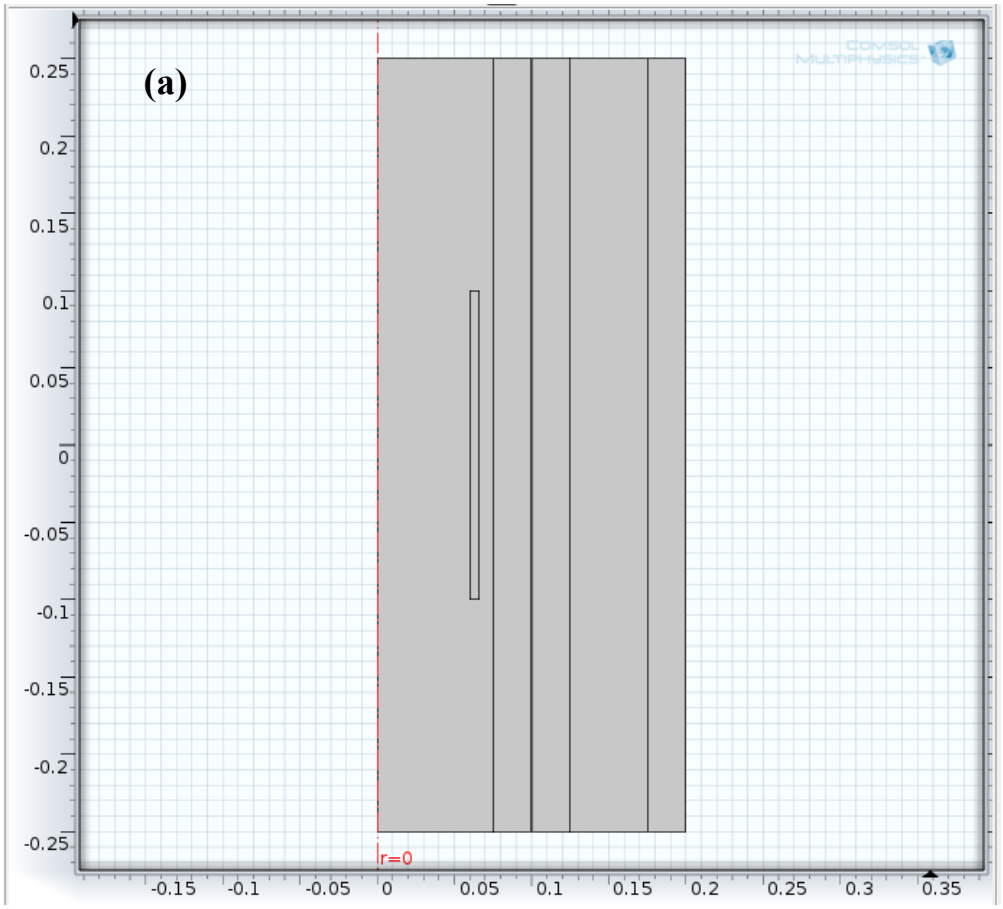

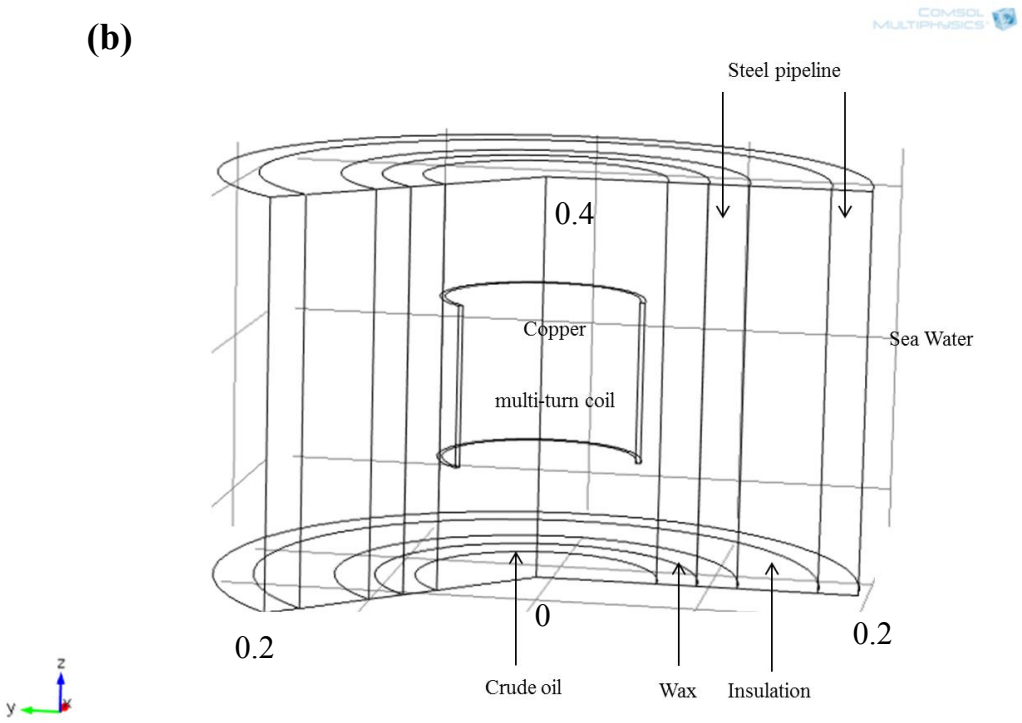

Figure 42: Model of the subsea pipe-in-pipe system containing a multi-turn coil in (a) 2D view, and (b) 3D view

The pipe-in-pipe system provides safety and insulation to the pipeline fluids. The inner pipeline carries the crude oil, while the outer pipeline is subjected to the harsh sea environment. However, for the COMSOL model, calculations were performed for a single section of the pipe. Hence, a stationary fluid at steady state was assumed. The pipeline carries a magnetic field generator, which is modeled as a multi-turn copper coil, in line with the current market specifications. COMSOL defines multi-turn coil by constructing a solid region and dividing it into several turns. Hence, the coil is modeled as a single layer. An induction heating module is applied to the model on COMSOL, which automatically applied magnetic field boundary conditions on different surfaces

based on their magnetic properties. As mentioned earlier, the geometry of the system is cylindrical with layers of insulation, pipeline, wax and oil, with specific inner diameter and outer diameter. The specification of the pipe-in-pipe model, based on typical field values (Varon et al. 2012) is shown in Table 9. The material properties employed for the model are shown in Table 10. The in-built material properties of COMSOL were used.

Component	Parameter	Abbreviation	Unit	Value
Inner steel pipeline	Inner diameter	D_1	m	0.2
	Outer diameter	D_2	m	0.25
Outer steel pipeline	Inner diameter	D_3	m	0.35
	Outer diameter	D_4	m	0.4
Insulation	Thickness	t	m	0.05
Wax	Thickness	t	m	0.025
Coil	Inner diameter	D_0	m	0.12
	Thickness	t	m	6.25E-03
	Number of turns	N	-	25
	Length	L	m	0.2
	Resistance	R	Ω	1.12E-04
Nanopaint	Thickness	t	m	2.00E-04

Table 9: Specifications of the pipe-in-pipe model

Material properties	Symbol	Unit	Copper	Steel	Insulation	Wax
Relative permeability	μ_r	-	1	1	N/A	2.1
Relative permittivity	ϵ_r	-	1	1	N/A	2.1
Electrical conductivity	σ	S/m	6.0E+7	4.03E+6	2.50E-8	1.0E-8
Heat capacity	C_p	J/Kg.K	385	475	2000	3430
Density	ρ	Kg/m^3	8700	7850	750	900
Thermal conductivity	k	W/m.K	400	44.5	0.17	0.25

Table 10: Material properties of the pipe-in-pipe model

We model a transient state induction heating behavior of the above model system. The schematic of boundary conditions is shown in Figure 43.

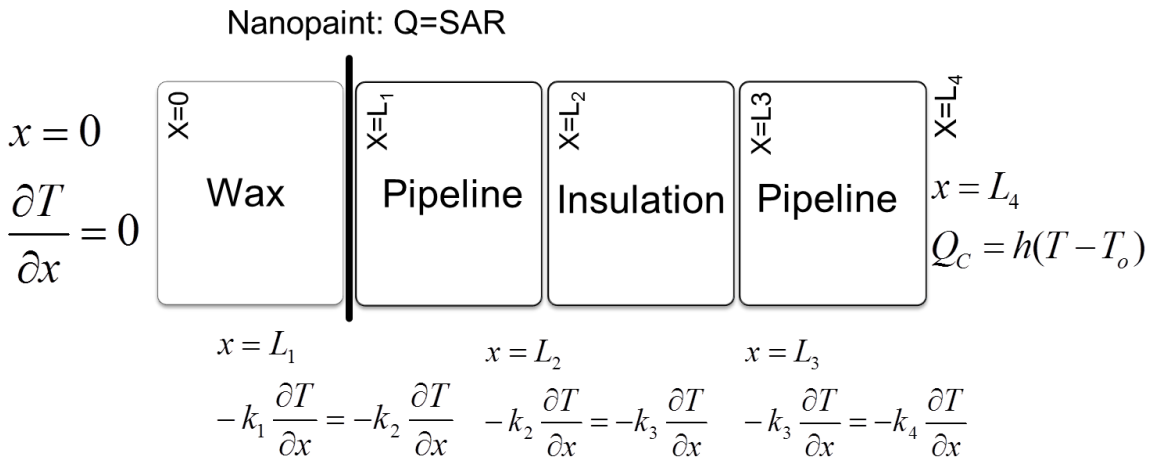

Figure 43: Schematic of boundary conditions of pipe-in-pipe system COMSOL model

Initially, the entire system is at 25°C. The layers are coupled by the boundary condition of heat flux continuity, and with a heat source and a heat sink. The transient-state equation for heat conduction is given by equation (29).

$$\rho C \frac{\partial T}{\partial t} = \nabla.(k \nabla T) \tag{29}$$

where ρ, C, and k are the density (Kg/m^3), specific heat capacity (J/Kg.K) and thermal conductivity (W/m.K) of the system respectively. $\frac{\partial T}{\partial t}$ is the temperature gradient with respect to time, and ∇T is the spatial variation in temperature (x, y or z direction)

The condition of constant heat flux between two surfaces a and b is given by

$$k_a \frac{\partial T}{\partial x} = k_b \frac{\partial T}{\partial x} \tag{30}$$

As schematically shown in Figure 42, we assume that the bulk of the wax acts as an insulator, for the short duration until it detaches by surface melting and hence there is no heat flux at the surface, as given by equation (31).

$$\frac{\partial T}{\partial x} = 0 \tag{31}$$

The sea water surrounding the outer pipeline at 5°C is a heat sink. It cools the pipeline by convection, given by equation (32), where h is the overall heat transfer coefficient, set as 2000 W/m^{2}K for the present simulation (Varon et al. 2012), T_0 is the external ambient temperature, and T is the temperature of the pipeline fluid.

$$Q_c = h(T - T_0) \tag{32}$$

Nanopaint is modeled as a heat source on the boundary between the wax and inner pipe. It generates heat as a function of magnetic field and nanoparticle loading. The heat produced in W/m^2 is given by SAR definition, as in equation (5). The value of constants is applied to the equation (see section 2.5, Table 1) at 500 kHz and heat generation was normalized per unit area, given by equation (33).

$$Q = 125 \times 10^{-6} l_{NP} (H)^2 \tag{33}$$

where l_{NP} is the nanoparticle loading in paint in g/m^2 and H is the normal component of magnetic field in A/m.

5.2.2 Parameters for Design and Analysis

A thin section of the model created by COMSOL is shown in Figure 44. The model is solved for various iterations of nanoparticle loading, $l_{NP,}$ and coil current, I, which directly changes the magnetic field H. The coil current is varied over 10 data points from 50 A to 400 A and nanoparticle loading is varied from 10 g/m^2 to 100 g/m^2. In comparison, for our experiments, the nanoparticle loading was varied between 4 g/m^2 (2 % by weight of Fe_3O_4 nanoparticles) and 34 g/m^2 (14 % by weight of Fe_3O_4 nanoparticles). Coil current and nanoparticle loading directly affect heat generation from nanopaint. The frequency of the magnetic field is maintained constant at 500 kHz.

The primary measurement parameter is temperature at the wax-nanopaint surface due to heating of nanopaint by magnetic field. This is evaluated by defining a surface temperature probe. For each case, the time that is required for the nanopaint – wax interface to reach 323 K (melting point of wax) is evaluated. This time will be the minimum residence time of the magnetic field generator to provide the required magnetic field to the pipe section, and can thus be used for calculating velocity of the device passing over the particular pipe section. This data was used to calculate the cost and power requirement for the device to heat and melt wax from a certain length of the pipeline. Further, for every analysis, a 2D and a 3D plot of magnetic field distribution is generated. For a given nanopaint-wax system, maximizing magnetic field at the nanopaint location will optimize heating. This can be done by adjusting the location or radius of the coil as discussed in the preceding section. Finally, the nanopaint heating model is compared to the base case of induction heating of steel only. This comparison

shows the effect of ohmic heating and hence the relative contribution of nanopaint towards heating.

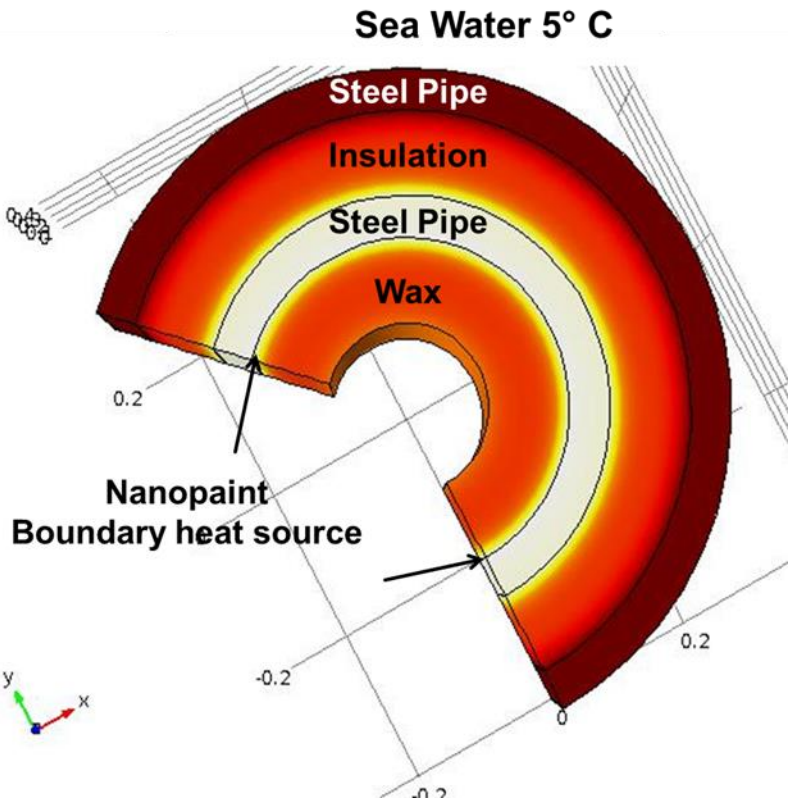

Figure 44: 2D COMSOL model of pipe-in-pipe system

As discussed earlier, the main design parameter for a given nanopaint-wax system is the strength of the magnetic field. Magnetic field distribution is not uniform and is highly dependent on the designs and location of the coil. In our application, the magnetic field outside the coil is desired to be at a maximum for a given coil current. This can be achieved by modifying the shape of the coil, the number of turns and its relative position to the nanopaint surface. Due to the limited processing capability of the available COMSOL version, the shape of the coil cannot be varied. However, the coil's relative

radius to the pipe is a variable parameter. It is observed that closer proximity of coil to the nanopaint surface results in a stronger magnetic field on the surface. Hence the coil should be as placed as close to the surface as practicably possible.

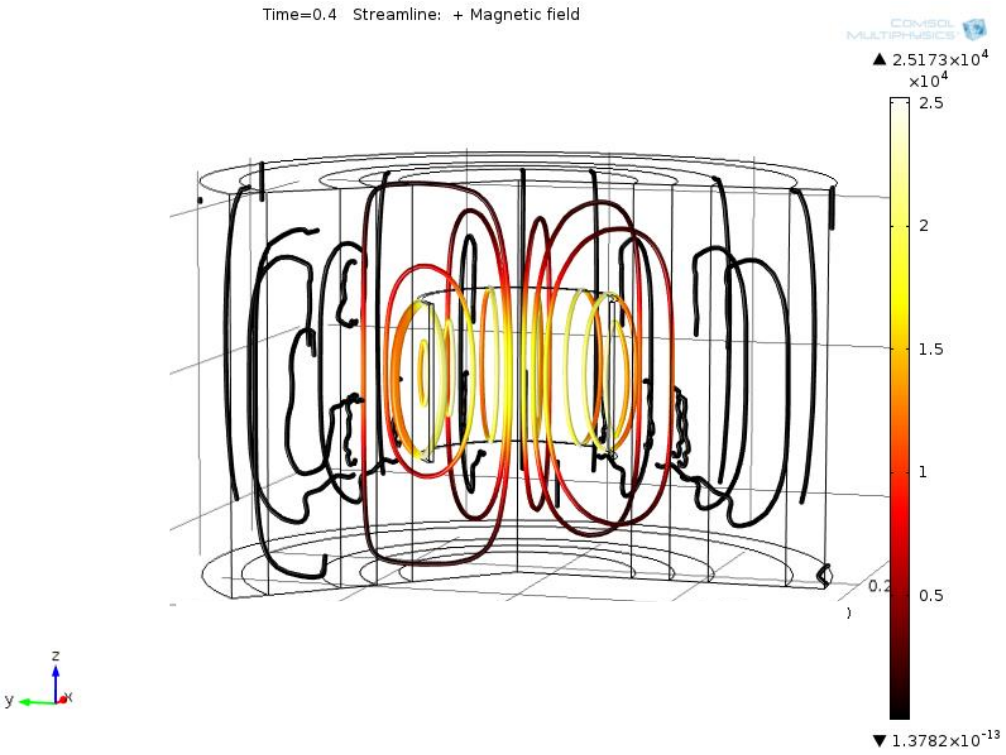

Figure 45: 3D plot of magnetic field lines inside the pipe at coil current of 300 A and magnetic field frequency of 500 kHz

An example of a 3D magnetic field plot at 300 A and 500 kHz is shown in Figure 45. This shows the magnetic field intensity, shown in different colors of the magnetic flux lines, in and around the multi-turn coil inside a pipeline. The color bar on the right indicates the intensity, with white representing the strongest and black representing the

weakest magnetic field, in A/m. As seen in the figure, the magnetic field intensity is the strongest at the center of the coil and diminishes away from the coil, radially and longitudinally. When magnetic field lines contact the steel surface, they attenuate due to concentration of electric charges on the surface. This result can be seen more clearly in the 2D plot shown in Figure 46.

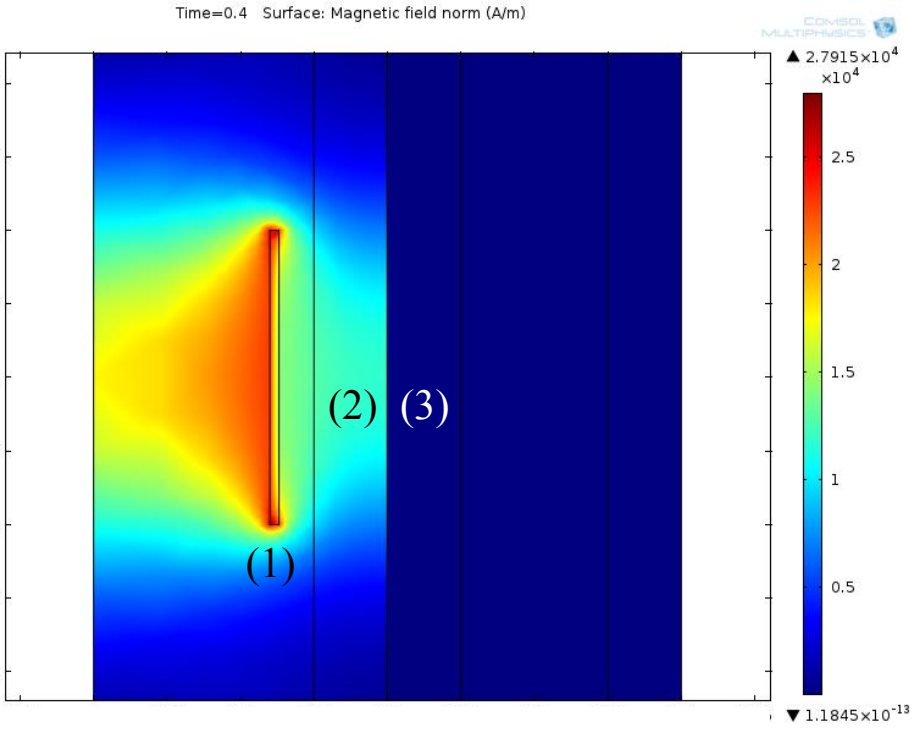

Figure 46: 2D plot of magnetic field distribution inside the pipeline system at coil current of 300 A and magnetic field frequency of 500 kHz with (1) a multi-turn coil, (2) wax, and (3) pipeline

The magnetic field excites the nanopaint and produces heat. This heat is distributed through the pipe-in-pipe system. The time taken for the nanopaint-wax layer

to reach 323 K (melting point of wax) is recorded. All such results are recorded and are shown in the next section.

5.2.3 Model Results

The maximum magnetic field at the mid-point of the coil, on the nanopaint surface, corresponding to different coil currents is summarized in Table 11. The time taken to melt wax for different coil currents and nanoparticle loading is shown in Figure 47. This corresponds to the minimum residence time, which is the time required for the magnetic field generator to heat nanopaint surface to desired wax melting temperature. The figure indicates a power relation of coil current with heating. We compared nanopaint heating to the case of induction heating by steel only and found that it takes 10 times more time than the 10 g/m^2 case. This shows that the conventional induction heating is negligible compared to nanopaint heating.

Coil Current I (A)	**Maximum Magnetic Field on Nanopaint Surface H (A/m)**
100	3920
200	7840
300	11760
400	15000

Table 11: Maximum magnetic field on nanopaint surface (A/m) corresponding to coil current 100 A, 200 A, 300 A, and 400 A

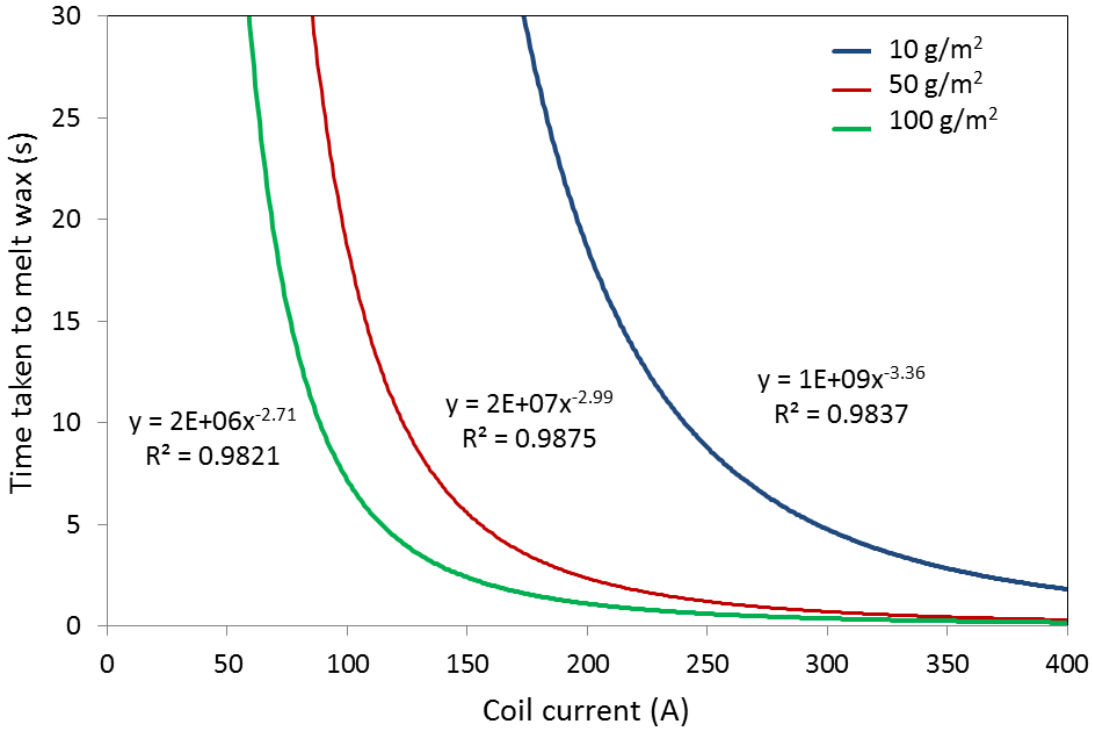

Figure 47: COMSOL Results - Time taken to melt wax from the defined subsea pipe by different coil currents from 100 A to 400 A and nanoparticle loading of 10, 50 and 100 g/m^2

The effect of nanoparticle (in nanopaint) loading on heating was also found to have a power dependence on time. Figure 48 shows that increasing nanoparticle concentration greatly would not increase heating proportionately. This relation can be used to optimize the heating performance. For instance, changing nanoparticle loading from 10 to 50 g/m^2 decreases the residence time from 2 s to 0.4 s at 400 A or 15000 A/m. A further increase in nanoparticle loading, above 50 g/m^2, changes the residence time to 0.25 s, which is not a substantial increase.

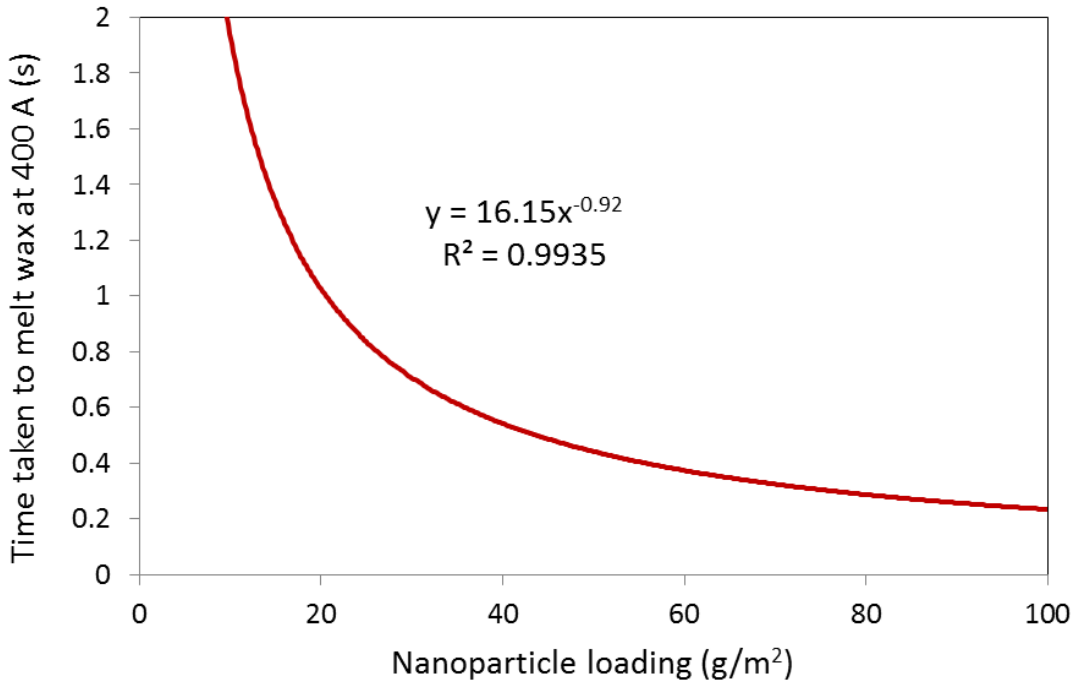

Figure 48: COMSOL Results - Time taken to melt wax at 400 A at different nanoparticle loadings from 10 g/m^2 to 100 g/m^2

These results were further analyzed to estimate the cost of implementation of nanopaint-induced heating. The power consumed per km of pipeline (Wh/km) was calculated for each case using the equation (34).

$$P = \frac{1000I^2Rt}{L} \tag{34}$$

where I is the coil current (A), R is the resistance of the copper coil (Ω), t is the time (s) taken to heat a section of length L (m). Using Figures 47 and 48, the time taken for various currents and nanoparticle loading can be found. Thus, the power consumed was calculated and plotted, as shown in Figure 49. This plot can be used to choose an optimum current and nanoparticle loading based on the battery power available.

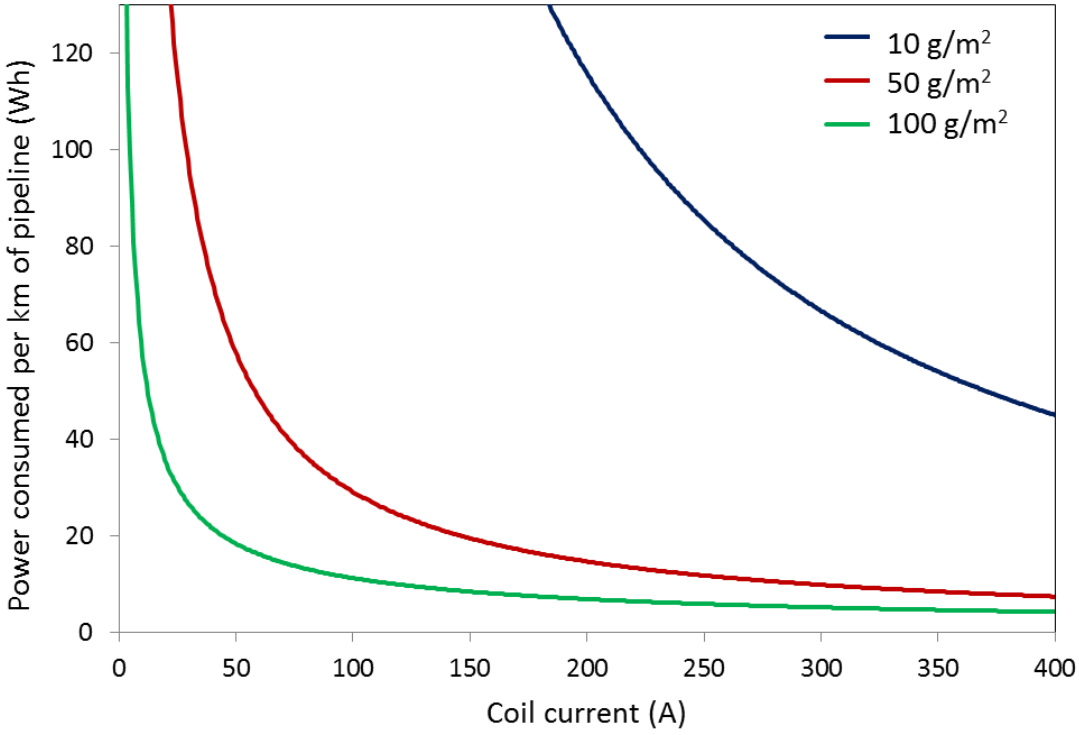

Figure 49: COMSOL Results - Power consumed by nanopaint for different coil currents and nanoparticle loading

Next, we evaluated the power delivery of a standard Lithium-ion battery with a specification: 12 cell battery, 3300 mAh and maximum current of 430 A, weighing about 2 Kg. The cost of such a battery is currently about $100. These specifications can be used to calculate the power that can be supplied by the battery, using equation (35).

$$P_{battery} = \frac{M \times N_C \times V_s}{1000} \tag{35}$$

Where M is the total amount of energy a battery can hold at a given time (mAh), N_c is the total number of cells in a battery, and V_s is the voltage of a standard cell which is 3.7 V for a standard Li-ion cell. Using this equation, the power of the battery was calculated to be 147 Wh.

Based on the power requirements shown in Figure 49, we calculated the length of pipeline that one such battery of 147 Wh would be able to heat up before replacement and the results are shown in Figure 50.

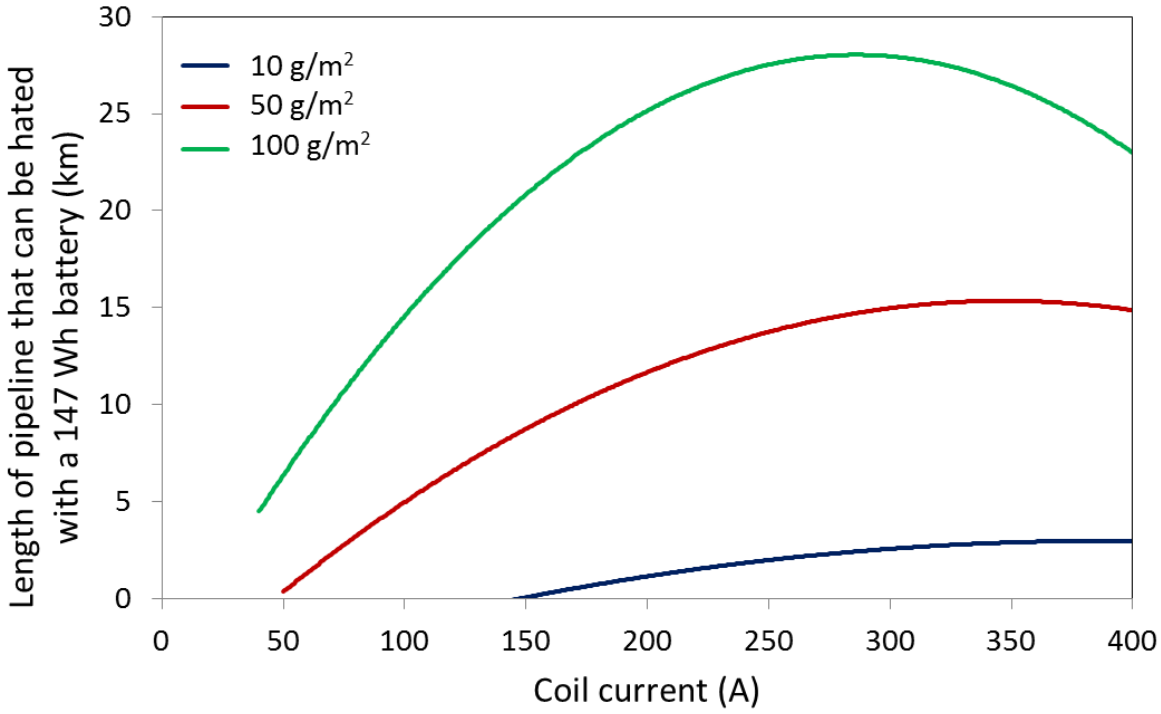

Figure 50: Length of pipeline that can be heated with a 147 Wh battery at different coil currents

This figure shows that as the coil current increases, a greater length of pipeline can be traversed to melt the wax. This is due to the lower residence time required and hence higher velocity of the magnetic field generator moving along the pipeline. However, the increase is not linear as indicated by the exponential relation of heating time with coil current/magnetic field. Hence, this plot can be used to choose an optimum configuration that can achieve melting of wax from a pipeline. For instance, with the

simple battery described above, maximum pipeline length of 27 km can be heated with a coil current of about 300 A, which corresponds to a magnetic field of 12000 A/m at 100 g/m^2 of nanoparticle loading. At 12000 A/m and 50 g/m^2 of loading, a pipeline length of 15 Km can be traversed to melt the wax with a 147 Wh battery. Given, the cost of generating magnetic field (coil current), the cost of installation and launching of magnetic field generator, and the nanoparticle cost, an optimized choice can be made.

Next, these results were compared with the case of the conventional induction heating only. In case of induction or eddy current heating (no-nanopaint), the battery would be able to heat up and melt wax from about 0.5 Km of pipeline. This shows that power consumption is very high for the case of induction heating of steel and hence is not economical. Further, it would not be practical to design a system with small enough velocity to deliver sufficient duration of magnetic field to the steel pipeline. Hence, magnetic nanopaint-based heating is a better method for wax removal.

Chapter 6: Conclusion

6.1 Experimental Conclusions

In this thesis, heating by superparamagnetic Fe_3O_4 nanoparticles was empirically evaluated for two samples varying in size distribution; at magnetic fields ranging from 200 – 1000 A/m; and frequencies of 450 kHz and 630 kHz. Experiments were performed by varying the following parameters: medium of nanoparticles (liquid dispersions, solid paint), state of heated fluid (batch or flow), and concentration of nanoparticles, magnetic field strength and frequency. The properties of nanoparticles and nanopaint were quantitatively determined and related to heating performance. Based on heating performance results and theoretical predictions, the following conclusions were drawn.

- Nanoparticle behavior in dispersion and in paint was found to be superparamagnetic, as measured by VSM. Even though EMG 605 is hydrophilic it does not agglomerate in organic solvent-based paint, but simply embeds in paint and shows the same heating performance as dispersions. The distribution of nanoparticles in nanopaint was found to be non-uniform, judging from the lower susceptibility value of nanopaint compared to dispersions, as measured by VSM. The thickness of the paint was found to be variable between 90 to 300 μm.
- Heating performance of nanoparticles in liquid dispersions and nanopaint were comparable. This shows that nanoparticle-based heating by Neel relaxation was not constrained by the type of medium (liquid, solid), if the thermal property was maintained constant. Hence, Neel's relaxation theory for superparamagnetic nanoparticles (SPM-NPs) in fluid can also be applied to nanopaint.
- Heating performance of magnetic nanoparticles was independent of concentration of particles but strongly dependent on particle size distribution, for a given magnetic field and frequency. Based on size distribution obtained by TEM, it was

predicted and experimentally verified that EMG 605 shows better heating performance than EMG 1400. EMG 605 showed a maximum SAR of 95 W/g at about 575 A/m. Experimental data shows that only SAR of EMG 605 shows quadratic dependence on magnetic field, in line with Neel's relaxation theory. For EMG 605, SAR was proportional to 1.3E-3 $H^{1.76}$ and this correlation can be used to predict SAR for different magnetic fields. Hence, EMG 605 nanoparticles and nanopaint, was used for all subsequent experiments. The results were insufficient to explain deviation of EMG 1400 from this quadratic behavior. Several samples varying in size distribution need to be evaluated to understand the effect of size distribution on heating performance.

- Heating performance for flow experiments is better than batch experiments by a factor of ~ 5 to 8. Flow-induced mixing and an increased temperature gradient between nanopaint and flowing fluid result in better heat transfer, hence higher SAR of flow experiments. In view of the strong dependence of SAR on temperature, an efficient dissipation of the generated heat from the nanoparticles is important to maintain a high SAR.
- Heating performance of nanopaint decreases with increase in temperature. Heating rate of nanopaint under low ambient temperatures of 10 °C to 20 °C was found to be marginally higher than the heating rate at higher temperatures. Over a broad temperature range, the effect of higher heating rates at lower temperatures is cancelled by the lower heating rates at higher temperatures. Hence, for the purpose of our application in subsea pipelines, the experimental correlation obtained for EMG 605 at ambient room temperature may be applied.
- Heating performance of nanopaint was found to be the same for different systems, namely decane and water. The heat produced and hence SAR was found to be the

same, for a given magnetic field and is given by the correlation of SAR proportional to 1.3E-3 $H^{1.76}$. Hence, SAR is a constant value for different systems under the same conditions.

- The feasibility to melt wax deposits by nanopaint was proved by the wax coupon experiments. It was found that the heating rate of melting wax did not depend on the thickness of the deposit. Surface heating involves melting a thin layer of wax in contact with the nanopaint and does not depend on the mass of the sample heated.
- Spin coater was used to develop uniform coatings on test coupons for nanopaint heating experiments. Several types of epoxies and block co-polymer were used as the medium. Trials were performed on different materials of coupons such as polystyrene, polycarbonate and polypropylene sheets. Best coating was obtained using Macropoxy 646 A and B, from Sherwin Williams with EMG 605 iron oxide nanofluid, on a polycarbonate sheet. The coating was uniform at about 10 to 14 μm. While this method was good to prepare nanopaint test coupons, it was difficult to coat cylindrical surfaces; and consequently manual method of coating was used to coat the test pipe's inner surface.

6.2 MODELING CONCLUSIONS

- Models of magnetic field excitation of nanopaint in a subsea steel pipeline were developed using COMSOL. This was used to simulate a scenario where nanopaint heating is used to melt and remove the wax deposited on the pipeline. The model consisted of a pipe-in-pipe system made of steel, coated with nanopaint and containing crude oil. A multi-turn coil was modeled in the center of the pipeline, to generate an alternating magnetic field. This model showed the magnetic field distribution obtainable by varying current in the multi-turn coil, and the subsequent heating produced by nanopaint excitation at various magnetic fields.
- The time taken to melt wax at different coil currents was evaluated. It was found that the time taken to melt wax followed a power relation with the coil current variation from 100 to 400 A. This current variation corresponded to a maximum magnetic field of 3900 A/m to 15000 A/m on the nanopaint surface. Residence time as low as 0.25 s at 15000 A/m was obtained.
- Time taken to melt wax showed a power correlation with nanoparticle loading from 10 g/m^2 to 100 g/m^2. This shows that the heat generation at the nanopaint locally, is constrained by its dissipation to the surroundings. The time required to melt wax vs. nanoparticle loading was plotted and could be used for optimization of heat delivery design. It was found that changing nanoparticle loading from 10 g/m^2 to 50 g/m^2 decreases the residence time from 2 s to 0.4 s. A further increase in nanoparticle loading over 50 g/m^2 does not change the residence time substantially.
- The power consumed per Km of pipeline at a given magnetic field was calculated. Based on the power consumed, the length of the pipeline that can be traversed using a 147 Wh battery was calculated, as an example design. It was found that a

maximum pipeline length of 27 Km can be heated with a field of about 12000 A/m at 100 g/m^2 of nanoparticle loading. At 12000 A/m and 50 g/m^2 of loading, a pipeline length of 15 Km can be traversed to melt the wax with a 147 Wh battery. Given the cost of generating magnetic field (coil current), the cost of installation and launching of magnetic field generator, and the nanoparticle cost; the dimensions of the coil relative to the pipe dimension, the velocity of the coil (magnetic field generator), the nanoparticle loading on nanopaint, etc. can be optimized, employing the SAR correlation developed and taking the modeling approach taken in this thesis.

6.3 FUTURE WORK

- Experimental SAR values for static experiments are higher than those predicted by Neel's relaxation theory, for a given magnetic field. Comparison with literature values for similar size nanoparticles and experimental parameters suggests that the specification of magnetic field for our magnetic field generator was not accurate. Accurate measurement of magnetic field is needed for effective comparison.
- Heating experiments can be conducted at different frequencies in the kHz and MHz range for the same coil configuration. Heating performance can be optimized in terms of frequency of magnetic field. This parameter could not be studied due to the limitations of the magnetic field generation equipment.
- Nanoparticle samples of asymmetrical shapes may be used for experiments. It has been observed in literature that several needle-shaped, and ellipsoid nanoparticles are capable of producing more heat due to higher anisotropy. This can be utilized to optimize heating performance.
- An experimental setup of a solenoid inside a steel tube can be built to test the effect of magnetic field inside a metal. The tube can be coated with nanopaint and subjected to an alternating magnetic field. The heating produced by nanopaint can be compared to the eddy current heating produced by steel only. This experiment would be useful to show the effectiveness of nanopaint-based heating for melting deposits from subsea steel pipelines.
- Wax deposits are heterogeneous in composition and melt non-uniformly. In our models, we considered homogeneous compounds. It would be useful to study the conduction of heat in a real wax deposit and its subsequent melting behavior.

Appendices

APPENDIX A: ADDITIONAL IMAGES

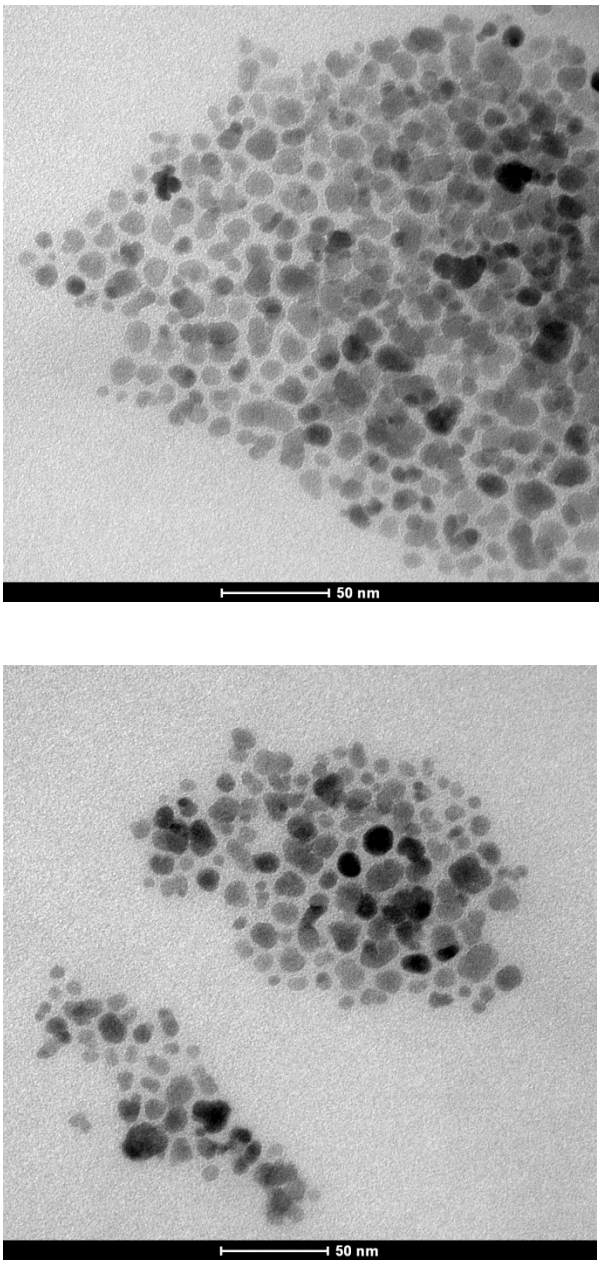

Figure A1: Additional Transmission Electron Microscope (TEM) images of iron oxide (Fe_3O_4) nanoparticles in EMG 1400 sample

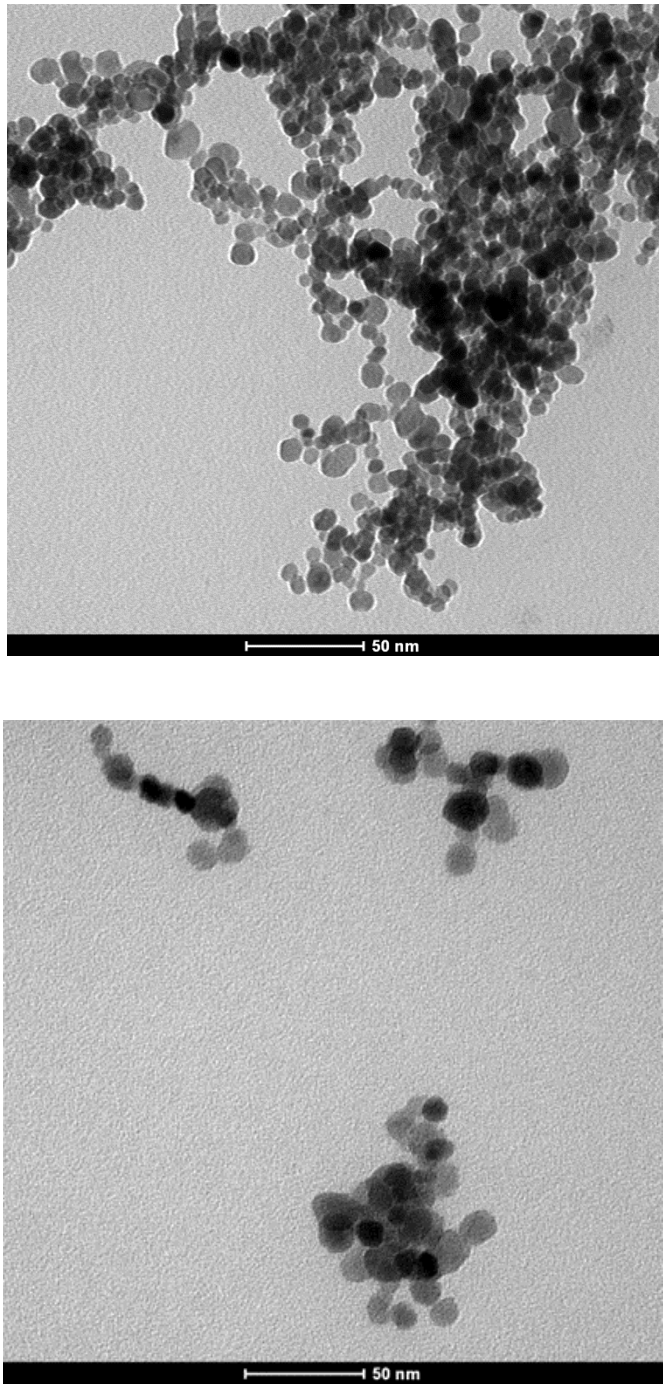

Figure A2: Additional Transmission Electron Microscope (TEM) images of iron oxide (Fe_3O_4) nanoparticles in EMG 605 sample

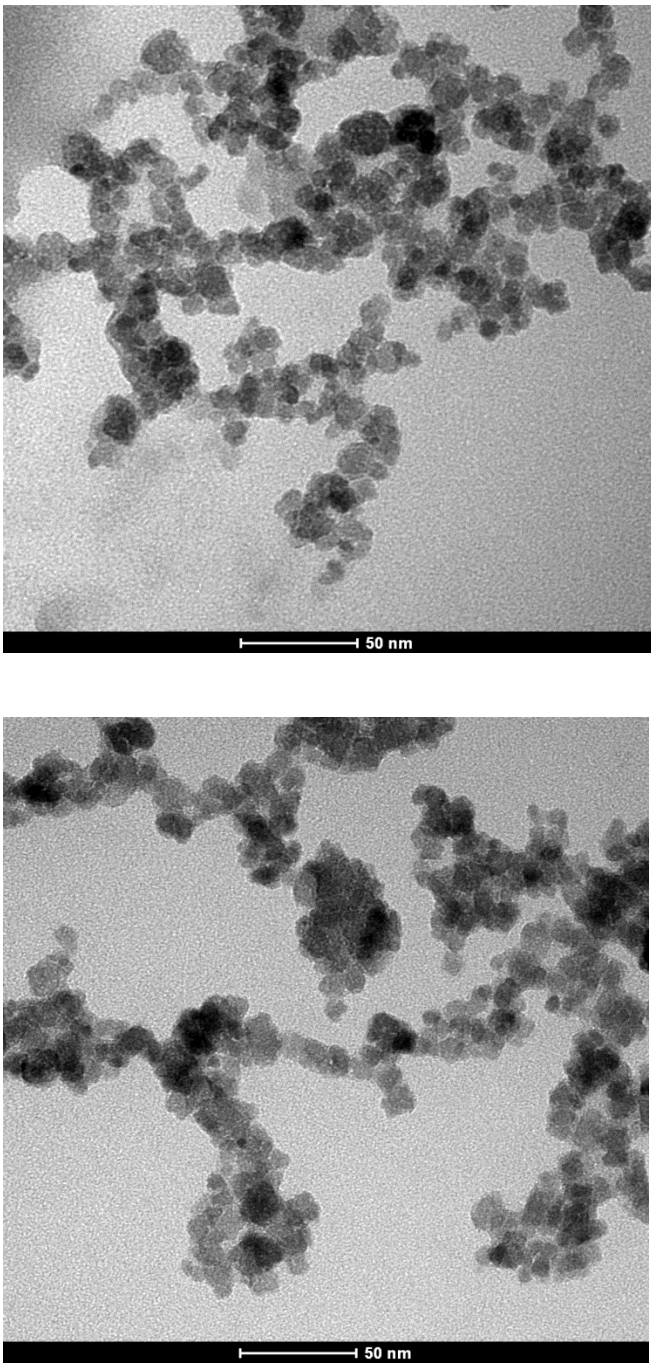

Figure A3: Additional Transmission Electron Microscope (TEM) images of iron oxide (Fe_3O_4) nanoparticles in PAA-8K sample

APPENDIX B: COMSOL MODELING GUIDE

An extensive modeling guide with access to examples and additional walkthroughs can be found on the COMSOL website (http://www.comsol.com). Included here is a basic step-by-step guide for setting up a model, and analyzing the output. This guide will demonstrate how the "Pipeline Wax Heating Model" from Chapter 5.2 was set up.

1) To set up a new model, first open a version of COMSOL; in this guide, COMSOL v4.3 will be used. First, the COMSOL model wizard will prompt you to 'Select a Space Dimension'. For this example, choose the '2D axisymmetric' space dimension.

2) Next, you will select the appropriate physics that describe your system. Select 'Heat transfer' module → Electromagnetic Heating → Induction Heating. This module simulates the effect of magnetic field on different materials; and models the heat generation by induction heating. The heat generation can be translated into temperature distribution inside a pipeline by placing probes and recording temperature, which will be discussed later.

3) Next, you will be prompted for the study type. In this case, we are interested in investigating the transient behavior of the system since the wax deposits on the nanopaint were heating with time. Hence, select 'Time Dependent' study and click 'Finish'. The COMSOL graphic user interface that appears upon finalizing the study type is shown in Figure B1.

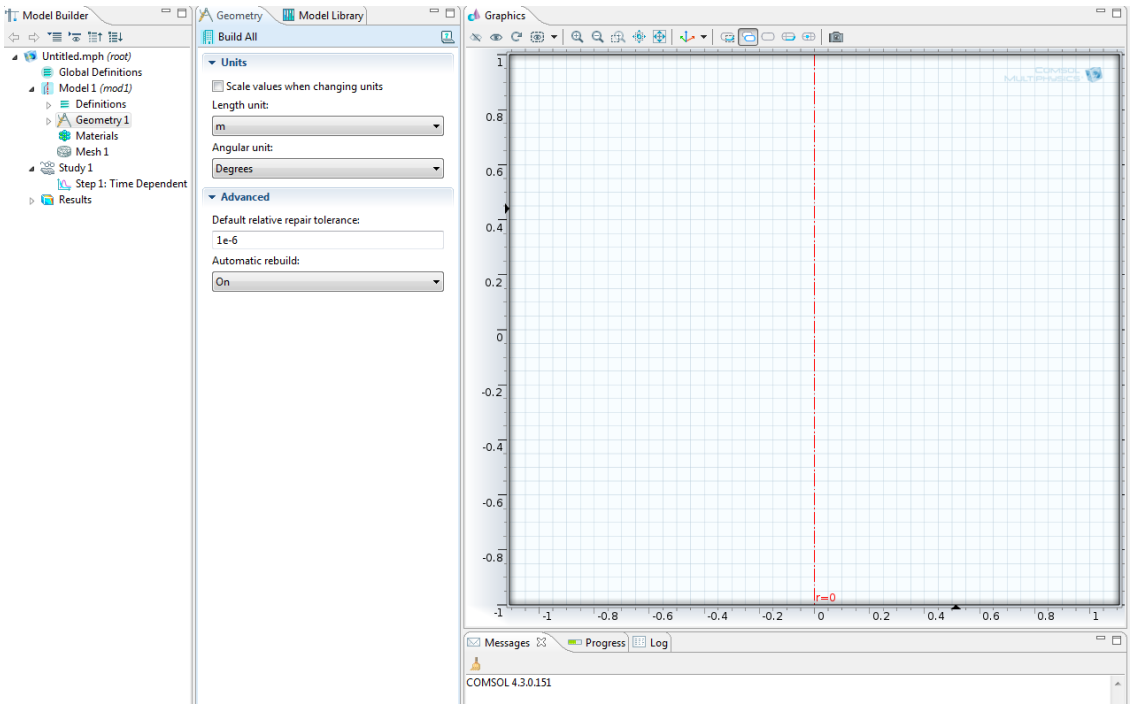

Figure B1: COMSOL graphic user interface from which models are built

4) Next, right click the 'Global Definitions' tab on the 'Model Builder' menu at the right side of the interface and click 'Parameters'. This will enable you to define the constants of the model. Constants can be entered as a function of other constants, and COMSOL will automatically compute the value. It is important to specify the units of the constants, and appropriately label what they signify in the 'Description' column. Variable names already used by COMSOL cannot be set as constant parameters without inducing an error in COMSOL; e.g., T cannot be used as a parameter in the heat transfer models because COMSOL already uses the variable for temperature. In the case of the wax heating model, we need to define constants for creating the coil, generating a magnetic field and generating heat in nanopaint as a function of magnetic field. First, we define the coil current (I_0), frequency of magnetic field (f), radius of the coil (r_{coil}), area of a single

coil (A_c) and number of turns in the multi-turn coil (N). Next, we define a heating constant based on SAR correlation (c). This is calculated by entering the values of all parameters in the equation (5), except magnetic field (H). The value of 'H' is calculated by the simulator based on coil current and is subsequently combined with 'c' to calculate heat generation, which will be shortly discussed. The initial system temperature is defined as T_0, and the sea water temperature is defined as T_i. The parameters list is shown in Figure B2.

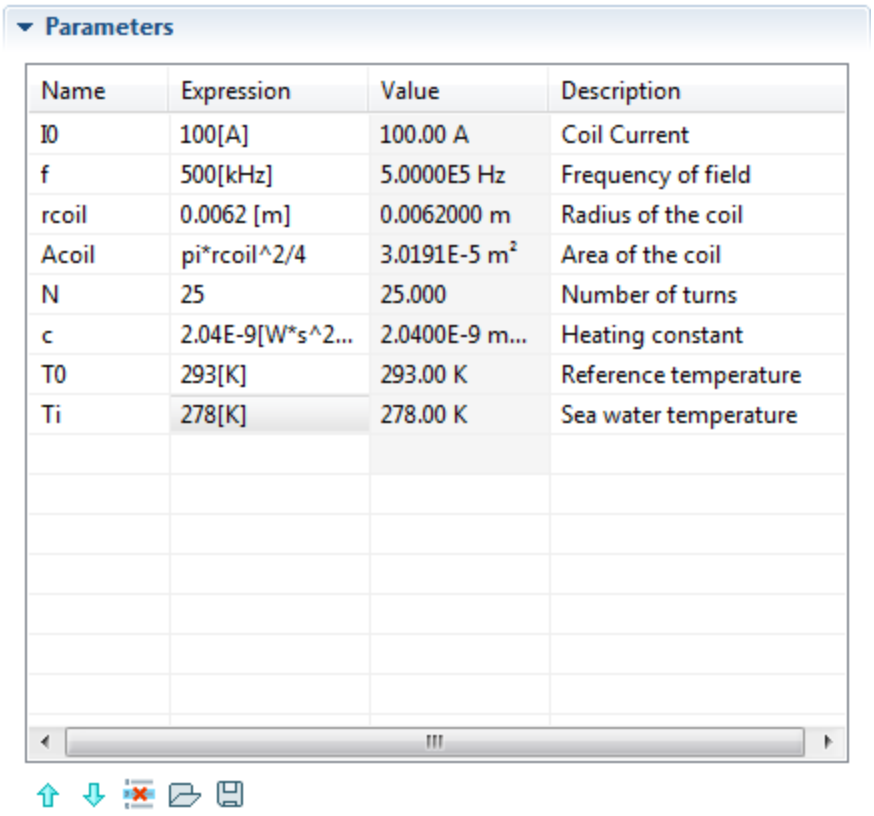

Figure B2: Example of parameters list used for pipeline wax heating model

5) Next, the model geometry is defined. In this case, a cylindrical pipe-in-pipe system coated with nanopaint, and containing a multi-turn coil is defined. Right click the

'Geometry' tab and add a rectangle to the model. The specification of the inner pipe, outer pipe, insulation, coil and wax are entered as per Table 9. It is important to understand that the 2D axisymmetric model simulates a cross-section of the pipe. Hence, the width of every rectangle is the radius of every section. Once, all values are entered, select 'Form a Union' and then 'Build All'. An interface similar to the one in Figure B3 will appear in the graphics window.

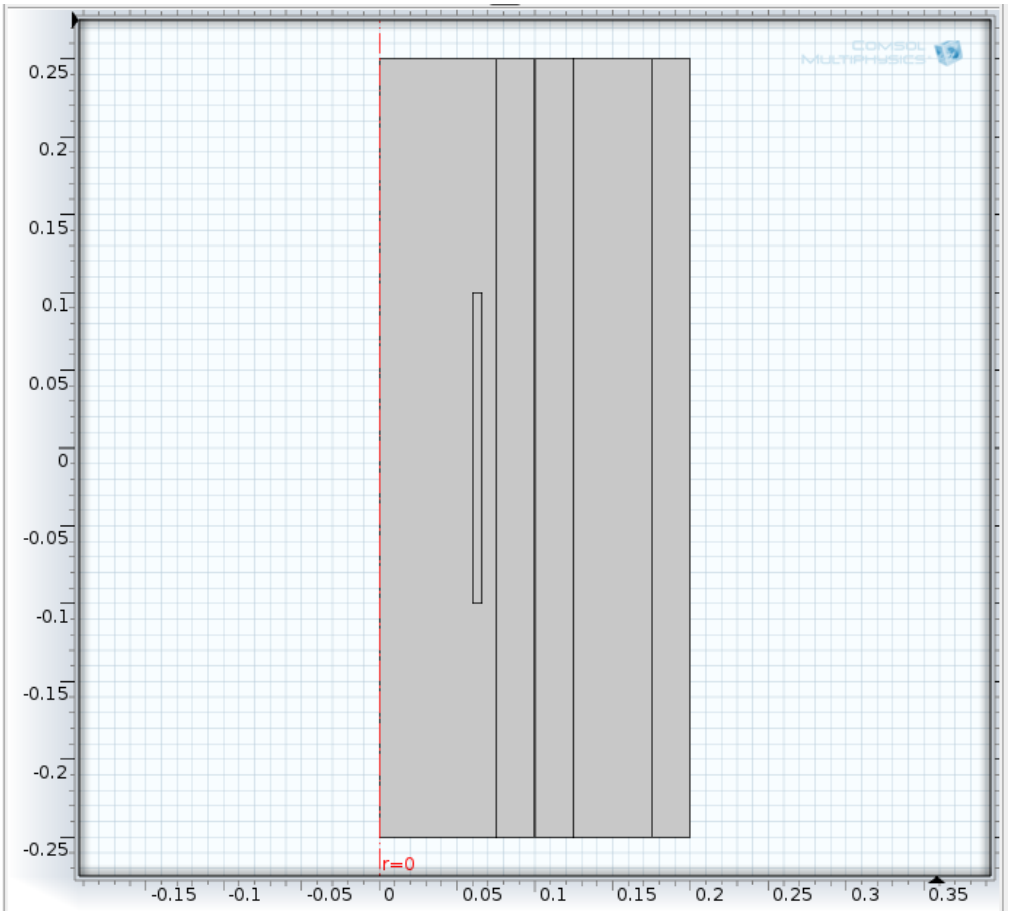

Figure B3: Interface shows geometry containing a multi-turn coil in a pipe-in-pipe system

6) Next, the variables and probes can be defined in the Model → 'Definitions' tab. Nanopaint heating is calculated by using the heating constant and the simulated magnetic field. Since the coil current is variable, so the magnetic field and heating varies. Hence, nanopaint heating is defined as a variable, Q on the nanopaint boundary (between inner pipeline and wax). Q is defined as per equation (33), for different nanoparticle loading. Next, we need to measure magnetic field and temperatures at various boundary. These can be measured using boundary probes. Right click on 'Definitions' → 'Probes' → 'Domain Point Probe'. Enter the 'x' and 'y' coordinates of the probe. In our case, we define several probes on the nanopaint surface (fixed 'x', variable 'y'), and one on the inner steel pipeline at y=0. Next, click on 'Point Probe Expression' and select the expression you want to measure. In our case, we select 'Induction Heating (Magnetic fields)' → 'Magnetic' → 'Magnetic field norm' (ih.normH). This measures the magnetic field on the nanopaint surface. We also define a temperature probe on the nanopaint surface.

7) After defining the appropriate geometries and probes, the materials that define those geometries must be input to the model. Right click the 'Materials' tab → 'Open the Material Browser'. Search to see if COMSOL has pre-defined a material to be used in the model. In our case, we used the 'AC/DC' and 'Liquids and Gases' tab to add appropriate materials – 'Copper' for the coil, and 'Steel AISI 430' for the inner and outer pipeline. Right click the desired material listing and add it to the model. In case the desired material was not found, the material can be manually added by right clicking Materials → Material. In this case, the material properties need to be entered.

(8) Next, the material is associated with its domain geometry. Left lick on the material, under 'Geometry Entity Selection' select the appropriate domain. The material

can be physically selected using the 'Graphics' view. When selected, the domain will now be defined by the selected material. An interface similar to Figure B4 will be seen.

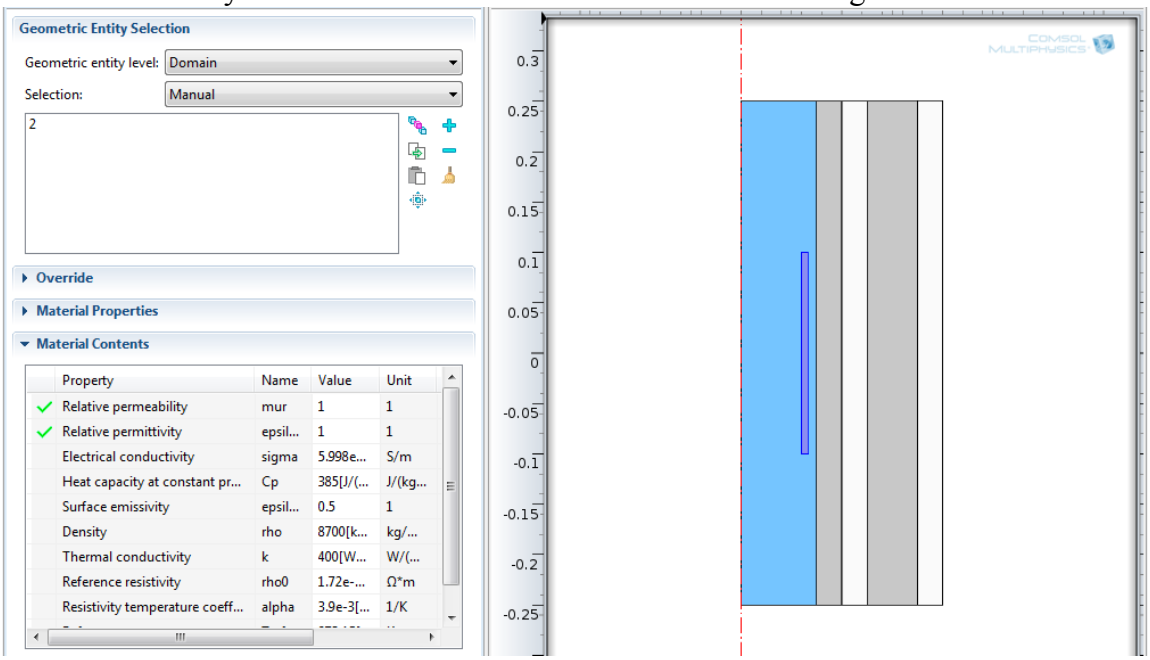

Figure B4: Material Selection in COMSOL used to define properties of a given material (highlighted in purple in the graphics window)

Next, the physics and boundary conditions will be defined. The model should already contain the physics for 'Induction Heating' and 'Initial Values' based on the initial model selection. Additionally, the induction heating condition is applied to every domain and multi-turn coil is defined. Click on Induction Heating, right click on 'Domains' → Induction Heating Model. Select a domain to apply the induction heating model. We need to define the induction heating model separately for each domain, to account for the interaction of magnetic field with a domain. Next, right click on 'Domains' → Magnetic Fields → Multi-Turn Coil Domains. Then select the domain to

apply this condition and enter values of current, conductivity, number of turns and so on. In our case, we ascertain them the symbol, whose value is defined in the global definitions section.

Next, we define the boundary conditions. By default, the condition of magnetic insulation and thermal insulation will be given. In addition, we add the condition of convective cooling on the outer pipeline by sea water circulation, and heating by Neel relaxation at the nanopaint boundary. Right click on 'Boundaries' →Heat Transfer in Solids → Convective Cooling. Select the boundary and enter the value of heat transfer coefficient (h) and external temperature (T_i). Next, right click on 'Boundaries' →Heat Transfer in Solids → Boundary Heat Source. Select the nanopaint boundary and enter 'Q' as the general heat source (as defined by the variable under 'Definitions' tab). This condition will calculate the heat generated at the nanopaint layer due to the magnetic field incident on it.

9) Now that the physics and boundary conditions have been defined, the model geometry is ready for meshing. The easiest way to mesh model geometry is to click the 'Mesh' tab from the model builder menu, select 'Physics-controlled' from the 'Sequence type' drop-down menu, select an element size and click 'Build All'. For our model, we used normal meshing, as shown in Figure B5. Physics-controlled meshing means that COMSOL will automatically insert small size mesh elements near important physics boundaries to improve calculation accuracy. The mesh size can be adjusted based on the model results, and re-meshing can be implemented if refined results are desired. Meshing can be performed on a custom basis by meshing specified geometries or domains separately using a different mesh type.

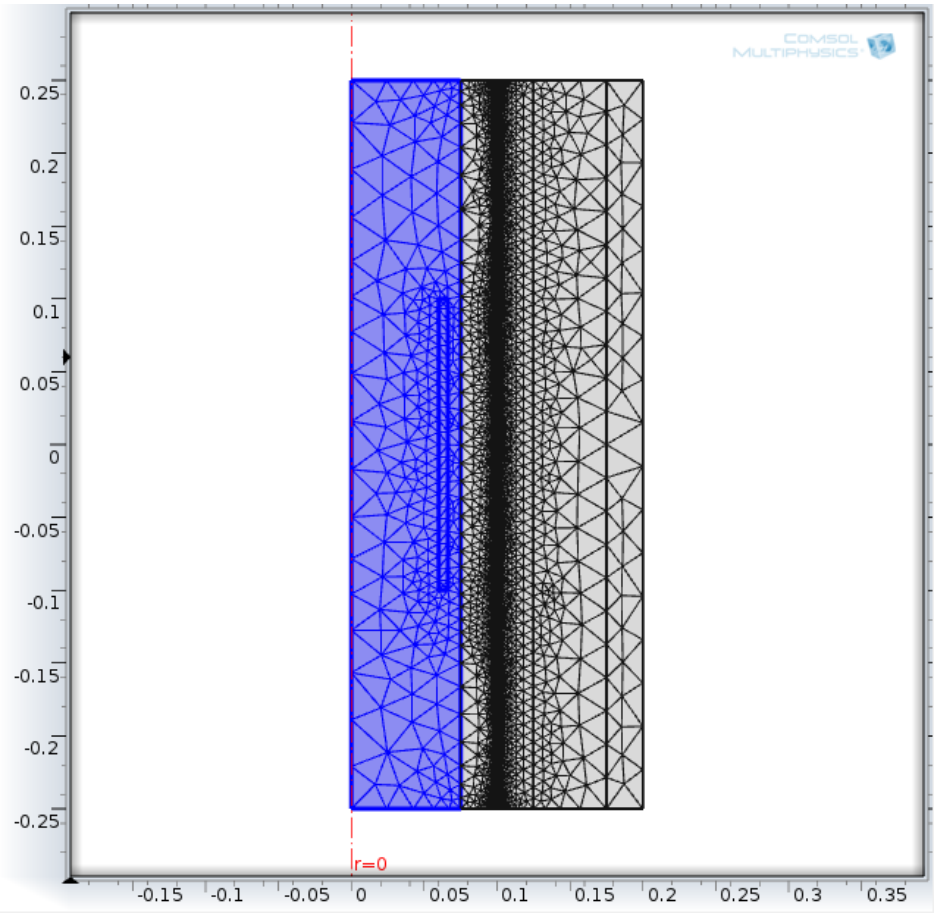

Figure B5: Completed, physics-controlled, triangular meshing of nanopaint-coated pipe-in-pipe system containing multi-turn coil

10) Now, the model is ready to be simulated. Click on the 'Study 1' tab → 'Step 1: Frequency-Transient'. Here, you can select the time of the study (in seconds) and the time interval for the computation, of the form - initial value, time interval, final time. To run the simulation, select 'Compute'. If a parametric sweep of a parameter is desired, this is that tab where that sweep is defined. Running a parametric sweep enables COMSOL to run multiple simulations without the user re-executing the simulation for each parameter.

11) Finally, the results can be analyzed using different types of plots. Be default, the values of the probes (defined under Definitions), will be displayed for the various times of the study under the 'Result' window, as shown in Figure B6. To further analyze the result, this table can be exported. Further, 2D and 3D plots of magnetic field were generated. Right click on the 'Results' tab from the Model Builder menu and add a 2D Plot Group to the results. Next, right click 2D plot group →Surface Plot. Select the desired expression, which in our case is magnetic field norm (ih.normH). Before plotting, it is important to select the desired time of computation from the drop-down menu. When you click on 'Plot', a figure similar to Figure B7 will be seen. Next, add a 3D plot group to the results. Right click 3D plot group → Streamline. Under expression, select 'Magnetic field (r, phi and z components)'. When it is plotted, a figure similar to Figure B8 will be displayed.

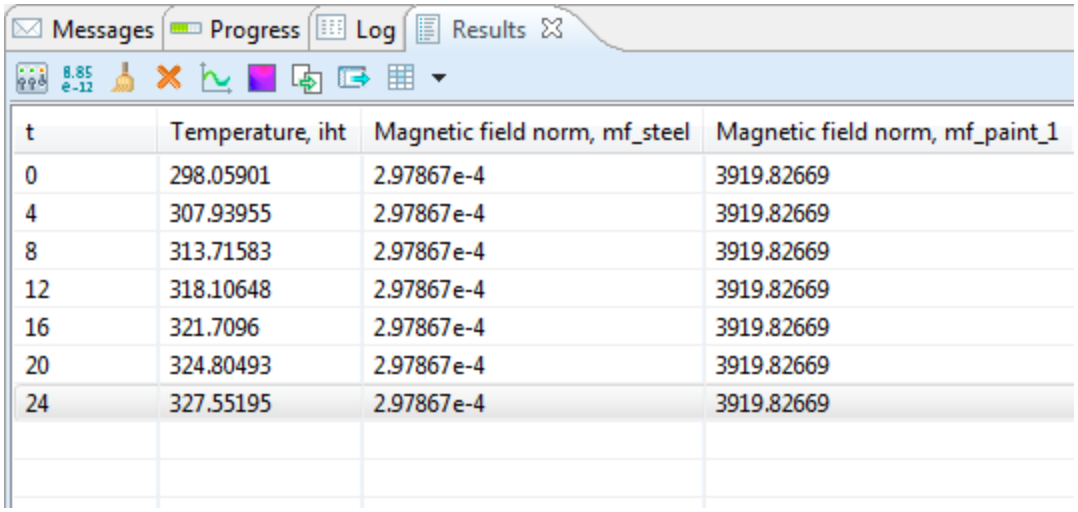

t	Temperature, iht	Magnetic field norm, mf_steel	Magnetic field norm, mf_paint_1
0	298.05901	2.97867e-4	3919.82669
4	307.93955	2.97867e-4	3919.82669
8	313.71583	2.97867e-4	3919.82669
12	318.10648	2.97867e-4	3919.82669
16	321.7096	2.97867e-4	3919.82669
20	324.80493	2.97867e-4	3919.82669
24	327.55195	2.97867e-4	3919.82669

Figure B6: Results show various probe measurements for temperature and magnetic field at different time intervals

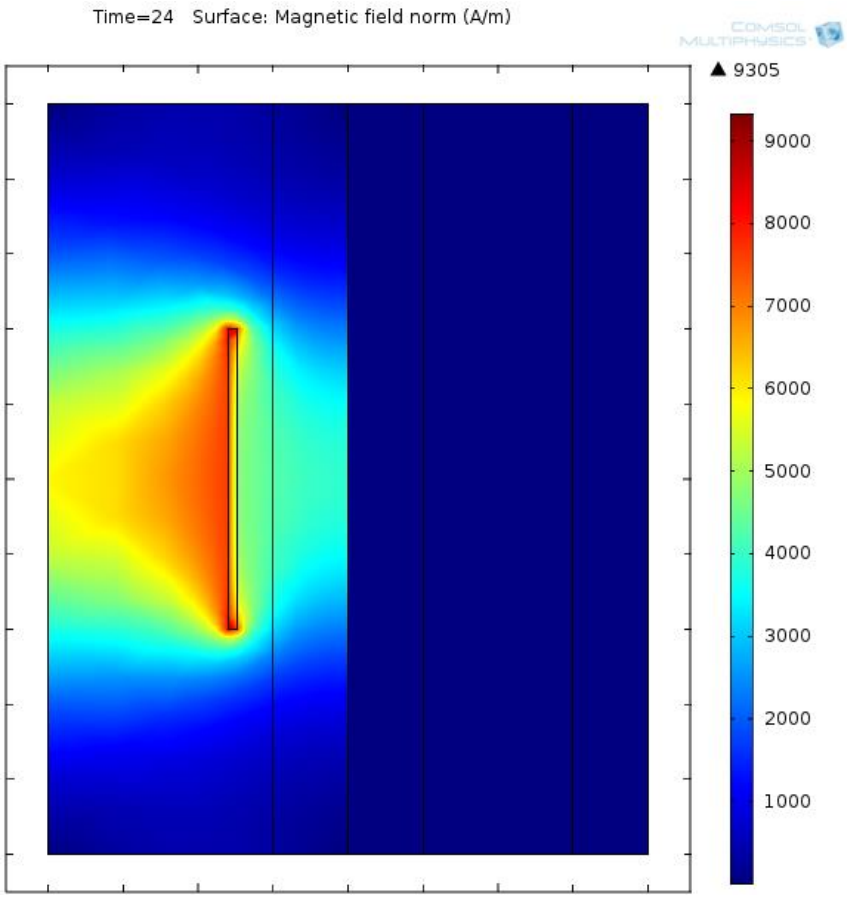

Figure B7: Example 2D surface plot of magnetic field

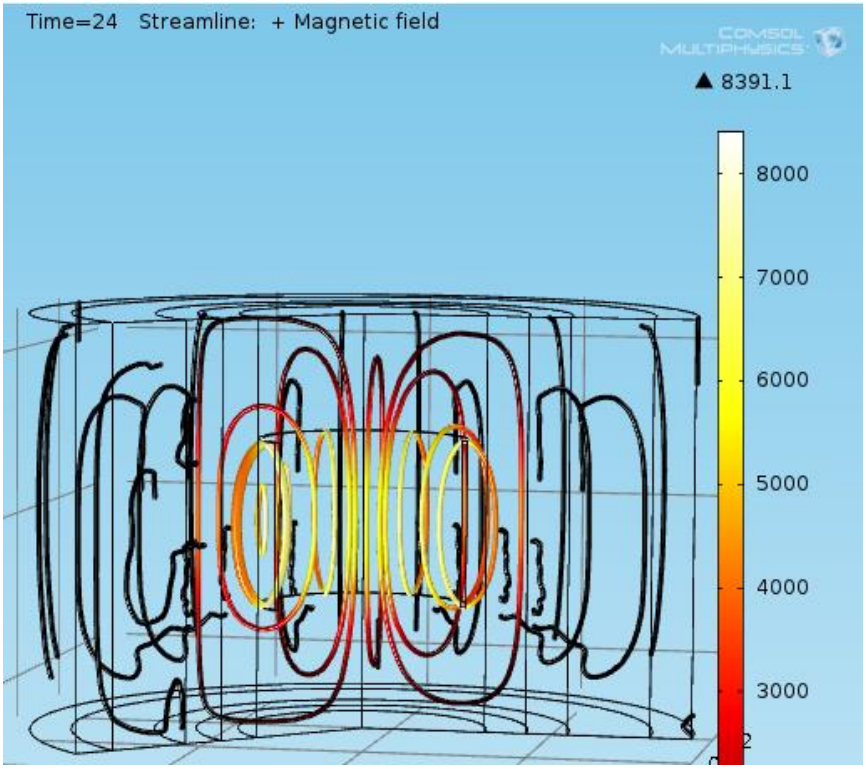

Figure B8: Example 3D streamline plot of magnetic field

To export data or plot, click on Export under the Model Builder window. Select the desired plot or table, layout and image options and click on Export.

APPENDIX C: DERIVATION OF MAGNETIC FIELD FORMULA

Magnetic Field Component of a 3-Turn Coil

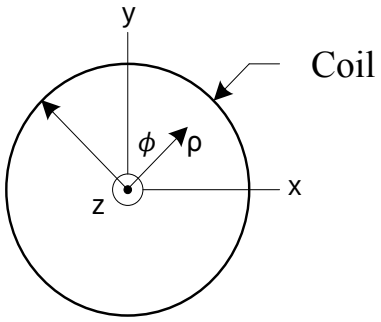

Figure C1: Coordinate system of a circular coil

The magnetic field formula for a 3-turn coil is derived from Biot-Savart Law, given by

$$\int \overrightarrow{dH} = \frac{I}{4\pi}\int \frac{\overrightarrow{dl}\times\overrightarrow{a_R}R}{R^3}. \tag{36}$$

where $\overrightarrow{dl} = ad\varphi\overrightarrow{a_\varphi}$ and $R = \sqrt{a^2 + z^2}$

where $\overrightarrow{dH}$ is the vector component of the magnetic field (A/m), $\overrightarrow{a_R}$ is a unit vector, and a is the radius of the coil (m). Here, the law is applied over a single-turn and the definition is extended to several turns over a small length of coil.

$$\overrightarrow{dl} \times \overrightarrow{a_R} = dl\,\overrightarrow{a_\varphi} \times \overrightarrow{a_R} \tag{37}$$

$$\overrightarrow{dl} \times \overrightarrow{a_R} = dl\,\overrightarrow{a_\varphi} \times \frac{z(-\overrightarrow{a_\rho}) + a\overrightarrow{a_z}}{\sqrt{a^2 + z^2}}$$

Taking the cross product, gives

$$\overrightarrow{dl} \times \overrightarrow{a_R} = \frac{a^2\overrightarrow{a_z}\,\overrightarrow{a_\varphi}d\varphi}{R}. \tag{38}$$

Integrating $d\varphi$ over a circular loop of 2π gives,

$$\int \overrightarrow{dH} = \frac{I}{4\pi}\int_0^{2\pi} \frac{a^2 \overrightarrow{a_z}\,\overrightarrow{a_\varphi} d\varphi}{R^3}$$

The z-component of the magnetic field of a single turn of a circular coil is given by,

$$H_z = \frac{Ia^2}{2(a^2+z^2)^{3/2}}. \tag{39}$$

For multiple turns of the circular coil, the H_z for each coil turn is computed separately for its position (z) relative to the observer point and the results added. Simplification of the above formula for our 3-turn coil specification gives,

$$H_c = 23.6 \times I \tag{40}$$

where H_c is the total magnetic field at the center of the 3-turn coil in A/m and I is the current flowing through the coil in A.

Magnetic Field Component (H_z) of a 5-Turn Ribbon Coil

The derivation of 3-turn coil is extended to calculate the field of a 5-turn ribbon coil. The ribbon coil has a different geometry and needs to be accounted for in the derivation. Figure C2 shows a cross sectional view of the ribbon coil and indicates the observer point at z where the vertical component of the magnetic field, H_z, is computed. The coordinate, z, may have any value $-\infty < z < +\infty$, The coil carries a total current of I Amperes distributed uniformly along the vertical extent of the ribbon conductor of radius a that extends vertically from $z = -\frac{h}{2}$ to $z = +\frac{h}{2}$.

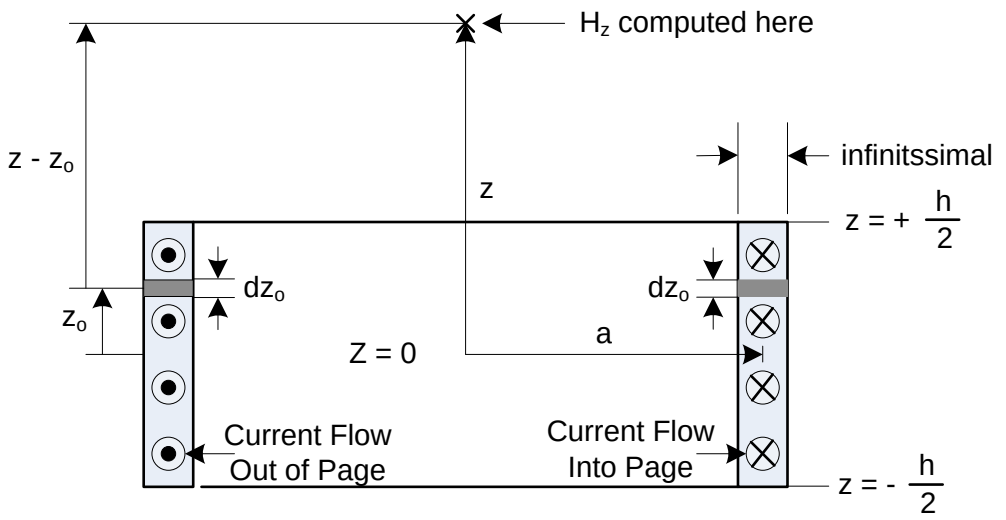

Figure C2: Cross-sectional view of the ribbon coil

The field component, H_z, is computed by modifying the formula derived from a circular coil of small round wire, equation (39).

$$H_z = \frac{Ia^2}{2(a^2 + z^2)^{3/2}}$$

The modifications include: (1) replacing I by $\frac{I}{h}$ which distributes the current uniformly along the vertical extent of the ribbon, and replacing z by $z - z_o$. The result is then integrated with respect to z_o from $z_o = -\frac{h}{2}$ to $z_0 = +\frac{h}{2}$. This integral is expressed as

$$H_z = \frac{Ia^2}{2h} \int_{-h/2}^{h/2} \frac{dz_0}{[a^2 + (z - z_o)^2]^{3/2}}. \tag{41}$$

An integral table gives the following

$$\int \frac{dx}{r^3} = \frac{x}{a^2 r}$$

for

$$r = (x^2 + a^2)^{1/2}$$

If we let $z - z_o = x$ which gives $dz_o = -dx$ we evaluate the H_z integral as,

$$H_z = \frac{I}{2h}\left[\frac{z+\frac{h}{2}}{\sqrt{a^2+\left(z+\frac{h}{2}\right)^2}} - \frac{z-\frac{h}{2}}{\sqrt{a^2+\left(z-\frac{h}{2}\right)^2}}\right]. \tag{42}$$

For multiple turns of the ribbon coil the H_z for each coil turn is computed separately for its position relative to the observer point and the results added. Simplification of the above formula for our 5-turn ribbon coil specification gives,

$$H_r = 20.55 \times I \tag{43}$$

where H_r is the total magnetic field at the center of the 5-turn ribbon coil in A/m and I is the current flowing through the coil in A.

Glossary

μ	=	Magnetic permeability, m kg s^{-2} A^{-2}
N	=	Number of coil turns
I	=	Current, A
L	=	Length, m
a	=	Radius of the coil, m
z	=	Height of the coil or distance from origin, m
μ_0	=	magnetic permeability of free space, H m^{-1}
H	=	Magnetic field strength (amplitude), A m^{-1}
M	=	Magnetization, A m^{-1}
M_s	=	Saturation magnetization, A m^{-1}
B	=	Induced magnetic field, T
K_v	=	NP volume anisotropy, kJ m^{-3}
V	=	NP volume, m^3
K_s	=	NP surface anisotropy, kJ m^2
τ_N	=	Neel relaxation time constant, s
τ_0	=	Characteristic time constant, s
K_b	=	Boltzmann's constant, m^2 kg s^{-2} K^{-1}
T	=	Temperature, K
τ_m	=	Characteristic magnetization time, s
τ_B	=	Brown relaxation time, s
τ	=	Effective relaxation time constant, s
D_p	=	Mean nanoparticle diameter, nm
χ	=	Magnetic susceptibility
f	=	frequency, Hz
q	=	Heat flux, W m^{-2}
D_p	=	NP diameter, nm
W_p	=	Weight fraction of magnetite nanoparticle in dried nanopaint
SAR	=	Specific absorption rate of fluid, W g^{-1}
ρ	=	density, kg m^{-3}
k_i	=	Thermal conductivity of material 'i', W m^{-1} K^{-1}
$C_{p,\ Paint}$	=	Specific heat capacity of nanopaint, J g^{-1} K^{-1}
C_{DP}	=	Specific heat capacity of additive-added paint, J g^{-1} K^{-1}
Q	=	Nanopaint heat source, W m^{-2}

h	=	Convective heat transfer coefficient of sea water, W m^{-2} K^{-1}
E	=	Electric field, V m^{-1}
ω	=	Angular frequency, Hz
ε	=	Electric permittivity
σ	=	Electric conductivity, S m^{-1}
l_{NP}	=	Nanoparticle loading, g/m^2
P	=	Power consumed per km of pipeline, Wh/km
R	=	Resistance of the copper coil, Ω
L	=	Length of the pipeline section, m
$P_{battery}$	=	Power supplied by a battery, Wh
M	=	Amount of energy stored in a battery, mAh
N_c	=	Number of cells in the battery
V_s	=	Voltage of a standard cell, V

References

Bakoglidis, K. D., Simeonidis, K., Sakellari, D., Stefanou, G., & Angelakeris, M., 2012. Size-dependent mechanisms in AC magnetic hyperthermia response of iron-oxide nanoparticles. IEEE Transactions on Magnetics, 48(4), 1320–1323.

Balanis, C.A., 1989. Advanced Engineering Electromagnetics. In John Wiley & Sons.

Benz, M., 2012. Superparamagnetism : Theory and Applications., 1–27.

Boddie, A.W., W. Frazer, J. & Yamanashi, W.S., 1987. RF electromagnetic field generation apparatus for regionally-focused hyperthermia.

Bologna, M., 2001. Generator of Electromagnetic Waves for Medical Use.

Chatterjee, J., Haik, Y. & Chen, C.-J., 2003. Size dependent magnetic properties of iron oxide nanoparticles. *Journal of Magnetism and Magnetic Materials*, 257(1), 113–118.

Coffey, W. & Kalmykov, Y., 2012. Thermal Fluctuations of Magnetic Nanoparticles : *Journal of Applied Physics*, 121301(112), 1–99.

Davidson, A., Huh, C. & Bryant, S.L., 2012. Focused Magnetic Heating Utilizing Superparamagnetic Nanoparticles for Improved Oil Production Applications. *SPE International Oilfield Nanotechnology Conference*, SPE 157046, 1–16.

Denniel, S., Perrin, J., Felix-henry, G. F. A., & France, F., 2004. Review of Flow Assurance Solutions for Deepwater Fields. Offshore Technology Conference, OTC 16686.

Glöckl, G., Hergt, R., Zeisberger, M., Dutz, S., Nagel, S., and Weitschies, W., 2006. The Effect of Field Parameters, Nanoparticle Properties and Immobilization on the Specific Heating Power in Magnetic Particle Hyperthermia. Journal of Physics: Condensed Matter 18 (38): S2935–49.

Gonzales-Weimuller, M., Zeisberger, M. & Krishnan, K.M., 2009. Size-dependent heating rates of iron oxide nanoparticles for magnetic fluid hyperthermia. *Journal of Magnetism and Magnetic Materials*, 321(13), 1947–1950.

Goya, G. F., T. S. Berquó, Fonseca, F. C., and Morales, M. P., 2003. Static and Dynamic Magnetic Properties of Spherical Magnetite Nanoparticles. Journal of Applied Physics 94(5): 3520–3528

Harrington, J.A., Matsuura, Y. & Optic, F., 1995. Review of hollow waveguide technology. *SPIE*, 2396(1), 4–14.

Hergt, R., Hiergeist, R., Zeisberger, M., Glöckl, G., Weitschies, W., Ramirez, L. P., Hilger, I., Kaiser, W. A., 2004. Enhancement of AC-losses of magnetic nanoparticles for heating applications. Journal of Magnetism and Magnetic Materials, 280(2-3), 358–368.

Hergt, R., Andrae, W., D'Ambly, Carl G., Hilger, I., Kaiser, W.A., Richter, U., and Schmidt, H.G., 1998. Physical Limits of Hyperthermia Using Magnetite Fine Particles. IEEE Transactions on Magnetics 34 (5-2): 3745–54.

Hergt, R., Dutz, S. & Röder, M., 2008. Effects of size distribution on hysteresis losses of magnetic nanoparticles for hyperthermia. *Journal of physics. Condensed matter : An Institute of Physics journal*, 20 (2008) 385214, 1-12.

Holloway, C.L., Hill, D.A., Dalke, R.A., and Hufford, George A., 2000. Radio wave propagation characteristics in lossy circular waveguides such as tunnels, mine shafts, and boreholes. *IEEE Transactions on Antennas and Propagation*, 48(9), 1354–1366.

Hsu, M.H. & Su, Y.C., 2008. Iron-oxide embedded solid lipid nanoparticles for magnetically controlled heating and drug delivery. *Biomedical Microdevices*, 10(6), 785-793.

Huang, Q., Li, S., Wang, W., and Wang, C., 2014. "Experimental Investigation of Wax Deposition at Different Locations Through a Detachable Flow Loop Apparatus. Proceedings of the 10th International Pipeline Conference. IPC2014-33007: 1–7.

Jordan, A., Scholz, R., Wust, P., Fähling, H., and Felix, R., 1999. Magnetic Fluid Hyperthermia (MFH): Cancer Treatment with AC Magnetic Field Induced Excitation of Biocompatible Superparamagnetic Nanoparticles. Journal of Magnetism and Magnetic Materials 201 (1-3): 413–419.

Kita, E., Yanagihara, H., Hashimoto, S., Yamada, K., Oda, T., Kishimoto, M., and Tasaki, A., 2008. Hysteresis power-loss heating of ferromagnetic nanoparticles designed for magnetic thermoablation. IEEE Transactions on Magnetics, 44(11-2), 4452–4455.

Kneller, E.F. & Luborsky, F.E., 1963. Particle size dependence of coercivity and remanence of single-domain particles. *Journal of Applied Physics*, 34(3), 656–658.

Kok, M.V. & Saracoglu, R.O., 2000. Mathematical Modelling of Wax Deposition in Crude Oil Pipelines. *Petroleum Science and Technology*, 18(9-10), 1121–1145.

Kötitz, R., Weitschies, W., Trahms, L., & Semmler, W., 1999. Investigation of Brownian and Neel relaxation in magnetic fluids. Journal of Magnetism and Magnetic Materials, 201(3), 102–104.

Lévy, M., Wilhelm, C., Siaugue, J.-M., Horner, O., Bacri, J.-C., & Gazeau, F., 2008. Magnetically induced hyperthermia: Size-dependent heating power of γ-Fe_2O_3 nanoparticles. Journal of Physics. Condensed Matter : An Institute of Physics Journal, 20(2008) 204133, 1-5.

Minami, K., Kurban, A. P. A., Khalil, C. N., & Kuchpil, C., 1999. Ensuring Flow and Production in Deepwater Environments. Offshore Technology Conference, OTC 11035, 1–9.

Ondeck, C. L., Habib, A. H., Ohodnicki, P., Miller, K., Sawyer, C. A., Chaudhary, P., and McHenry, M. E., 2009. Theory of magnetic fluid heating with an alternating magnetic field with temperature dependent materials properties for self-regulated heating. Journal of Applied Physics, 105(7).

Pankhurst, Q. A., Connolly, J., Jones, S. K., & Dobson, J., 2003. Applications of magnetic nanoparticles in biomedicine. Journal of Physics D: Applied Physics, 167(13), R167–R181.

Reutov, Y.Y. & Loskutov, V.E., 2007. Penetration of the magnetic field of a marker placed inside a gas pipeline through a steel tube wall. *Russian Journal of Nondestructive Testing*, 43(11), 718–723.

Rosensweig, R.E., 2002. Heating magnetic fluid with alternating magnetic field. *Journal of Magnetism and Magnetic Materials*, 252 (2002), 370–374.

Rovers, S. A., Poel, L. A. M. Van Der, Dietz, C. H. J. T., Noijen, J. J., Hoogenboom, R., Kemmere, M. F., Kopinga, K., and Keurentjes, J. T. F., 2009. Characterization and Magnetic Heating of Commercial Superparamagnetic Iron Oxide Nanoparticles. Journal of Physical Chemistry C (113), 14638–14643.

Surducan, V., Surducan, E., Ciupa, R., & Neamtu, C., 2012. Microwave generator for scientific and medical applications. AIP Conference Proceedings, 1425, 89 (2012).

Thanh, N.T., 2012. *Magnetic Nanoparticles: From Fabrication to Clinical Applications*, CRC Press.

Turner, P. F., Hagmann, M., Youd, T. L., & Elsworth, J. L., 2010. Transparent electromagnetic applicator and hyperthermia treatment method. U.S. Patent 11/367,076.

Varon, L., Orlande, H. & Vianna, F., 2012. Estimation of the Convective Heat Transfer Coefficient in Piplines With the Markov Chain Monte Carlo Method. *Proceedings of the 10th World Congress on Computational Mechanics*.

Wang, X. W. X., Tang, J. T. J., & Shi, L. S. L., 2010. Induction Heating of Magnetic Fluids for Hyperthermia Treatment. IEEE Transactions on Magnetics, 46(4), 1043–1051.